Morphological Evolution of Rock-Slopes and Assessing the Rockfall Activity Index (RAI) Methodology

Shane Joseph Markus

A thesis

submitted in partial fulfillment of the

requirements for the degree of

Master of Science in Civil Engineering

University of Washington

2018

Committee:

Joseph Wartman

Brett Mauer

Program Authorized to Offer Degree:

Civil & Environmental Engineering

University of Washington

Abstract

Morphological Evolution of Rock-Slopes and Assessing the Rockfall Activity Index (RAI) Methodology

Shane Joseph Markus

Chair of the Supervisory Committee:
Joseph Wartman
Department of Civil & Environmental Engineering

Rockfall poses a significant monetary and life-safety hazard to transportation corridors in mountainous regions. In well-indurated, relatively continuous rock, the orientation and spacing of discontinuities can be quantified to investigate the interaction between distinct rock blocks, and subsequently perform stability analyses. However, in lower-quality, highly discontinuous rock, joint patterns are often too complex to perform traditional stability analyses. Rockfall hazard rating and rock mass classification methodologies have been adopted to provide relative rockfall hazard assessments of slopes in highly jointed rock, but these methods are subjective and have poor spatial resolution.

The Rockfall Activity Index (RAI) developed by Dunham *et al.* (2017) uses high-resolution terrestrial laser scanning-derived point cloud models of rock-slope morphology to provide a higher-resolution, quantifiable alternative to traditional hazard rating systems.

Using outputs of rockfall detection algorithms at four study sites in Alaska, the efficacy of the RAI system is investigated, and modification to the RAI methodology is proposed to better represent rock-slope mass-wasting processes. Additionally, rockfall detection data is used to understand recession rates and morphological evolution of these rock-slopes.

Table of Contents

1. Introduction

Rock-slope instability poses a significant hazard to infrastructure and communities in mountainous terrain. Transportation corridors (such as highways and railroads) are particularly vulnerable to life-safety or monetary hazards (Turner and Jayaprakash, 2012) due to rockfall events, because of their linear nature and, therefore, lengthy exposure to potentially unstable rock-slopes. In these corridors, rock blocks can fall from natural or man-made slopes into roadways or railways, potentially colliding with vehicles, trains, and pedestrians, causing human losses, damage to infrastructure, and delays for clean-up.

In high-quality rock-masses (i.e., well-indurated rocks having relatively few, widely spaced discontinuities), stability depends on specific block and discontinuity geometries. Rock-masses such as these are typically analyzed using 2- or 3-dimensional limit-equilibrium or discrete element models. Lower quality rock-masses are typically associated with weak rock or highly jointed rock materials (Hoek, 2006). These rock-masses are complex and are often assessed using rock mass classification systems such as the Rockfall Hazard Rating System (RHRS), which rely on visual inspection and basic rock-mass data to analyze susceptibility to rockfall (Dunham *et al.*, 2017). In addition to these analyses, these systems are also used for preliminary design and budgeting for higher-quality rock-slopes (Bieniawski, 1997). These systems are generally coarse in spatial resolution, subjective in nature, and sometimes expose workers to the hazards associated with rock-slopes (Hoek, 2006).

Advancements in Light Detection and Ranging (LiDAR) technology have allowed for the development of high-resolution models of the structure of rock-slopes in recent years. Prior to this paper, researchers at the University of Washington have developed a methodology, known as the Rockfall Activity Index (RAI) System, to use these high-resolution models of low-quality rock-slopes to develop hazard maps of the slopes (Dunham *et al.*, 2017). This system attempts to improve the spatial

resolution, enhance the safety, and create a more objective measurement of rock-slope quality than previous systems have accomplished. This methodology is discussed in detail later in this thesis.

The development of LiDAR has also allowed for high-resolution detection of rock-slope failures, through the comparison of two scans of the same site collected at different time intervals. This thesis uses data from the change detection of four distinct test sites in south-central Alaska to inform on the efficacy of the RAI system and suggests modifications to improve the system. This thesis also intends to investigate other characteristics of mass-wasting processes that can be derived from the change detection data.

1.1 Study Sites

Two regions in southcentral Alaska were selected by the Alaska Department of Transportation & Public Facilities for the RAI project work. The rock-slopes in these regions were selected due to their history of causing damage to the roadways and threatening life safety, and because of their accessibility to mobile (i.e., vehicle-based) LiDAR and Terrestrial Laser Scanning (TLS) equipment. The two study regions are shown in Figure 1**.** Location of study regions (Google Maps) The first, known as Long Lake, is located approximately 70 miles northeast of Anchorage along the Glenn Highway (AK-1) from milepost 71 to 89, in the Matanuska Valley. The second, known as Glitter Gulch, is located along the George Parks Highway (AK-3) from milepost 239 to 241, in the Nenana River Valley, near Healy in the Alaska Range.

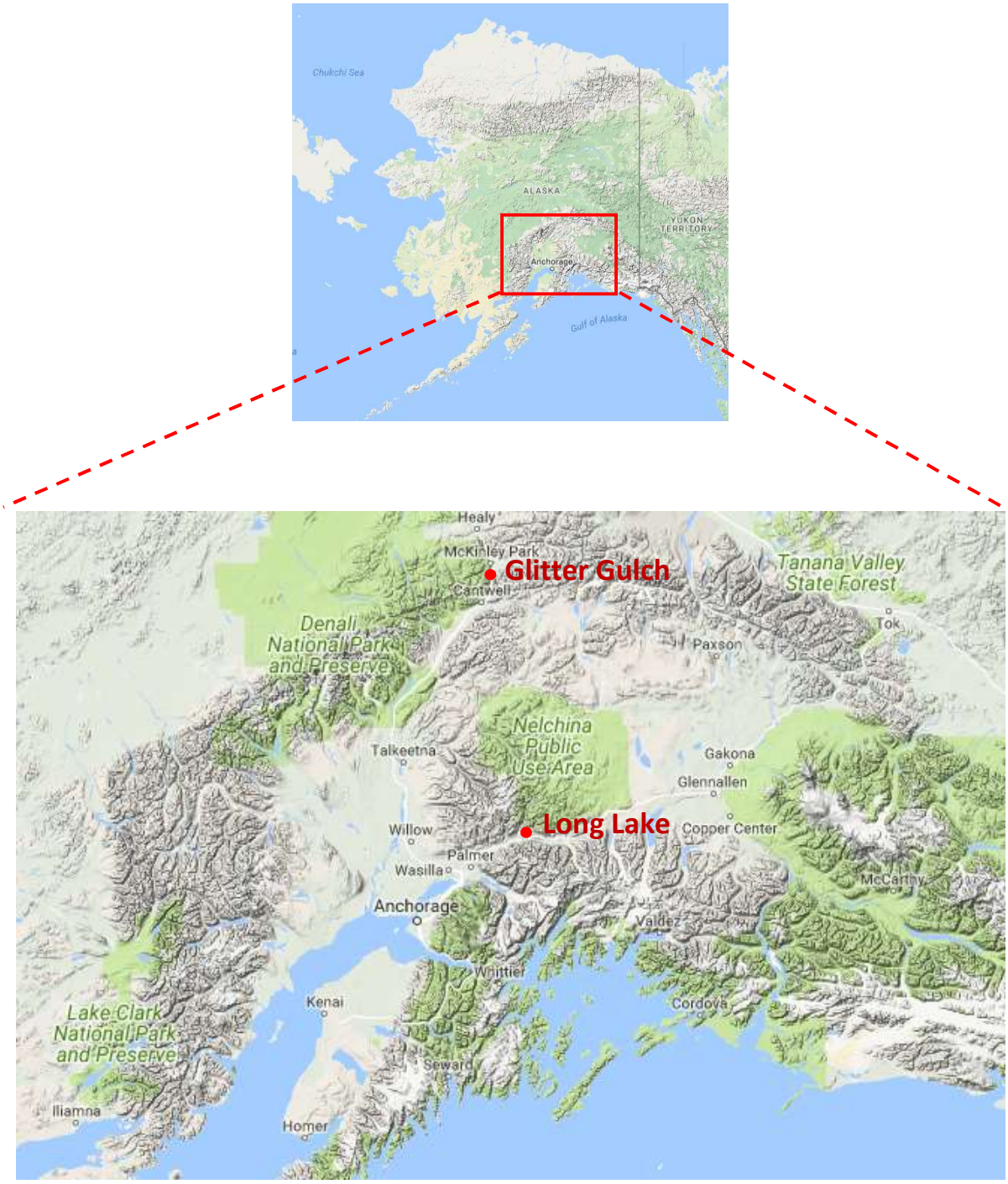

Figure 1. Location of study regions (Google Maps)

Four distinct study sites in the Long Lake region were specifically chosen for this paper. These four sites were selected because of their variety in slope morphology, variability in sizes, and variability in locations along the Glenn Highway. The four sites are referred to as Long Lake milepost 71 (i.e., *"LL71"*), Long Lake milepost 85.5 (i.e., *"LL85.5"*), Long Lake milepost 86.9 (i.e., *"LL86.9"*) and Long Lake milepost 87 (i.e., *"LL87"*). The locations of the four sites are shown below, in Figure 2**.** Table 1 provides dimensions of the sites as well. Images of the four study sites are provided in Figures 3 through 6.

Figure 2. Vicinity map of the Long Lake study region, with the four Study Sites for this paper highlighted (Google Maps)

	Height (m)	Width (m)	Area (m^2)	Average Angle
Long Lake 71	53.9	285	16837.8	66°
Long Lake 85.5	10.8	60.5	678.5	56°
Long Lake 86.9	18.5	84.5	2203.0	50°
Long Lake 87	13.2	103.4	1569.8	58°

Table 1. Dimensions of the four study sites

Figure 3. Image of LL71

Figure 4. Image of LL85.5

Figure 5. Image of LL86.9 (Google Earth)

Figure 6. Image of LL87

1.2 Regional Geologic Setting

Southern Alaska is a tectonically active setting. Movement between the Pacific Plate, the Yakutat Plate, the North American Plate, and the Bering Plate create a compressional environment in this region. Some of the largest earthquakes, most prevalent volcanism, and most dramatic mountain ranges can be found here because of this tectonic activity. This environment has also worked to accrete materials onto the south shore of Alaska. These materials often have regionally similar geologic histories and are commonly known as terranes. These individual terranes were derived from ancient ocean basins or island arcs, and were carried to the North American Plate by seafloor spreading. Although the terranes are generally regionally similar, offset can occur due to crustal faulting, and metamorphism of some portions of the terrane could have occurred during the accretion process. Figure 7 is a generalized map of the accretionary terranes of southern Alaska, and Figure 8 is a generalized geologic map of the state of Alaska.

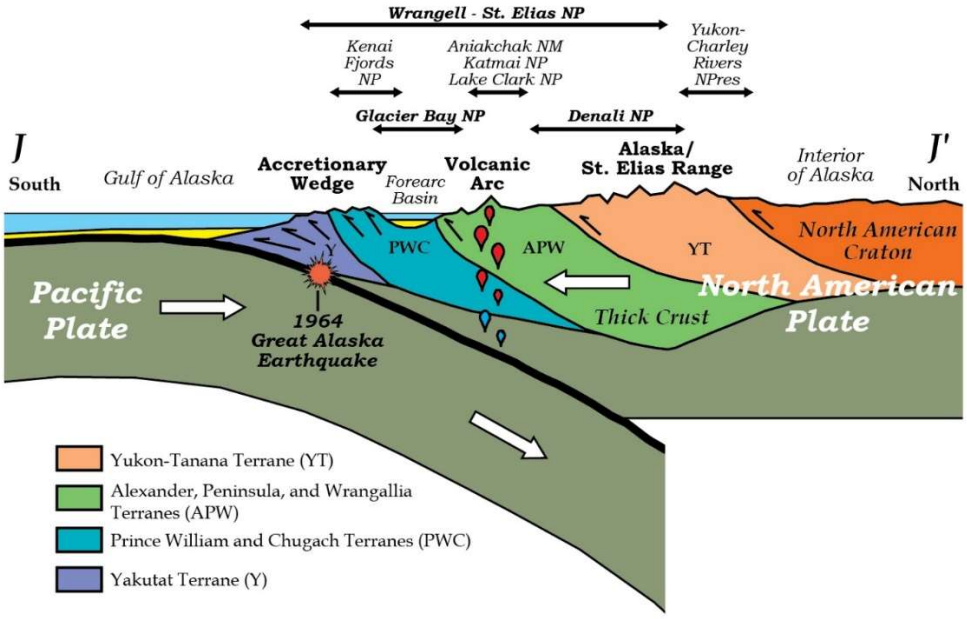

Figure 7. Generalized geology and accretionary terranes of southern Alaska (National Park Service)

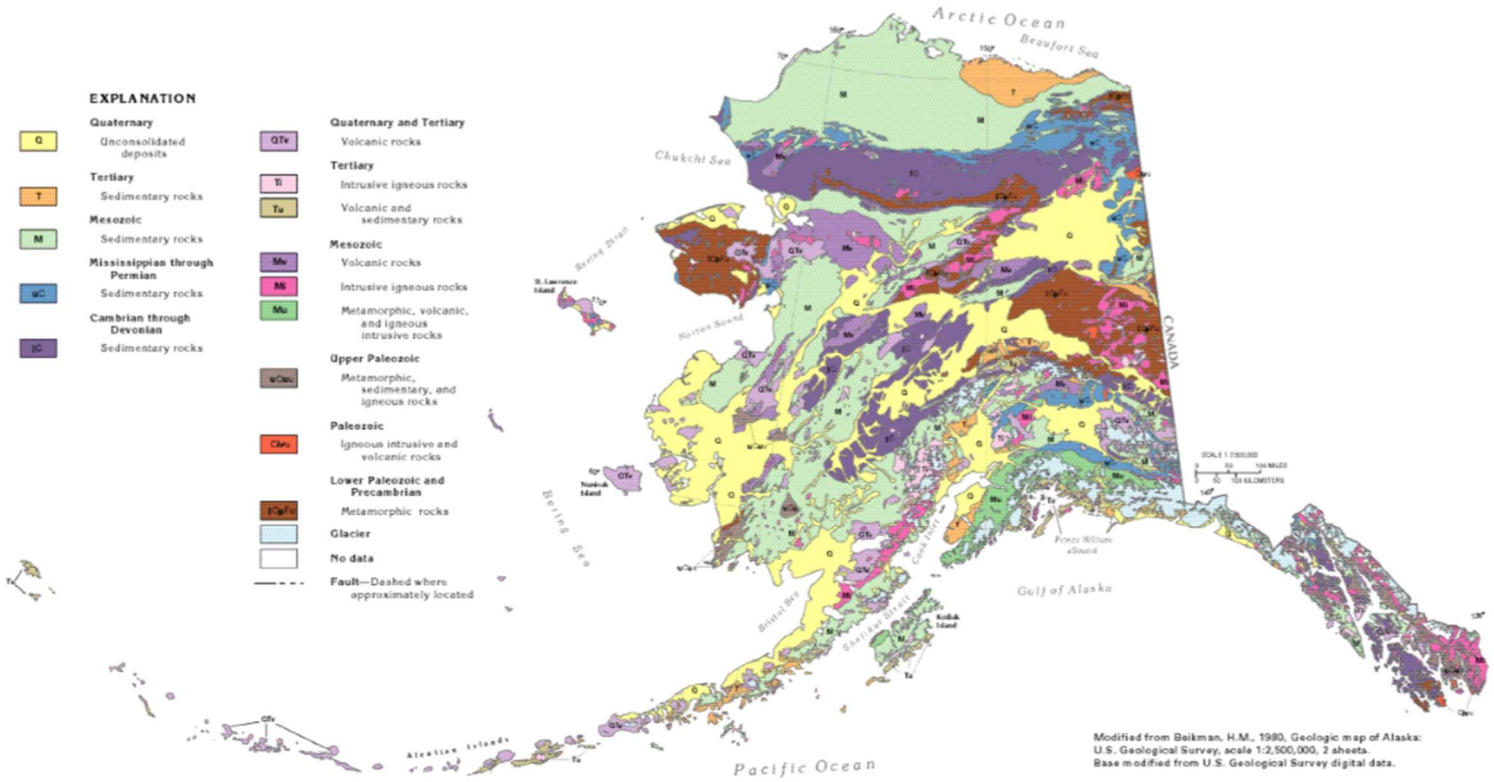

Figure 8. Generalized geologic map of the state of Alaska (Miller and Whitehead, 1999)

1.3 Geologic Setting of the Long Lake Area

A complex assortment of tilted and folded sedimentary units makes up the Matanuska Valley bordering the Glenn Highway. Accreted onto the mainland during the Tertiary period, the Peninsular Terrane comprises the Matanuska Valley (Connor, 2014). The Yakutat Plate then collided with the North American Plate, driving the uplift of the Talkeetna Mountains (Connor, 2014). While the Talkeetna Mountains were uplifting, water was eroding the mountains, and depositing sediment into alluvial fans and braided river systems in the Matanuska Valley, eventually forming the Arkose Ridge, Chickaloon,

Wishbone, and Tsadaka Formations during the Paleocene to the Oligocene Eras (Connor, 2014). The Chickaloon Formation primarily comprises the study sites adjacent to Long Lake (Wilson *et al.*, 2015). This formation is particularly characterized by its variability in rock type and structural geology (Alaska DNR, 2009). At least 3 Pleistocene-age glacial advances have since affected the Matanuska Valley at the study sites, further eroding and shaping the landscape, or depositing material in the valley bottom, depending on the climate and glacial mass balance (Alaska DNR, 2009). A large ice-dammed glacial lake, known as Lake Ahtna, flooded the Matanuska Valley at least once during the Pleistocene, further depositing material in the valley (Connor, 2014).

Two faults also border the Matanuska River Valley. Along the southern edge of the valley, the Border Ranges Fault juxtaposes the Chugach Terrane and Peninsular Terrane. The Border Ranges Fault is a long strike-slip fault formed during the terrane accretion, but has re-activated multiple times in its history, resulting in a total offset of at least 120 km (Ridgway *et al.*, 2007). Abutting the north edge of the Matanuska River Valley, the Castle Mountain Fault juxtaposes the Wrangellia Terrane and Peninsular Terrane, along with the post-accretion sediments overlying the Peninsular Terrane. The Castle Mountain Fault is approximately 200 km long, reaching from near Palmer to Tahneta Pass (Connor, 2014). The fault has produced historic seismicity and is assumed to be active, capable of producing strong earthquake shaking (Labay and Haeussler, 2001). A geologic map of the area is presented in Figure 9.

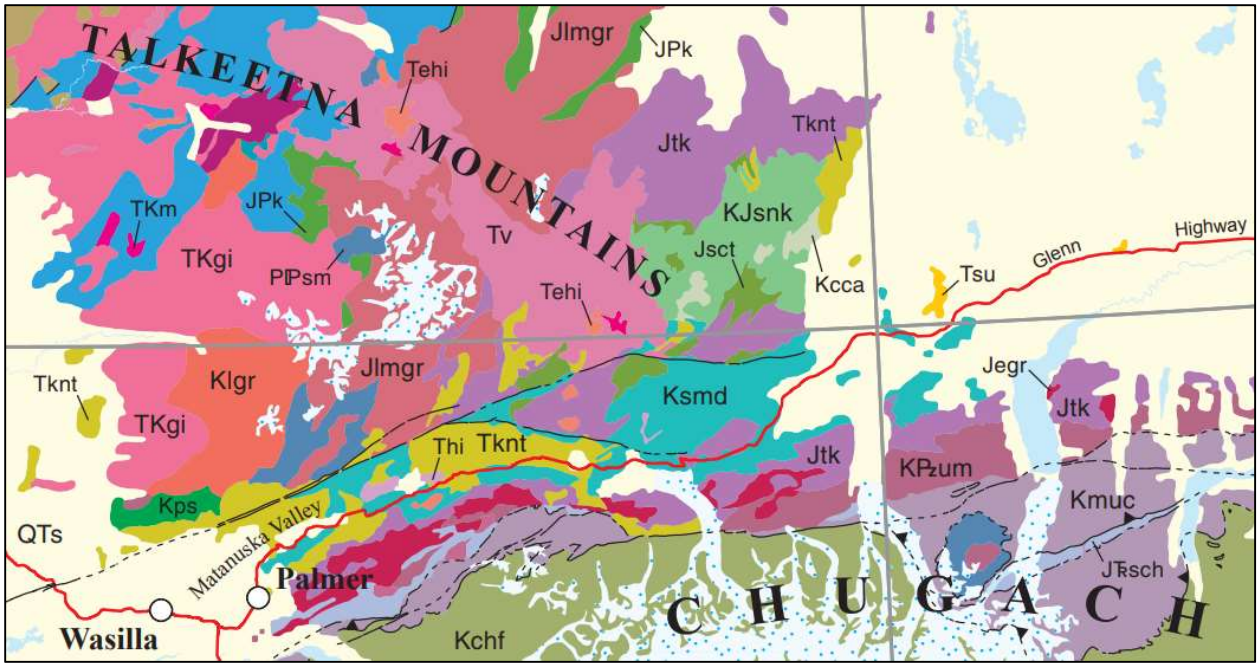

Jegr	Intermediate to mafic plutonic rocks (Early Jurassic)
Jlmgr	Plutonic rocks (Late and Middle Jurassic)
JPk	Kakhonak Complex and Tlikakila Complex of Carson and Wallace (Jurassic, Triassic, and older)
Jtk	Talkeetna Formation (Early Jurassic)
JTrsch	Blueschist of southern Alaska (Early Jurassic to Triassic)
Jsct	Shelikof and Chinitna Formations and Tuxedni Group (Middle Jurrasic)
Kcca	Coquina and calcarenite (Lower Cretaceous)
Kchf	Chugach accretionary complex (Cretaceous)
Klgr	Intermediate granitic rocks (Late Cretaceous)
Kmuc	McHugh and Uyak Complexes, and similar rocks (Late Cretaceous)
KPzum	Mafic and ultramafic rocks in southern Alaska (Cretaceous to late Paleozoic)
Tehi	Felsic dikes, sills, and small stocks in southern Alaska (Tertiary and older)
Thi	Hypabyssal intrusions (Tertiary)
TKgi	Granitic rocks of southern and interior Alaska (Tertiary, Paleocene, Cretaceous, Maastrichtian)
TKm	Mafic intrusive rocks (Tertiary to Late Cretaceous or older)
Tknt	Nearshore and nonmarine sediments in southern Alaska (Tertiary)
Tsu	Sedimentary rocks, undivided (Tertiary)
Tv	Volcanic rocks, undivided (Tertiary)
KJsnk	Staniukovich and Naknek Formations, Kotsina Conglomerate, and similar rocks of southern Alaska (Lower Cretaceous to Jurassic)
Kps	Pelitic schist (Late Cretaceous)
Ksmd	Shallow to moderate depth sedimentary rocks (Upper Cretaceous to upper Lower Cretaceous)
QTs	Unconsolidated and poorly consolidated Surficial deposits (Quaternary and upper-most Tertiary)

Figure 9. Geologic Map of the Matanuska Valley region, with the Long Lake site highlighted (Wilson et al., 2015).

1.4 Surveying, Georeferencing, and Processing Methods

High-resolution 3-dimensional LiDAR surveys have been performed at the Long Lake study sites nearly annually between 2012 and 2017. These surveys have been performed, and the models processed and georeferenced, as described in the following sections.

1.4.1 Survey Equipment and Methods

Laser scanners acquire distance measurements by sending an electromagnetic pulse towards an object. The object reflects the pulse, and the scanner receives it back. Time-of-flight is measured, and a very accurate measure of distance can be collected using the following equation.

$$D = 0.5c\Delta t$$

Where c is the speed of light and Δt is the time-of-flight.

Point clouds of our four study sites have been collected intermittently between 2012 and 2017 using this methodology. In 2012, a consultant (David Evans and Associates) conducted a Mobile LiDAR survey using a TITAN Mobile Laser Scan system. In 2013, 2014, 2015 and 2017, graduate students from Oregon State University's Geomatics Team, led by Dr. Michael Olsen, gathered data using Terrestrial Laser Scanners. In 2013, 2014, and 2015, the team used a Riegl VZ-400 TLS. In 2017, Dr. Olsen's team used a Leica ScanStation P40.

An inclinometer, a digital SLR camera (Nikon D700), and a survey-grade GPS receiver (Trimble R8 GNSS) were mounted above the TLS scanner, and atmospheric conditions were recorded to correct distance measurements for the 2013, 2014, and 2015 scan sets (Olsen *et al.*, 2015). For the TLS scan sets, scan positions were typically spaced 50 – 80 meters apart and covered a 360 degree horizontal field of view and a 100 degree vertical field of view (-30 degrees to +70 degrees from horizontal). Each scan position was occupied for at least 20 minutes, allowing time for data logging. Six photographs were

collected at each position, encompassing a 360-degree view for the 2013, 2014 and 2015 scan sets. The scanner used in 2017 takes photographs to colorize the scans automatically. Table 2**,** below, shows average point spacing for all sites for all change epochs. Figures 10 through 13 show images of the 2017 point clouds as well.

	2012	2013	2014	2015	2017
Long Lake 71	N/A	2.76	1.51	1.51	0.90
Long Lake 85.5	5.74	1.03	0.91	0.59	0.45
Long Lake 86.9	3.00	N/A	N/A	1.08	1.17
Long Lake 87	7.89	1.12	N/A	0.79	0.59

Table 2. Average Point Spacing for the Scans (cm)

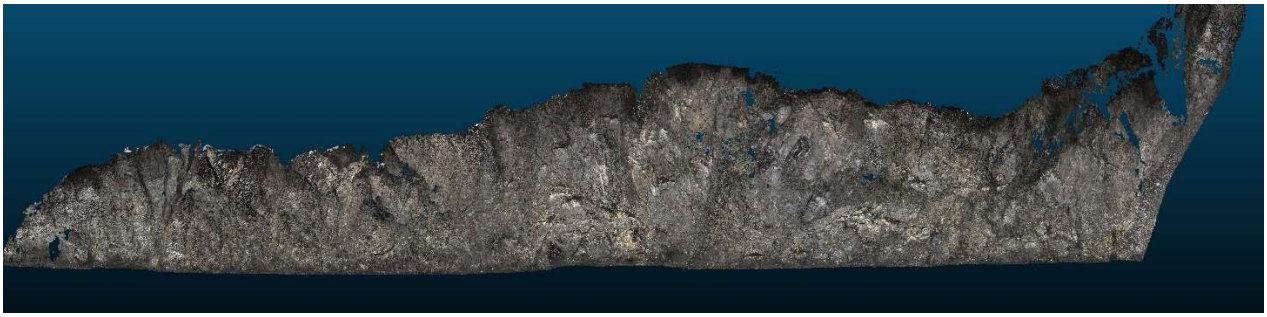

Figure 10. Point Cloud of LL71, 2017

Figure 11. Point Cloud of LL85.5, 2017

Figure 12. Point Cloud of LL87, 2017

Figure 13. Point Cloud of LL87, 2017

1.4.2 Processing and Georeferencing Methods

Each TLS scan was recorded in its own coordinate system. The scans were transformed into a common coordinate system (Alaska State Plane Coordinate System Zone 4, North American Datum 1983 (2011) Epoch 2010.00, Geoid 12A) per the process outlined in Olsen *et al.,* 2015. The 2012 mobile scans were georeferenced using reflective ground control markers, the locations established using a total station with an RTK GPS device. Olsen e*t al.* (2015) provides the details of the geo-referencing methods.

Manual cropping and editing was then performed. Unwanted data, such as passing vehicles, moisture in the air, the road surface, or thickly vegetated patches, were manually cropped from the point clouds using Maptek I-Site Studio and Leica Cyclone. Areas with more sparse vegetation, and adequate ground point coverage, were filtered using a ground filtering algorithm developed by the OSU Geomatics team headed by Dr. Olsen.

A surface model was then generated from the point clouds, on a 5-centimeter grid. Each representative grid point location is selected as the average location of cloud points in the vicinity of that grid point. It was also deemed necessary to perform a hole filling operation, using a Thin Plate Spline technique, to approximate the surface where there are small data gaps. When change occurs near data gaps, the volume of change can be miscalculated, and the hole filling aims to correct this. These methods are outlined in detail in Olsen *et al.*, 2015. An example of the raw point cloud and surface model generation (with filled holes in pink) is shown in Figures 14 and 15.

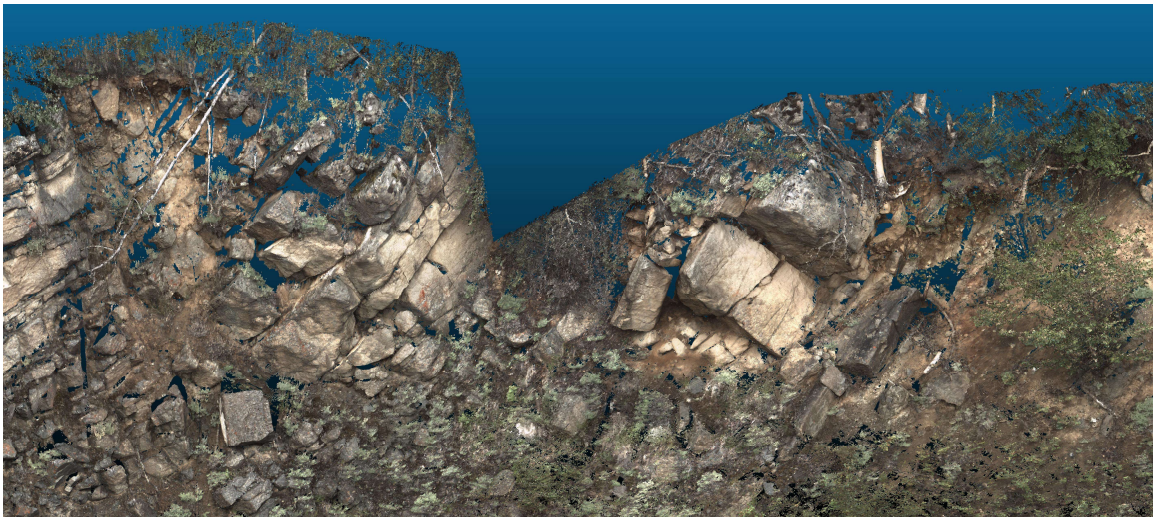

Figure 14. Raw Point Cloud Data.

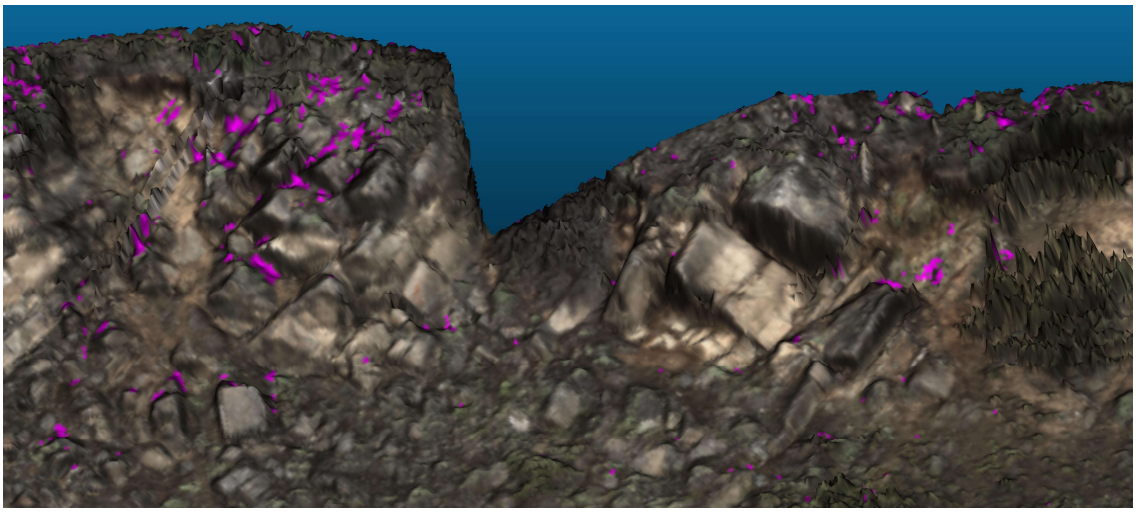

Figure 15. Surface Generation

1.5 The Rockfall Activity Index (RAI) – A Method for Rock-Slope Hazard Assessment

The Rockfall Activity Index (RAI) (Dunham *et al.*, 2017) was developed as a rock slope hazard classification methodology utilizing high-resolution 3-dimensional LiDAR point clouds. Work is being done to extend the methodology for use with other high-resolution 3-dimensional model of rock slopes, such as structure-from-motion (SfM) photogrammetry models. The system aims to provide a rock-slope hazard rating to distinct slope areas based on parameters found in the point clouds of each rock-slope.

The RAI system uses local surface slope and surface roughness measurements to map morphological characteristics and erosional processes of the slope, assigning a classification to the various regions on the slope face. The system aims to strike a balance between classifying the slope too finely, resulting in discontinuous process mapping, and classifying the slope too roughly, resulting in resolution loss. 7 geomorphologic classifications, as shown in Table 3**,** were selected to adequately map rock-slope morphology. The classification procedure flow chart is shown in Figure 16**.**

Morphological classification	Description
Widely to moderately spaced discontinuous rock (D_w)	Intact blocks or fragments of rock separated by discontinuities typically spaced at ~30 cm or greater
Closely spaced discontinuous rock (D_c)	Intact blocks or fragments of rock separated by discontinuities typically spaced between ~10 cm and ~20 cm
Fragmented discontinuous rock (D_f)	Intact blocks or fragments of rock separated by discontinuities with a typical spacing of less than ~10 cm
Intact rock (I)	Rockmass with few or relatively minor discontinuities
Cantilevered overhang (O_c)	Overhanging rock whose lower portion is inclined at less than 120° [see Fig. 1]
Steep overhang (O_s)	Overhanging rock whose lower portion is inclined at greater (i.e., steeper) than 120° [see Fig. 1]
Talus (T)[d]	Mass wasting-derived rock fragments (debris) accumulated at the base of a slope, or along benches within a slope

Table 3. The 7 RAI morphological classifications (Dunham et al., 2017)

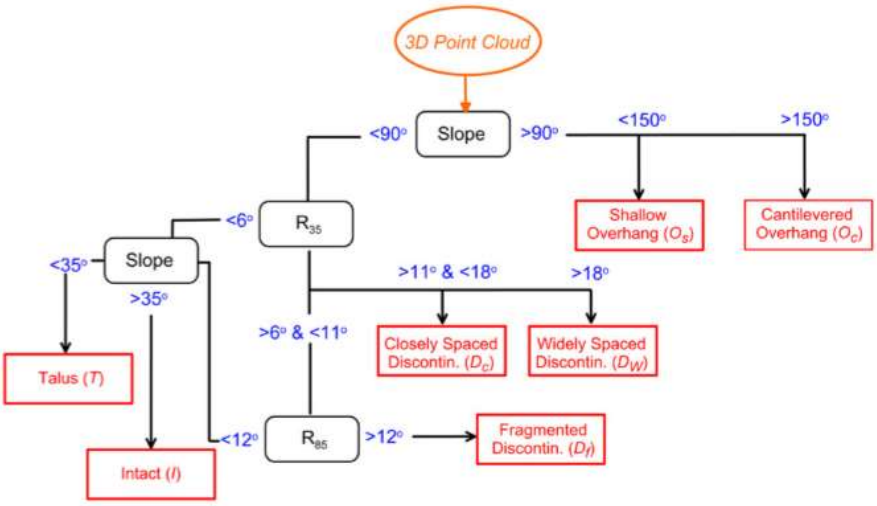

Figure 16. RAI System surface classification algorithm (Dunham et al., 2017)

The system associates each classification with an average failure rate and failure size, that had been derived from limited observation of failure occurrences over one year of data for one site. This failure rate and size, along with the point location along the slope face, is used to calculate an annual kinetic energy release (the "RAI Score") from each point of a 5-cm-spaced grid along the slope face, to the road surface. Figure 17, below, shows an example of the output of the RAI methodology for one of the study sites.

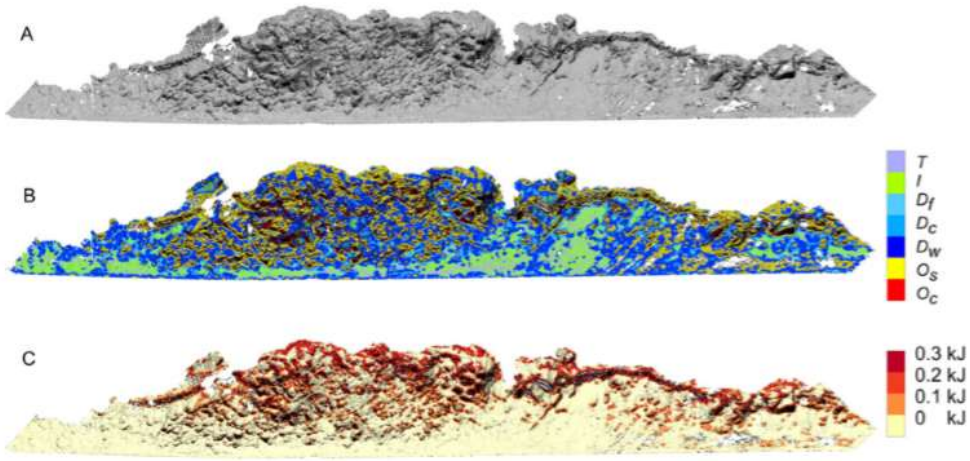

Figure 17. Output of the RAI methodology at Site LL85.5 (Dunham et al., 2017)

One goal of the current research is to assess the efficacy of the RAI methodology by identifying whether or not the roughness thresholds and window sizes adequately differentiate between different rock-mass geomorphologic processes, and identifying whether the selected failure rates and failure sizes are adequately representing events associated with the various RAI classifications.

1.6 Rock-slope Change Detection Techniques

Software developed by Dr. Olsen works to isolate and report individual change events when surveys of the same rock-slope are conducted at different time intervals (Olsen *et al.*, 2015). The two

vegetation-filtered surface models, represented as Digital Elevation Models (i.e., DEMs, in 2.5-Dimensional space), are compared in order to compute a grid of distances between the two models.

A significant change threshold is then employed to determine which cells most likely changed from one year to another. If the distance between two points on the grid is smaller than the significant change threshold, the cell will not be flagged as changed. This serves to alleviate noise associated with sampling or georeferencing errors. Deviating from Olsen *et al.* 2015, a significant change threshold γ as low as 0.03 meters was selected for much of this work; previous work had only analyzed significant change of 0.05 meters. Where applicable, lowering the significant change threshold provides the opportunity to extend the size range of detectable failures, though it presents increased likelihood of falsely identified failure events.

If the changed cell is adjacent to one or more other changed cells, it is part of a change cluster. Each change cluster is reported with a unique change identification number. The change distance for each cell, along with the area representation of each cell, is used to compute a change volume for each cell. Change volumes for all cells in a change cluster are combined to find the total volume of the change event. Positive and negative change (accreted and eroded cells) are differentiated and will not be clustered together; these events have unique change identification number sets as well.

Four epochs of change have been recorded at LL85.5, LL86.9 and LL87. These change epochs include the periods between 2012 and 2013, between 2013 and 2014, between 2014 and 2015, and between 2015 and 2017. Only three epochs of change have been recorded at LL71: 2013 to 2014, 2014 to 2015, and 2015 to 2017.

1.6.1 Sources of Error in Detecting Rockfall Events

While manually inspecting the change grid and raw point clouds, it was discovered that not all identified failure clusters represented actual rockfall events. Generally, these errors in identifying failure clusters can be categorized into two sources. Firstly, excessive vegetation on slope areas can cause the misidentification of failures. Secondly, complex 3-dimensional geometries observed on the slope face hinder our ability to accurately identify failure. Both sources are exasperated by the increase in scan resolution through time, as equipment, technology, and scanning methods improve. These sources of error are described in further detail below.

The presence of vegetation was observed to trigger errantly reported rock-slope failures several ways. Firstly, vegetation can actually grow, fall, or move, which becomes identified as a rock-slope erosion or accretion by the change detection software. Falling vegetation does not represent the same hazard as rockfall, nor is it necessarily related to rock-slope geomorphologic processes, and therefore should be ignored in the discussion of rock-slope geomorphologic processes. Also, vegetation can be scanned differently year-to-year, leading to different interpretations of the ground surface. Because LiDAR pulses can "penetrate" vegetation, by finding gaps through it, some ground points and some vegetation points are represented in the point cloud. In later scans, when resolution improved, more ground points were recorded in proportion to the vegetation points. When the ground filtering algorithm was used, the ground surface in later, higher-resolution scan years was estimated lower than in earlier, lower-resolution scan years; this can then be errantly identified as a rock-slope failure. See Figures 18 and 19 for a graphical representation of this phenomenon.

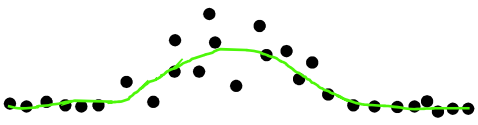

Figure 18. Example of a cloud of points on vegetation with low point density, and the corresponding surface generation

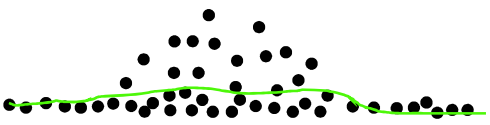

Figure 19. Example of a cloud of points on vegetation with high point density, and the corresponding surface generation

Relatively large-scale, complex 3-dimensional geometries are another source of potential error in the change detection techniques. Very blocky terrain, with protrusions and concavities much larger than the scale of the failures we aim to identify, provide challenges in determining locations of real change, and discerning them from apparent change due to sampling errors. Firstly, increases in point sampling resolution through time will result in concavities being more fully recognized, rather than being assumed to be flat. Figures 20 and 21 demonstrate this problem.

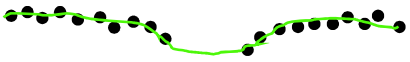

Figure 20. Example of a cloud of points at a concavity with low point density, and the corresponding surface generation

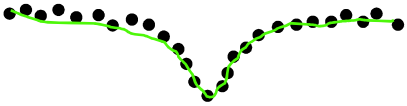

Figure 21. Example of a cloud of points at a concavity with high point density, and the corresponding surface generation

Additionally, overhangs in the perspective of the best-fit-plane for the DEM will cause problems with surface generation, and the surface generated in one scan is unlikely to be generated the same in a subsequent scan, due to resolution and point sampling differences. Figures 22 and 23 demonstrate this problem.

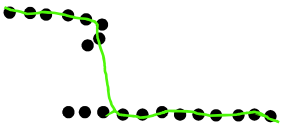

Figure 22. Example of a cloud of points at an overhang with low point density, and the corresponding surface generation.

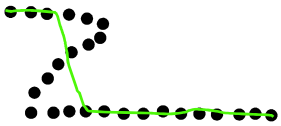

Figure 23. Example of a cloud of points at an overhang with high point density, and the corresponding surface generation.

Surfaces parallel to the normal of the DEM best-fit-plane are also much more likely to trigger change identification, because the significant change threshold is measured along the normal of the best-fit plane. Change on surfaces that are perpendicular to the normal, or generally parallel to the best-

fit-plane, is more likely to be filtered out due to the significant change threshold. Therefore, in overhangs and corners, significant change is far more likely to be identified, although it may just have been caused by slight (<.01 meter) offset in the scans.

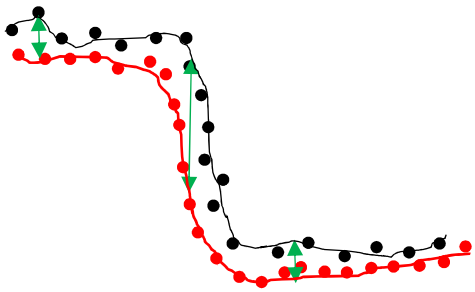

Figure 24. Example of a location in which the distance between surfaces that are parallel to the normal is exaggerated.

During the manual verification of failure identification process (see Section 1.6.5), it was also noted that, in the talus at the base of several slopes, tracks from construction equipment were observed in the identified failure clusters. These events bordering the road surface, that were obviously caused by human activity, were omitted from analyses, to negate their influence on the computation of natural erosion rates.

Figures 25 through 28 show the distributions of failures across the four study sites for the 2015-2017 change epoch. Across all epochs and sites, a total of 4,221 properly-identified failures were included in the data set.

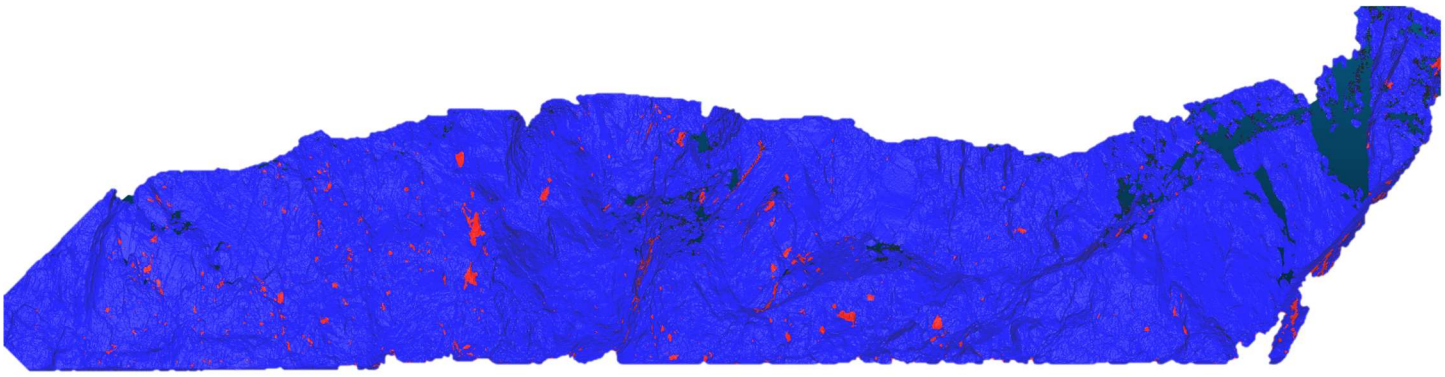

Figure 25. Failures at LL71 for the 2015-2017 Change Epoch.

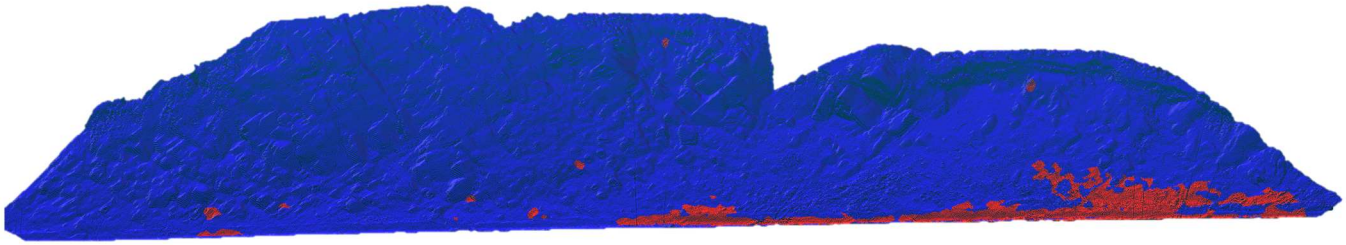

Figure 26. Failures at LL85.5 for the 2015-2017 Change Epoch.

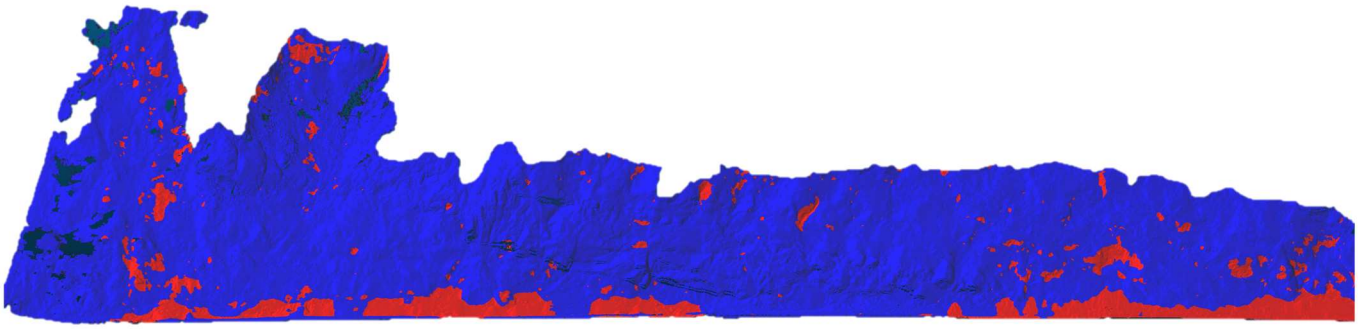

Figure 27. Failures at LL86.9 for the 2015-2017 Change Epoch.

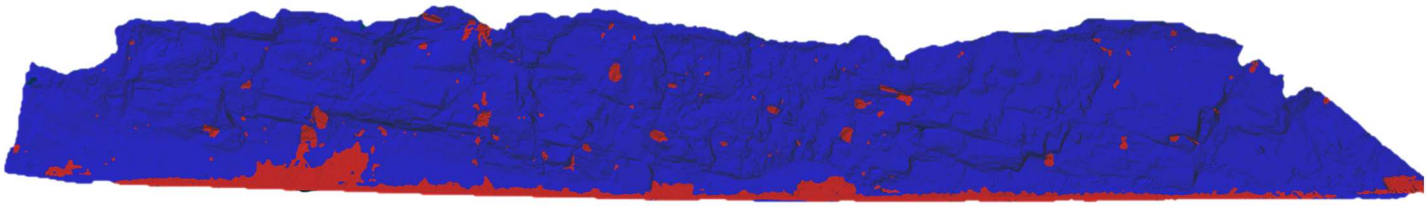

Figure 28. Failures at LL87 for the 2015-2017 Change Epoch.

1.6.2 Quantifying the Accuracy of the Change Detection Algorithm

To understand the extent of errors made identifying change, and the influence of human-activated change, change curves, size-frequency parameters (see Section 2.1), and erosion flux projections were compared for manually filtered and non-filtered change data. The intent is to determine if manual verification of change identifications is necessary in order to rely on change data. Table 4, below, shows the distributions of derived size-frequency parameters, β and α, and erosion flux values, for the key sites, when identified failure events are taken directly from the software, and when they are manually filtered.

Year & Site	Unfiltered Beta	Filtered Beta	Unfiltered Alpha	Filtered Alpha	Unfiltered Recession Rate (m/yr)	Filtered Recession Rate (m/yr)
2012-2013						
LL85.5	2.739	0.454	1.521	1.524	0.0144	0.0008
LL86.9	0.940	1.400	1.792	1.754	0.0032	0.0021
LL87	2.338	0.429	1.756	1.513	0.0091	0.0013
2013-2014						
LL85.5	4.947	0.669	1.645	1.494	0.0127	0.0010
LL86.9	1.633	1.157	1.845	1.787	0.0079	0.0051
LL87	1.734	0.547	1.859	1.814	0.0084	0.0018
LL71	1.172	0.478	1.769	1.717	0.0108	0.0055
2014-2015						
LL85.5	0.907	0.849	2.088	1.445	0.0066	0.0025
LL86.9	0.745	0.558	1.966	1.914	0.0037	0.0025
LL87	0.581	0.261	1.993	1.888	-	0.0011
LL71	1.345	0.416	1.814	1.805	0.0096	0.0034
2015-2017						
LL85.5	0.247	0.353	2.361	1.690	0.0028	0.0001
LL86.9	1.006	0.825	1.634	1.581	0.0050	0.0032
LL87	1.070	0.616	1.796	1.598	0.0067	0.0024
LL71	0.721	0.261	1.752	1.759	0.0065	0.0021

Table 4. Distribution of Size-Frequency parameters & Recession Rate measurements (based on Alpha and Beta parameters) between unfiltered and filtered data.

Figures 29 through 32 contain size-frequency plots of the change data, both manually filtered and raw, for the highest-resolution (2015-2017) change epoch.

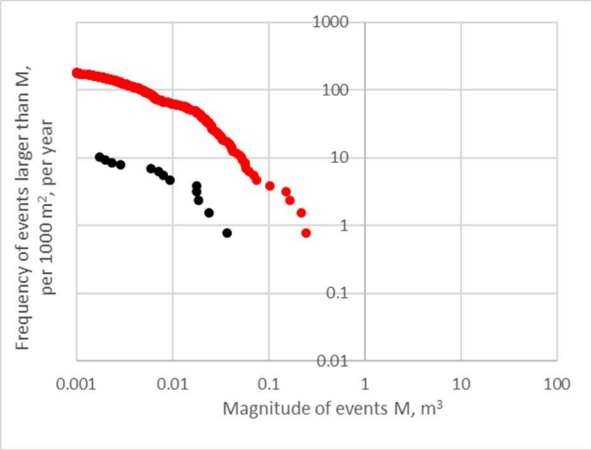

Figure 29. LL85.5 Change Data, comparison of manually filtered (black) and unfiltered (red) data.

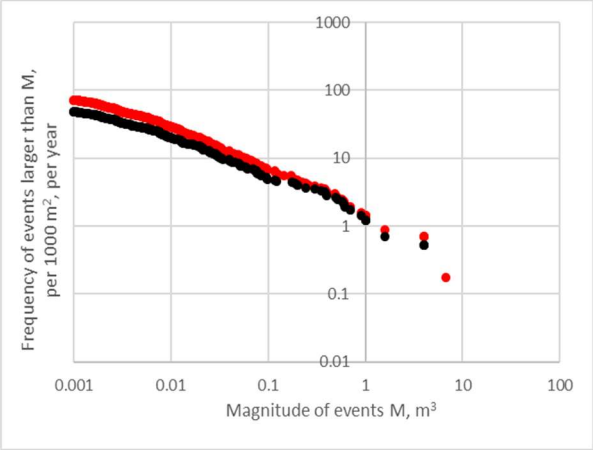

Figure 30. LL86.9 Change Data, comparison of manually Filtered (black) and unfiltered (red) data.

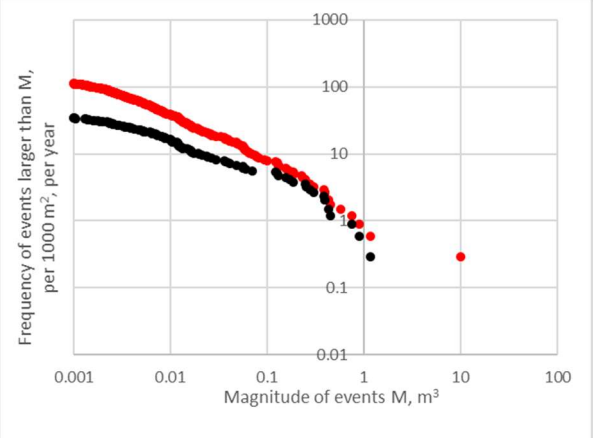

Figure 31. LL87 Change Data, comparison of manually filtered (black) and unfiltered (red) data.

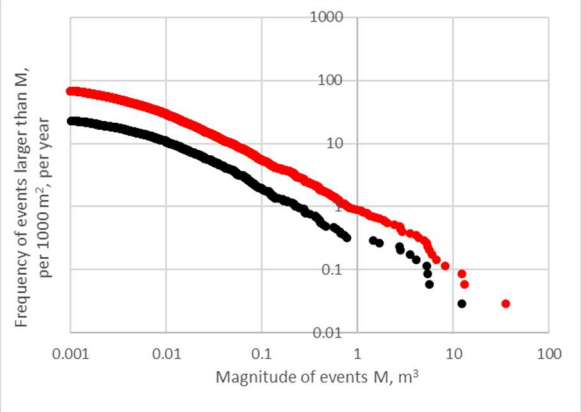

Figure 32. LL71 Change Data, comparison of manually filtered (black) and unfiltered (red) data.

Several points of interest should be noted from these figures and the table. The change detection software seems to generally assign the size distribution of failures fairly accurately, resulting in a somewhat accurate value for the scaling parameter, α. The plots above reinforce this; they are mostly

shifted up or down, and rarely skewed. Some outliers indicate that this is not always the case, though. For example, in Figure 31, above, the scaling parameter is much higher in the unfiltered data than the filtered data, and the discrepancy between unfiltered and filtered curves are non-uniform across size ranges. The activity parameter (the y-intercept) varies greatly between the manually filtered and unfiltered data. This discrepancy can also be seen in the measured erosion flux values; the unfiltered data has much higher erosion fluxes than the unfiltered data.

It is also notable that the fluctuation in the scaling parameter, α, the activity parameter, β, and the erosion flux volume between unfiltered and filtered data is less pronounced at LL86.9. LL86.9 is generally much more planar, and less geometrically complex, than the other sites. The blocky surfaces at LL85.5, LL87, and LL71 produce more erroneous failure identifications. Many of the Glitter Gulch sites also contain planar terrain. Although these sites have not been investigated for this thesis, it is likely that the change detection software will produce results with higher accuracy at the Glitter Gulch sites.

From this data, it becomes apparent that, for the purposes of this paper, manual verification of change detection data is necessary for meaningful analyses and results. In order to increase efficiencies of this system, corrections will need to be made to the change detection software and ground clutter filtering algorithm to improve accuracy of identifying change.

1.6.3 The Influence of RAI Class and Failure Size on Change Detection Accuracy

An analysis was conducted to see which failure sizes and in which slope areas change is being errantly identified. The following table, Table 5**,** shows the probability of failures being correctly identified, as a function of both failure size and RAI classification.

Failure Size (m^3)	0.001-0.005	0.005-0.01	0.01-0.05	0.05-0.1	0.1-0.5	0.5-1.0	1.0-5.0	5.0-10.0
Probability of Successful ID	0.337	0.336	0.342	0.402	0.381	0.387	0.467	0.500
RAI Class	Unclass. (0)	Talus (1)	Intact (2)	10cm Disc (3)	20cm Disc (4)	30cm Disc (5)	Shall Over (6)	Steep Over (7)
Probability of Successful ID	0.040	0.739	0.462	0.349	0.307	0.107	0.333	0.165

Table 5. Probability of successful identification of failures, for different failure sizes, and different RAI Classifications

Failures are slightly more likely to be properly identified by the change detection algorithm if they are larger in volume. The relationship is not significant, however; generally, all failure scales are being errantly identified. Failures are most likely to be properly identified by the change detection algorithm in the Talus RAI Class, followed by Intact Rock, followed by the discontinuity classes and shallow overhangs. This shows that roughness scales with probability of errant identification of failure; rougher surfaces are more likely to be errantly identified as change. Flat overhangs and very rough areas are very likely to be errantly identified. Unclassified slope area is most likely to be errantly identified as a failure. The table below, Table 6**,** shows the likelihood of proper identification of failures in the different change epochs, and at the different sites.

Change Epoch	2012-2013	2013-2014	2014-2015	2015-2017
Probability of Successful ID	0.079	0.289	0.322	0.310
Site	LL85.5	LL86.9	LL87	LL71
Probability of Successful ID	0.053	0.579	0.208	0.309

Table 6. Probability of successful identification of failures, for each change epoch and each site.

Failures are very likely to be identified errantly in the 2012-2013 change epoch, likely attributed to the lower scan resolution and poorer survey control during the 2012 mobile LiDAR campaign. Failures in the 2013-2014, 2014-2015 and 2015-2017 change epochs were errantly identified at a similar rate,

indicating that a further increase in scan resolution will likely not solve the issues directly. Failures are most likely to be errantly identified at site LL85.5, which can be attributed to the complexity of the geometries of the rock slope at that site. At Site LL86.9, the success rate is much greater, indicative of the relatively planar nature of that site. LL87 and LL71 contain both planar and geometrically complex areas, attributing their more average failure identification success rates.

1.6.4 Suggested Modifications to Change Detection Methodologies

Firstly, vegetation filtering methodologies could be improved. Currently, the algorithm assumes that any points outside of a certain range of the average surface location is vegetation. When the ground surface data is sparse, or geometric complexities are abundant, the vegetation filter may filter out points that are actually part of the rock-slope surface, or may not filter out vegetation points properly. Other techniques have been shown to handle the challenges of lower-resolution ground points or geometric complexity, with some calibration. For example, Kassebaum (2012) presents a methodology that attempts to travel along the rock-slope surface and differentiate between it and other noise; the method presented is computationally expensive, however. Experimenting with other methods may be beneficial, though vegetation does not appear to be the source of most error in change detection.

As previously discussed, 2.5-dimensional change detection has significant challenges on geometrically complex rock-slopes. Previous researchers have also found that 2.5-dimensional change detection hinders our ability to accurately quantify rock-slope recession (Abellan *et al.*, 2014). For example, deviating the viewing angle slightly has been shown to cause significant changes in rock-slope change detected by the algorithms (Benjamin *et al.*, 2016). Researchers have found that Cloud-to-Mesh

techniques, even in three dimensions, are difficult to employ accurately on rough and complex surfaces with extreme topographic variability (Olsen *et al.*, 2015).

Cloud-to-cloud techniques, however, have been shown to provide a good approximation of the true position of the rock-slope surfaces. Generally, significantly higher erosion values are measured using 2.5-dimensional change detection techniques, than when 3-dimensional techniques are used (Benjamin *et al.*, 2016). Employing cloud-to-cloud techniques, or 3-dimensional cloud-to-mesh techniques, would be beneficial to properly identify change along the rock-slope. Alternatively, 2.5-dimensional methods could be improved by rotating the point cloud when the surface normal strays towards perpendicular from the viewing angle, and recalculating a surface and the change grid at a different viewing angle.

1.6.5 Manual Verification of Change Detection Output

Failure data produced by Dr. Olsen's software provides the basis for this research. For this reason, along with the decreased significant change threshold and problems caused by vegetation, complex geometry, and scan resolution change, it was determined necessary to validate the accuracy of the change detection procedures. The main study sites, Long Lake 71, Long Lake 85.5, Long Lake 86.9, and Long Lake 87, for all surveyed change epochs, were manually checked for failure identification accuracy. Each identified failure cluster was examined in Maptek I-Site Studio to determine whether the failure actually existed, or if the aforementioned complexities caused misidentification of the failure cluster.

1.6.6 Quantifying the Influence of Scan Resolution on Change Data

A sensitivity analysis was conducted to determine whether scan resolution has a measurable impact on the derived size-frequency parameters and measured erosion flux volumes. This analysis was performed on the 2013-2014 and 2014-2015 data sets for LL71, because the size of the site provides an adequate sample size. The site was two-dimensionally gridded into 5m by 5m cells, and the scan resolution of each cell was approximated by counting the number of scan points within the cell, and dividing by the 2-dimensional cell area, to derive a resolution in points/m^2. Adjustments were made to account for data gaps. This procedure was completed for both the baseline and subsequent scan sets, and the minimum resolution between the two was used for analysis. Note several imperfections with this method. One imperfection stems from the projection into 2-dimensional space. If a cell contains a highly irregular surface or a surface non-parallel to the projection plane, the point spacing will be underestimated. The measurement will be denser than reality. Also, note in the scan resolution maps in Figures 34 and 35 that scan resolutions are typically clumped, and are typically higher at lower elevations along the slope. These could also be areas that happen to contain distinct erosional processes. For example, the high-resolution data at the base of the site is more likely to capture depositional talus slopes, because these slopes are more likely to exist at the base of the site. Whereas talus slopes are less likely to appear at the top of slope, where scan resolution is lower. In other words, correlation may not necessarily imply causation, due to issues with the ability to set a control in this experiment.

Figures 33 through 35 show a hillshade for LL71, and the 5m x 5m analysis grid colored to scan resolution for the 2013-2014 and 2014-2015 data sets. 3 classifications were selected when examining scan resolution, labeled “Low Resolution”, “Medium Resolution”, and “High Resolution”. These classifications were selected relative to the overall scan resolution, so thresholds for these classifications

were different between the two investigated data sets. For 2013-2014, “Low Resolution” indicates average point spacing above 0.033m. “Medium Resolution” indicates average point spacing above 0.024m. “High Resolution” indicates average point spacing below 0.024m. For 2014-2015, because the scan resolution is generally higher, resolution classifications were shifted down. “Low Resolution” indicates average point spacing above 0.016m, “Medium Resolution” indicates average point spacing above 0.011m, “High Resolution” indicates average point spacing below 0.011m.

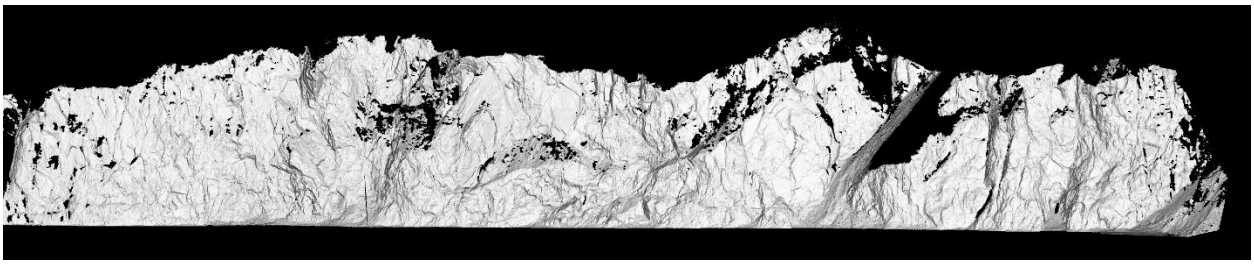

Figure 33. Hillshade of site Long Lake 71. Extremely low resolution data at the west (left) end was omitted.

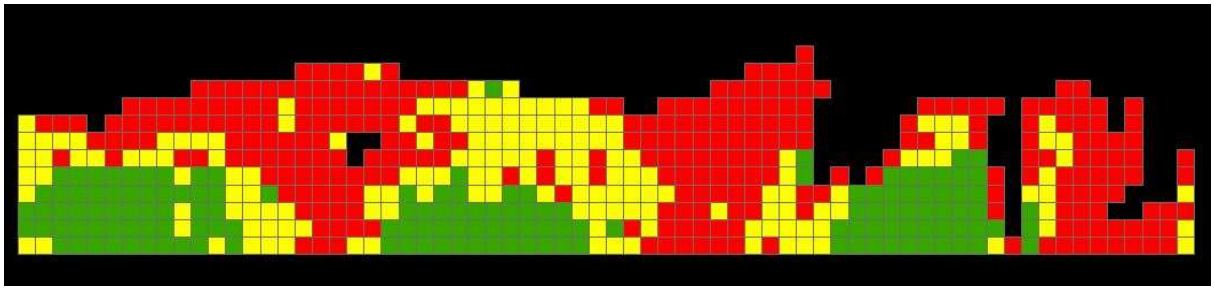

Figure 34. 2013-2014 LL71 Scan Resolution Map. Green indicates average point spacing below 2.4 cm. Yellow indicates average point spacing between 2.4 and 3.3 cm. Red indicates point spacing above 3.3 cm.

.

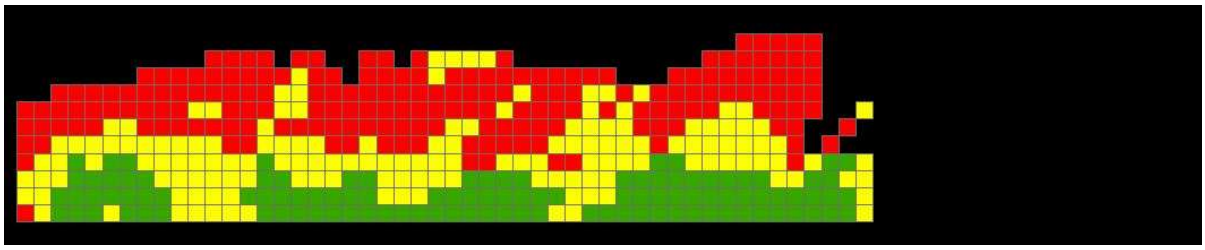

Figure 35. 2014-2015 LL71 Scan Resolution Map. Green indicates average point spacing below 1.1 cm. Yellow indicates point spacing between 1.1 & 1.6 cm. Red indicates point spacing above 1.6 cm. Note that the 2015 scan did not extend as far east as the 2013 and 2014 scans.

Note that the distribution of resolution classes follows the same general trends from year to year. This is a result of meticulous planning of the TLS surveys, stationing the scanner in similar locations every year. Scanner to target distance, and the presence of vegetation or other noise, influence scan resolution. Figures 36 and 37 are cumulative size-frequency distributions for events occurring in each of the resolution classes for 2013-2014 and 2014-2015 data sets. Table 7 lists the derived size-frequency parameters and estimated volume flux for each resolution class.

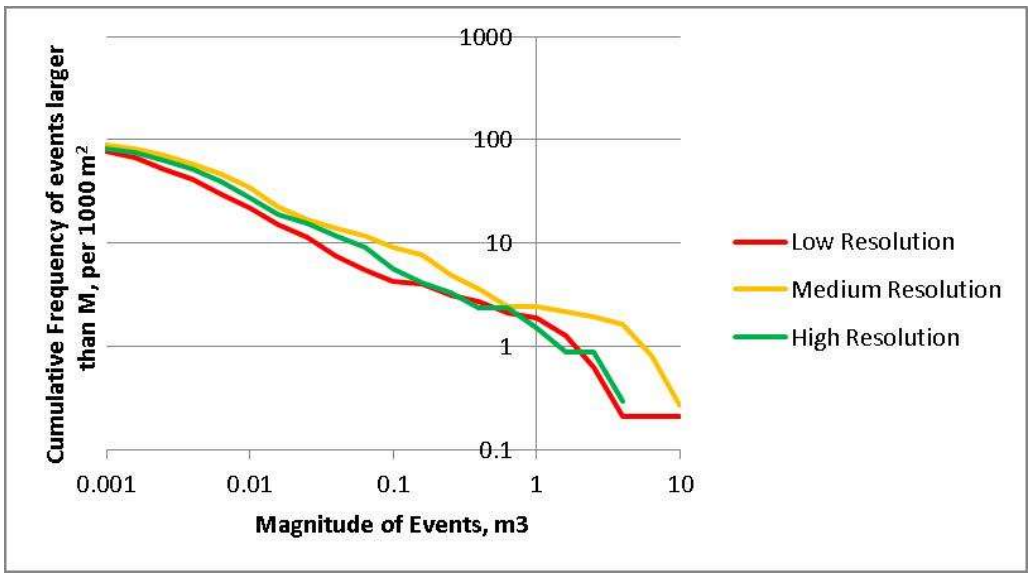

Figure 36. LL71, 2013-2014 size-frequency distribution for the 3 resolution classes

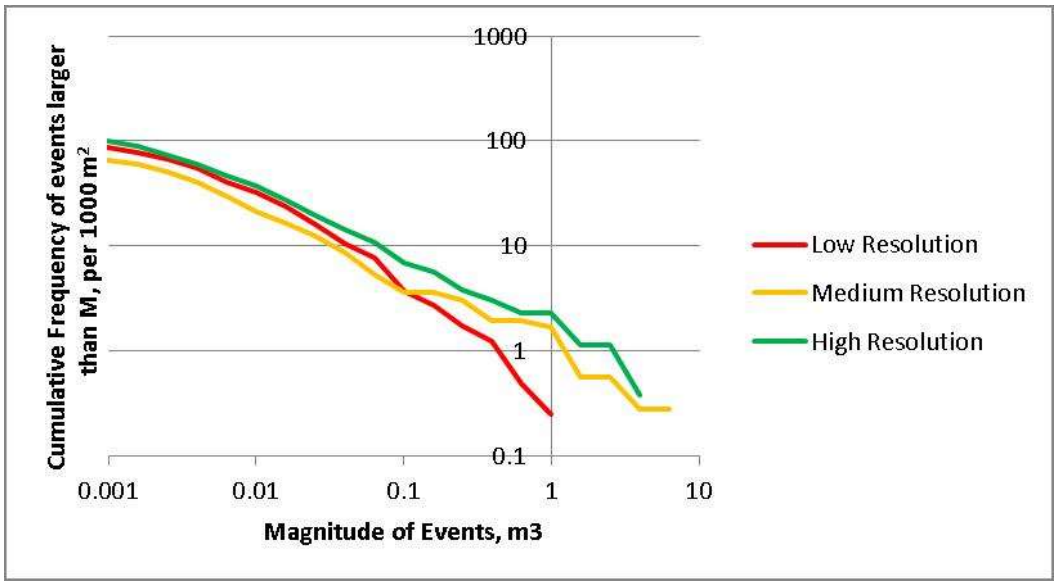

Figure 37. LL71, 2014-2015 size-frequency distribution for the 3 resolution classes

Resolution Classification	Activity Parameter, β	Scaling Parameter, α	Annual Recession Rate (m/yr)
2013-2014			
Low	0.709	1.654	.0072
Medium	2.304	1.575	.0148
High	0.859	1.66	.0073
2014-2015			
Low	0.41	1.879	.0026
Medium	0.672	1.659	.0057
High	1.077	1.653	.0080

Table 7. Derived size-frequency parameters and associated recession rates from the different resolution classes.

Although deviations exist in the size-frequency plots and derived parameters, the deviations are not primarily driven by small-sized failures. If size-frequency parameters were influenced by scan resolution, one would expect the lower size ranges to drive the differences. However, the larger size ranges are the driving factor in deviations between resolution classes, indicating that we are observing

actual geomorphological differences in the various regions of the slope. Therefore, it can be deduced that the scan resolution will not influence size-frequency parameter estimation in this study, in the ranges of scan resolutions that we are concerned with.

1.6.6 Quantifying the Influence of Temporal Resolution on Change Data

The effect of temporal censorship on change data was also investigated in this study. Long Lake Site 86.9 was analyzed in this study, since change identification is relatively accurate here; note that these analyses were performed on change data that was not manually verified. Change data between 2013 and 2017 was investigated. In one set, change detection was performed for both the 2013-2015 epoch and the 2015-2017 epoch, and combined to produce a 2013-2017 cumulative size-frequency distribution (2-year scan interval). In the other set, change detection was only performed for one 2013-2017 epoch (4-year scan interval). Plots of the two analyses are shown in Figure 38 below.

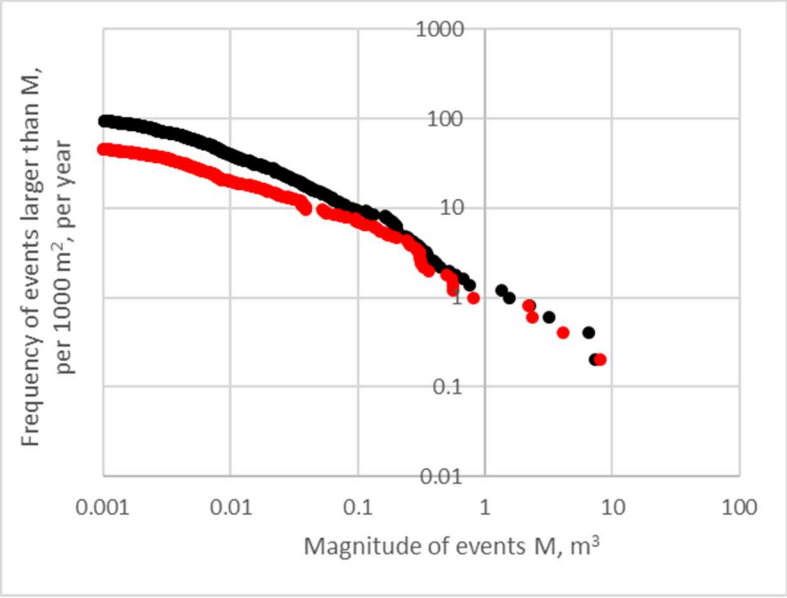

Figure 38. LL86.9 size-frequency distribution for a 2-year scan interval

Scan Interval	Activity Parameter, β	Scaling Parameter, α	Annual Recession Rate (m/yr)
2-year	1.154	1.785	.00784
4-year	0.857	1.711	.00562

Table 8. LL86.9 size-frequency parameters for a 2-year scan interval and

The scaling parameter, α, is noticeably smaller in the 4-year scan interval data than the 2-year scan interval data. Distinct smaller failures can overlap and be identified as larger failures in longer scan intervals. This effect is likely contributing to the difference in the calculation of α.

The activity rates between the two intervals are also noticeably different. This is likely due to errors in change detection; with two 2-year scan intervals, problematic regions of the slope can be errantly identified as change twice. If no change detection errors were present, the annual erosion flux for the 2-year and 4-year scan intervals would be approximately equal. Figure 39, below, shows the two curves normalized so erosion flux is equal. This normalization assumes that errant detection occurs at the same rate across all size ranges (an assumption that often holds true).

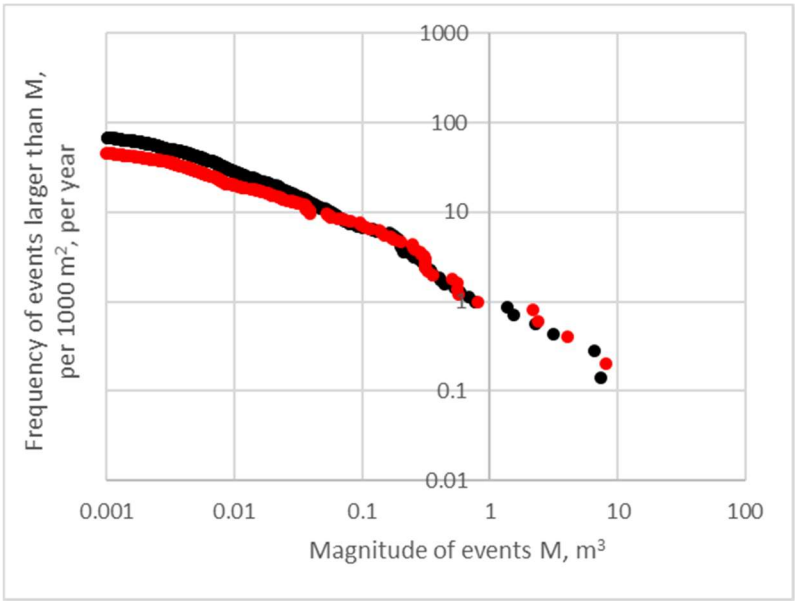

Figure 39. LL86.9 size-frequency distribution for a 2-year scan interval (black) and a 4-year scan interval (red), normalized by volume flux

2. Rock-Slope Failure Data

2.1 Power-Law Scaling of Natural Phenomena

Many natural phenomena have been shown to demonstrate self-organized criticality. When certain dynamic systems seek some natural equilibrium, they will often self-organize into a power-law size-frequency distribution. Forest Fires (Hergarten, 2003), species extinction events, nuclear chain reactions (Hergarten, 2003), solar flares (Clauset *et al.*, 2009), landslides, and, lastly, rockfalls, are all examples of such events. These phenomena often also display scale-invariance (Hergarten, 2003), meaning the same power-law relationship between event size and frequency holds true across a large range of scales, both in event magnitude and in time.

A power-law distributed size-frequency relationship explains that the frequency of events, *f(V)*, is dependent on the power of the size of the event, *V.* Typically, the smaller the event, the more frequently it will occur, and the larger the event, the less frequently it will occur. β and α are constants.

$$f(V) = \beta V^{-\alpha}$$

The relationship is visualized as linear on a double-logarithmic plot, with a y-intercept of β (at $V = 1$) and slope of -α. Alpha (α) is often referred to as the *scaling parameter* because it represents the relative frequency of events of different sizes occurring. Beta (β) is often referred to as the *activity parameter* because it describes the frequency of events of a magnitude of 1. Below is an example of several power-law distributed events in nature and society, including the distribution of city populations, of unread emails, of forest fire size, of solar flare intensity, of earthquake magnitude, of religion followers, of American surnames, of American wealth distribution, of academic paper citations, of academic paper authors, of website hits, and of website hits (Clauset *et al*., 2009).

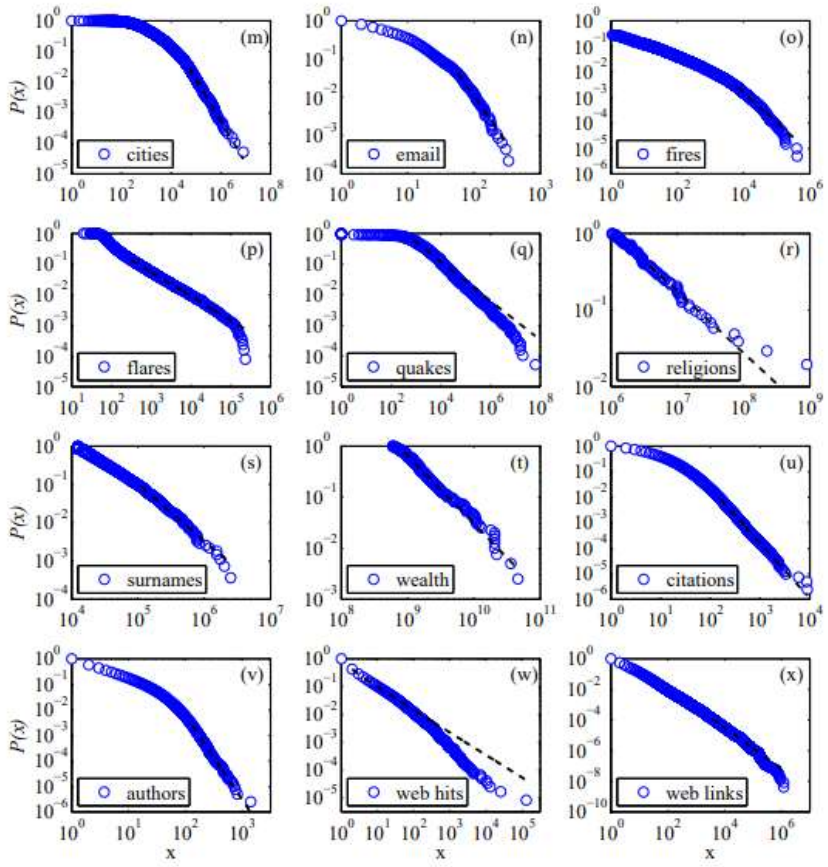

Figure 40. Various power law relationships in nature and society (Clauset et al., 2009)

2.1.1 Methods to Determine the Power Law Parameters

Size-frequency power law parameters can be challenging to estimate accurately. A variety of methods can be used to attempt to accomplish this task. Perhaps the most straightforward and intuitive is the use of arithmetic size bins. The magnitude domain is discretized into equal-width bins, and the events falling within each magnitude bin are counted. The selected bin width is typically arbitrary with respect to the estimate of the scaling parameter α, but will affect the calculation of the activity parameter β. The bin counts can be plotted on a double-logarithmic plot, a linear trendline assigned, and β and α parameters estimated. It is, however, difficult to capture power-law trends over many

orders of magnitude with this method. Since bins stay at constant width, it is difficult to accurately estimate power-law parameters in both the low-magnitude and high-magnitude regions, using the same bin width across the domain. Bins of small width capture parameters in the low-magnitude range well, but many bins in the high-magnitude range will be empty, rendering the data useless, or the bins will have low counts, rendering the data inaccurate. This is especially true if the data set is relatively small. Below is an example of a linearly-binned power-law relationship from LL71, between years 2014-2015. This plot captures approximately 1,000 rockfall events. Notice that neither the lower nor the upper size ranges are captured well with this method.

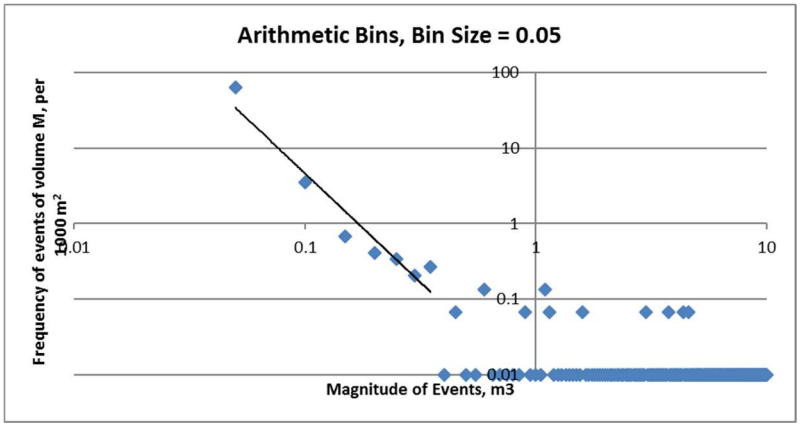

Figure 41. Linearly-binned estimate of power law parameters (LL71, 2014-2015)

Data can also be binned logarithmically. Bins of constant logarithmic width are created, and events falling within each bin are counted. Counts in the high-magnitude region can then properly influence the power-law parameter estimation, due to a larger bin size. However, the varying bin sizes cause the α exponent to be approximated imperfectly. This method will actually measure $\alpha - 1$, and will not provide the proper intercept, β. To correct this problem, each bin count can be normalized by its width, creating a count density (events / size). Below is an example of a normalized logarithmically-binned estimate of power law parameters, again from Long Lake 71, between years 2014-2015.

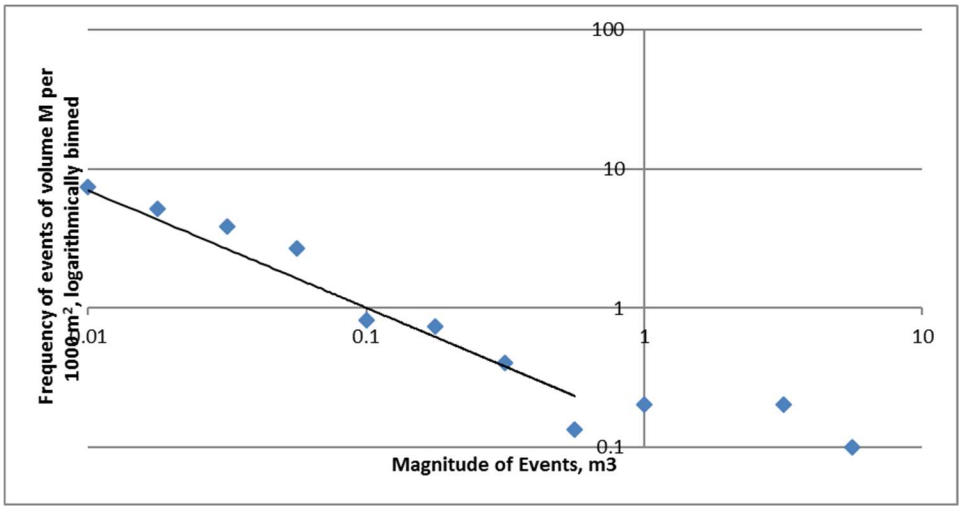

Figure 42. Normalized logarithmically-binned estimate of power law parameters (LL71, 2014-2015)

A probability density function (PDF) can be derived from a frequency density distribution by dividing each bin count by the total number of events. The PDF comments on the relative probability of events occurring in various size ranges, and does not comment on the frequency of events in general. Note that the integral of the PDF across the domain should be equal to 1. A PDF is typically notated as *p(x)*, and we will notate the Probability Density Function as such:

$$p(x) = Cx^{-\alpha}$$

Note that the scaling parameter (α) for the size-frequency distribution and the probability density function will be the same, but the intercept parameters, C and β, will differ.

The Maximum Likelihood Estimation (MLE) method bypasses the need to bin or visualize the data, and estimates the power law exponent (α) directly. It does not estimate β, as the method is based on a derivation from the PDF. Since we've established that the function *p(x)* is a probability density function (PDF), the following must be true:

$$\int p(x)dx = \int Cx^{-\alpha}dx = 1$$

and therefore

$$C = (\alpha - 1) / x_{min}^{1-\alpha}$$

The probability that our values were derived from this distribution is also called the likelihood of the set:

$$P(x|\alpha) = \Pi p(x_i) = \Pi[(\alpha - 1) / x_{min}^{1-\alpha}] * x^{-\alpha}$$

Though we want to know the opposite: a probable value of α given the data x_i. Bayes' Law states:

$$P(\alpha|x) = P(x|\alpha) * P(\alpha) / P(x)$$

Since P(α) and P(x) are constants for our data set

$$P(\alpha|x) \propto P(x|\alpha)$$

It is convenient to take the natural logarithm of both sides of the equation:

$$\ln[P(\alpha|x)] \propto \sum[\ln(\alpha - 1) - \ln(x_{min}) - \alpha \ln(x_i / x_{min})]$$

We can maximize this likelihood function by setting $d(\ln[P(\alpha|x)]) / d\alpha = 0$, and rearrange, to obtain:

$$\alpha = 1 + n[\sum \ln(x_i / x_{min})]^{-1}$$

Plugging the data from the set into this summation provides absolutely the best estimate of the power law exponent, α, that we can obtain. The MLE method also has some drawbacks, however. This method does not estimate the size-frequency activity parameter, β, since it is derived using the PDF constant C. The method also distributes the weighting for the estimation of the parameter α linearly by the number of data points, instead of geometrically on the log scale. Therefore, α is based much more heavily on the head of the distribution, where data is numerous but perhaps less representative of size-frequency power law trends, due to roll-off non-linearity (see Section 2.1.2). Instead, we prefer the estimation of α to be weighted heavily on linear data in the middle of the set, between the head and tail roll-offs.

The last, and most promising method for estimating power law parameters is using a cumulative size-frequency distribution. The cumulative size-frequency distribution describes the frequency of events occurring that are larger than some value V. The cumulative size-frequency distribution is also

intuitive to construct. Discretizing the domain into bins is unnecessary. To create the distribution, one must only decide on some size thresholds at which to produce a data point. These size thresholds are fairly arbitrary, and should not significantly influence the estimated parameters, but can affect the readability of the plot, and the ability to fit a power-law regression. Finer size thresholds will produce a more filled-in curve where the data is readily available. At large size ranges, though, fine thresholds lead to data points with varying x-values (size) and the same y-values (frequency of exceedance), creating a step-like function. One is free to vary the size threshold throughout the domain as he sees fit. For the purpose of this thesis, the cumulative frequency of events larger than the volume V will be calculated at the volume of each event. The cumulative size-frequency distribution will be notated as such:

$$F(V) = BV^{-A}$$

The cumulative size-frequency distribution method has a significant drawback, however. This method somewhat separates the visualization from reality. A histogram, linearly or logarithmically binned, tells us exactly the number of events occurring of a certain size range. We can relate that directly to hillslope processes, to derive erosion flux, for hazard mapping, or for other purposes. The cumulative size-frequency distribution cannot as readily be related to reality. Below is a plot of the cumulative size-frequency distribution for Long Lake Site 71, from 2014-2015. The linearity and prevalence of the data points should be noted.

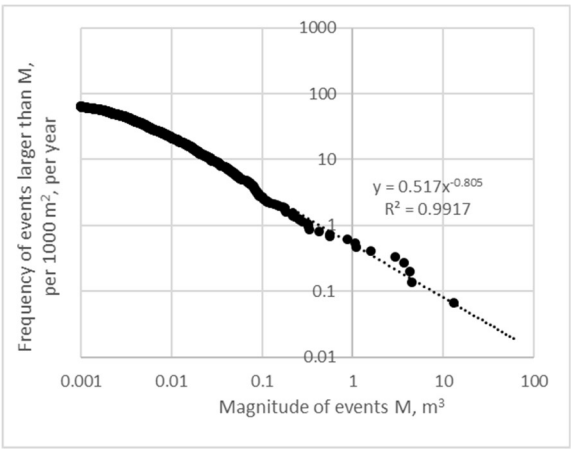

Figure 43. Cumulative size-frequency distribution for LL71, 2014-2015

The cumulative size-frequency distribution, *F(V),* can be related to the non-cumulative size-frequency distribution, *f(V)*. *F(V)* is merely a running summation of *f(V)*. So:

$$F(V) = \int f(V)dV$$

and

$$f(V) = - dF(V) / dV$$

therefore

$$\beta = B * A$$

$$\alpha = A + 1$$

This thesis will be utilizing this relationship often. Since accurate size-frequency parameters can most easily be obtained using the cumulative size-frequency distribution, this method will be used to obtain slope and intercept parameters for the distribution. The β and α parameters can then be calculated, to be used to relate data back to reality.

As with the size-frequency distribution, the cumulative size-frequency distribution can be divided by the total number of events to derive a cumulative density function (CDF). The CDF *P(x)* and the PDF *p(x)* and their constants are related in the same manner as *F(V)* and *f(V)*.

2.1.2 The Power Law Roll-Off

Power law parameters will only be valid for certain size ranges within our data set. Events of small volume are difficult to detect using the change methods outlined in Section 1.6. Small events will be undersampled, and, therefore, the log-log cumulative and non-cumulative plots will be non-linear below a minimum magnitude threshold, V_{min}. Although methods exist to quantify V_{min} statistically, this paper will quantify V_{min} graphically, observing it as the point where log-log linearity ends at the low-magnitude, high-frequency end of the magnitude-frequency curve.

Large volume events may also deviate from power-law behavior for a specific slope. Two effects primarily drive this deviation. Firstly, rock-slopes have a finite availability of material and kinematic ability to produce large failures. This is analogous to the upper bounds placed on the Gutenberg-Richter Recurrence Laws in seismology. In seismology, the Earth has not been shown capable of producing an earthquake of Magnitude 10 or larger. If it had, we would expect the Circumpacific belt to produce a Magnitude 10 earthquake only every 50 years (Kramer, 1996), though we've got no evidence of one ever occurring. Similarly, since rock-slopes are finite in height and width, failures above a certain size range would not be possible at some rock-slopes.

Secondly, large events may be temporally censored, as observed in several other databases (Hantz, 2011). Our database does not cover a large enough temporal range to experience the excessively large events that may still be represented by the power-law model. If an event is expected to happen once every ten years, and it does not happen during our five years of data collection, it's frequency will be undersampled by the data set, and the estimated power-law parameters may therefore be skewed at the tail of the distribution.

Because of these two effects, it is necessary to assign an upper bound magnitude to the power-law model, notated V_{max}, if non-linearity at large magnitudes are observed.

2.1.3 Volume Flux Derivation from Size-Frequency Distributions

After estimating the size-frequency power law parameters, β and α, an average annual volumetric erosion flux can be calculated for each RAI Class. Firstly, since the frequency distribution function only demonstrates the likelihood of events at given volumes, we must multiply the function by the event volumes, to get a volume contribution distribution (Barlow *et al.*, 2012). This distribution explains the Volume Loss contributed by events of particular sizes.

$$\textit{Volume Contribution Distribution} = \beta V^{-\alpha} * V = \beta V^{1-\alpha}$$

We can then sum the volume contributions of each event size over the domain, to derive an estimate for average annual volumetric erosion flux:

$$V_{tot} = \int \beta V^{1-\alpha}\, dV = \beta V_{max}^{2-\alpha} / (2-\alpha) - \beta V_{min}^{2-\alpha} / (2-\alpha)$$

2.1.4 Distribution of Volume Contributions of Failure Events at Long Lake

In order to investigate the upper-bound to the power law, one can also directly observe the distribution of volume contribution to total volume flux. Table 9 and Figure 44**,** below, outline the observed contributions of failure size bins to volume flux at each of the investigated sites. Because failures smaller than 0.001 m^3 were ignored at some sites, and below 0.0001 m^3 at others, data for the two smallest size bins is intermittently available.

Size / Site	.00001-.0001	.0001-.001	.001-.01	.01-.1	0.1-1	1-10	10-100
2012-2013							
LL85.5	N/A	N/A	0.0047	0.10	0.50	0	0
LL86.9	N/A	0.00058	0.028	0.97	2.39	0	0
LL87	N/A	N/A	0.0038	0.18	0.71	1.05	0
2013-2014							
LL85.5	0.00014	0.0013	0.035	0.17	0.28	0	0
LL86.9	N/A	N/A	0.44	5.52	3.17	2	0
LL87	0.00033	0.015	0.21	0.95	1.76	0	0
LL71	N/A	N/A	2.94	7.57	11.58	49.46	28.07
2014-2015							
LL85.5	0.00001	0.00071	0.037	0.16	1.01	0	0
LL86.9	N/A	N/A	0.44	1.61	1.85	0	0
LL87	0.00031	0.012	0.35	0.90	0.43	0	0
LL71	0.00062	0.037	2.39	8.56	7.40	19.30	13.03
2015-2017							
LL85.5	0.00008	0.00067	0.029	0.14	0.45	0	0
LL86.9	0.00023	0.021	0.38	2.45	3.90	3.90	0
LL87	0.00028	0.012	0.16	0.67	2.73	0.74	0
LL71	0.00084	0.054	2.35	8.55	11.16	33.84	17.83

Table 9. Volume contributions (in m3) to total volume flux for various size bins, for each study site

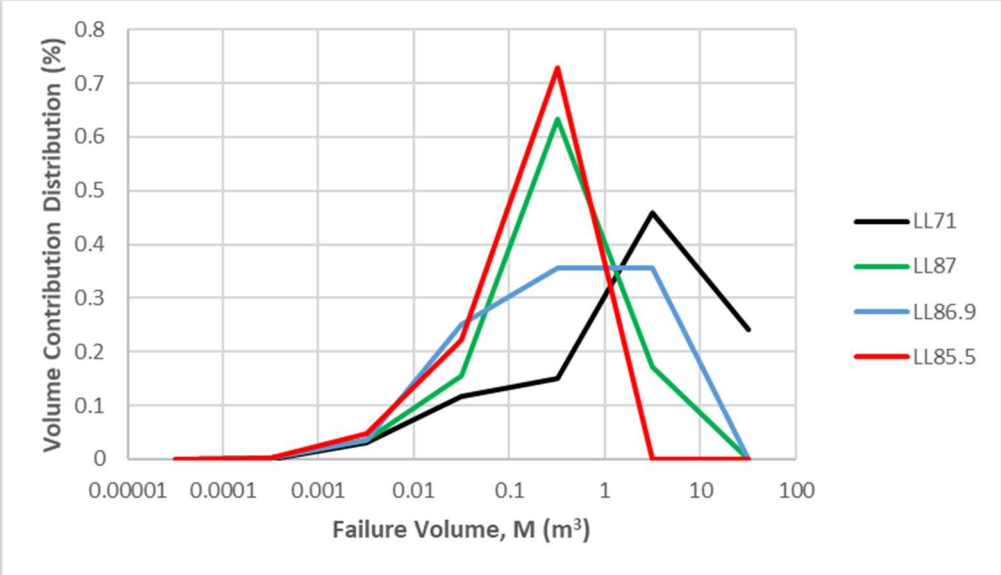

Figure 44. % of volume contributions from each size bin, averaged over all years.

It can be noted that the smallest size bins generally contribute insignificantly to the overall volume flux. Therefore, the methodology of assuming a lower bound to the size-frequency distribution is reasonable. Since the scan and model resolution prevent our ability to track failures under 0.001 m^3, relatively little is known about the mass-wasting processes in the small size ranges at the study sites. Some authors have noted that power-law size-frequency distributions hold true for very small size ranges (Barlow *et al.*, 2012). However, since we have not observed these events, and they are insignificant in the volume flux and hazard mapping methodologies, events below 0.001 m^3 have been omitted from any forward projection volume flux calculations.

Additionally, it is notable that the largest size bins contribute greatest, until some upper-bound is approached. It is, therefore, again proven necessary to instigate an upper bound on the volume flux model. The plot shows that the upper bound on power-law behavior changes depending on the site. Larger and more active sites (LL71 and LL86.9) incur larger volume contributions from the upper size ranges, whereas the smaller and less active sites incur larger volume contributions from the mid-range and lower size ranges.

It can also be noted that sites with a higher scaling parameter, α, have a greater volume flux contribution by small failures, as can be expected. For example, site LL86.9 in 2014-2015 has the highest scaling parameter ($\alpha = 1.914$) and has a relatively large contribution of small failures (53% of volume flux coming from failures below 0.1 m^3). When the scaling parameter α approaches 2, the volume contribution calculated for each bin will be approximately equal (see volume flux derivation in Section 2.1.3).

2.2 Size-Frequency Distributions for Rock-Slope Failures

Figures 45 to 59 show overall change cumulative size-frequency distributions for each site, with least-square power-law regressions. Table 10. Size-frequency parameters and volume flux

measurements for the four key Long Lake sites. gives the size-frequency parameters, the measured erosional volume flux from the slope (overall and loss per 1000 m^2), and the average slope recession rate.

2.2.1 2012-2013

During the 2012 mobile LiDAR surveys, the scan resolution was too low to capture failures accurately below approximately 0.01 m^3. This can be observed in Figures 45 through 47, below, where the low-end roll-off occurs at a much larger volume than during other change epochs.

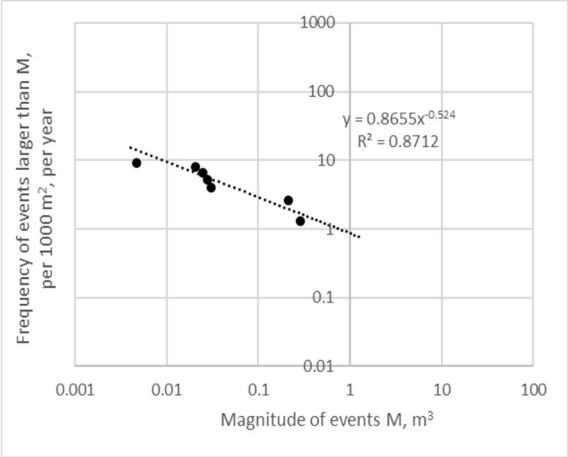

Figure 45. Cumulative size-frequency distribution for LL85.5.

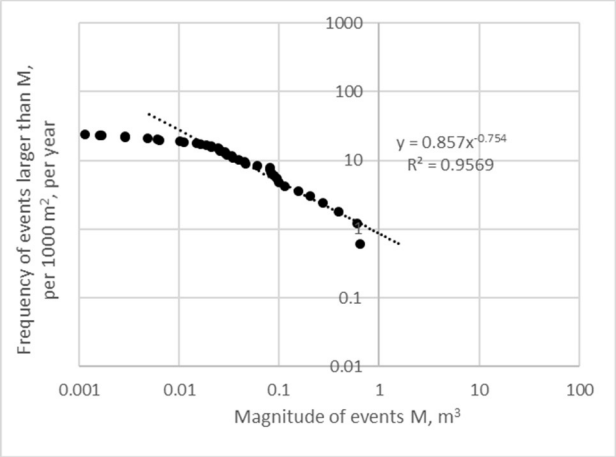

Figure 46. Cumulative size-frequency distribution for LL86.9.

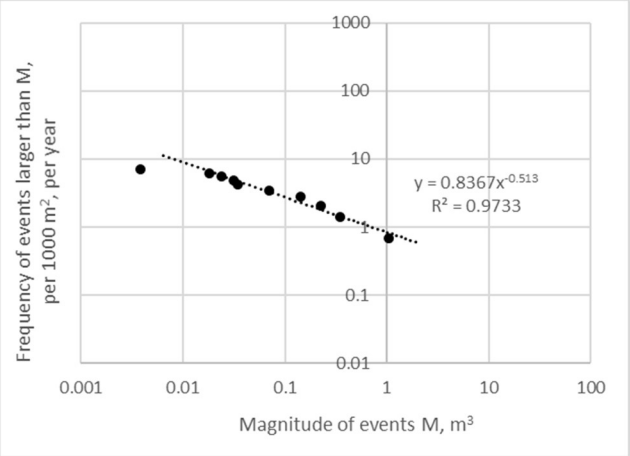

Figure 47. Cumulative Size-Frequency Curve for LL87

2.2.2 2013-2014

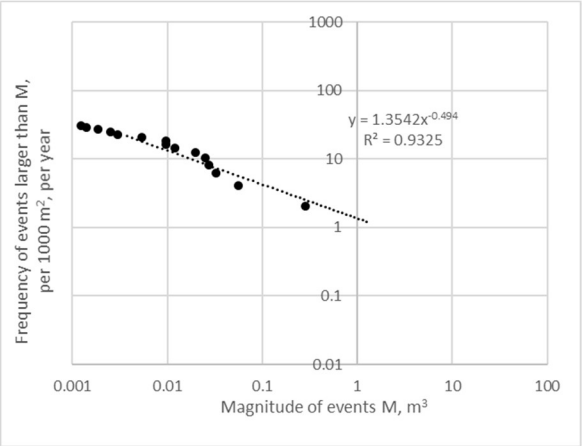

Figure 48. Cumulative Size-Frequency Curve for LL85.5.

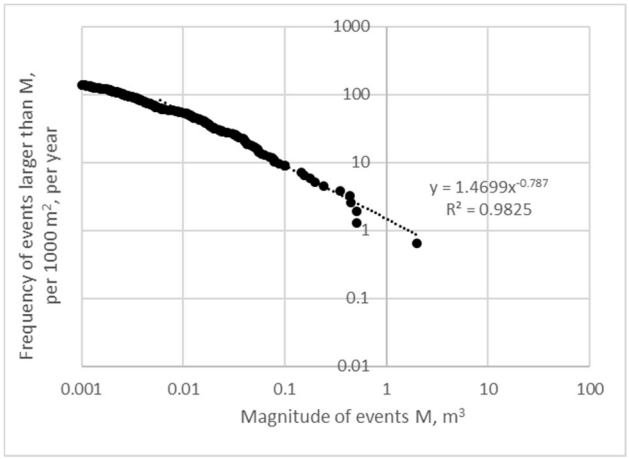

Figure 49. Cumulative Size-Frequency Curve for LL86.9.

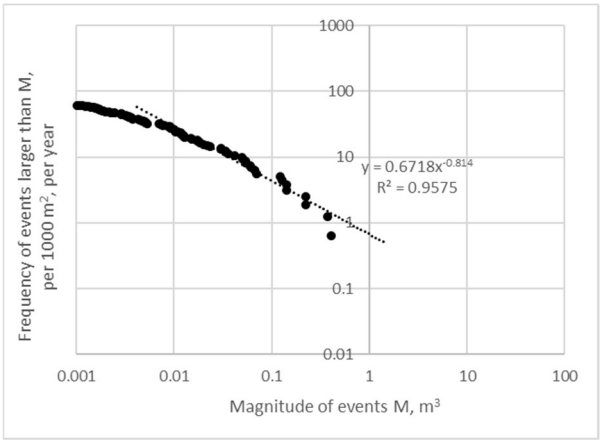

Figure 50. Cumulative Size-Frequency Curve for LL87.

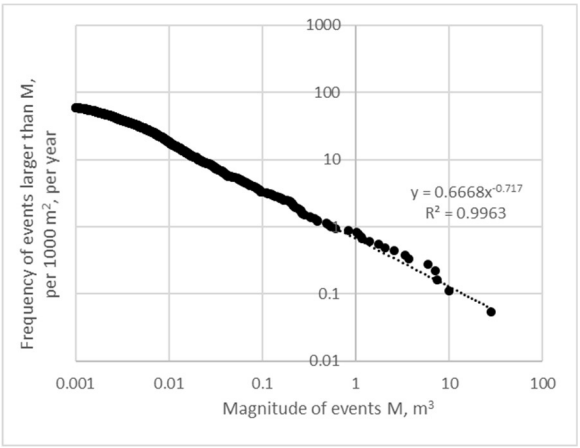

Figure 51. Cumulative Size-Frequency Curve for LL71.

2.2.3 2014-2015

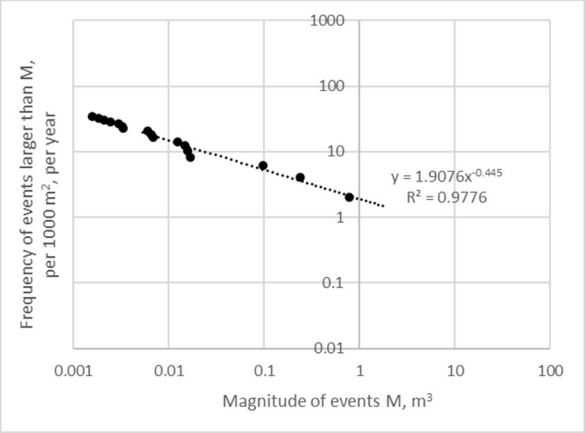

Figure 52. Cumulative Size-Frequency Curve for LL85.5

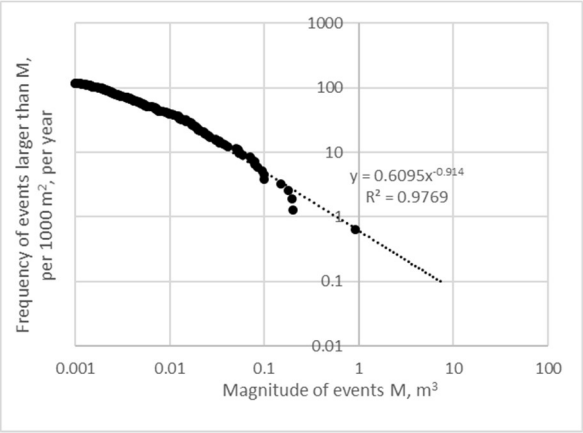

Figure 53. Cumulative Size-Frequency Curve for LL86.9

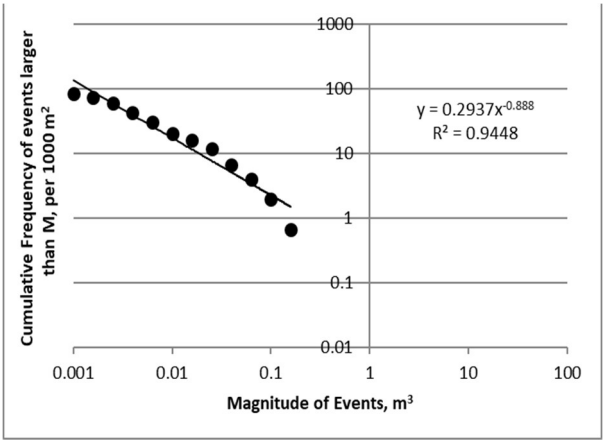

Figure 54. Cumulative Size-Frequency Curve for LL87.

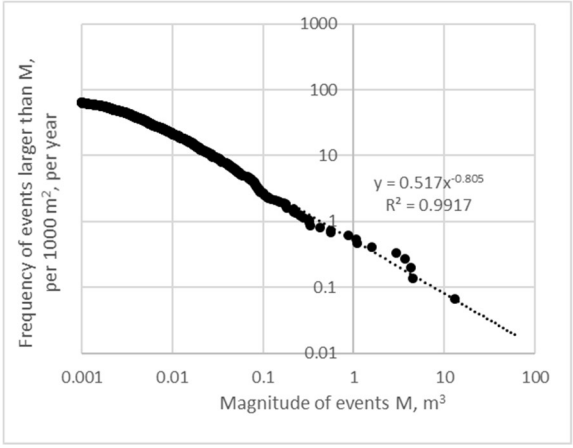

Figure 55. Cumulative Size-Frequency Curve for LL71.

2.2.4 2015-2017

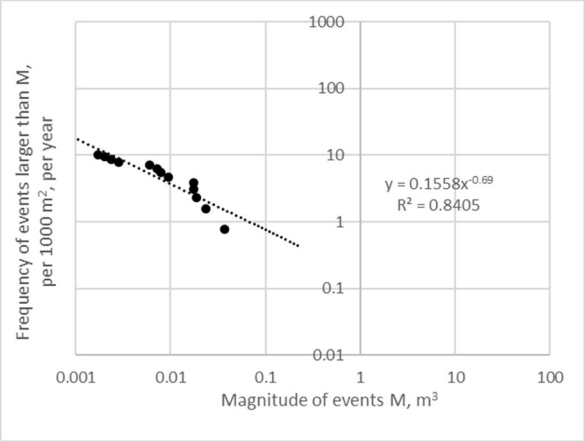

Figure 56. Cumulative Size-Frequency Curve for LL85.5.

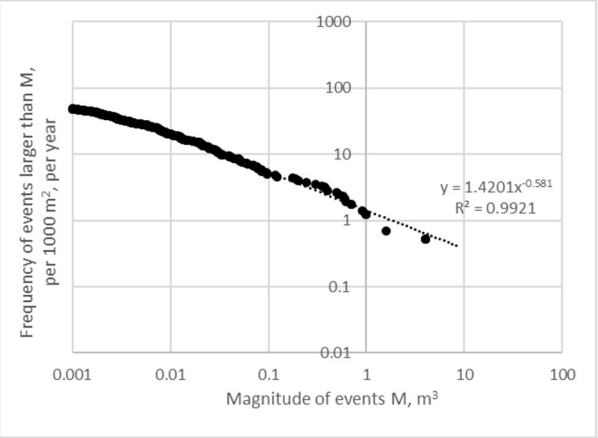

Figure 57. Cumulative Size-Frequency Curve for LL86.9.

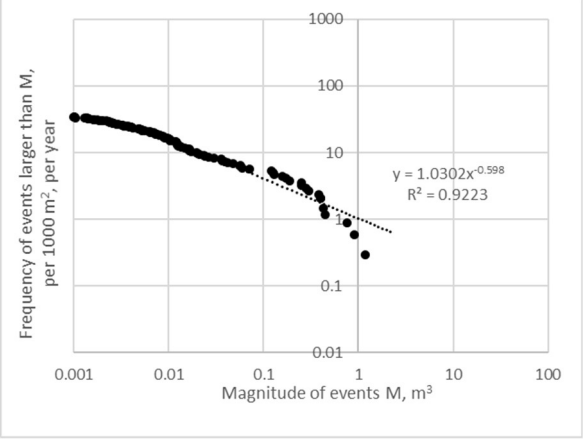

Figure 58. Cumulative Size-Frequency Curve for LL87.

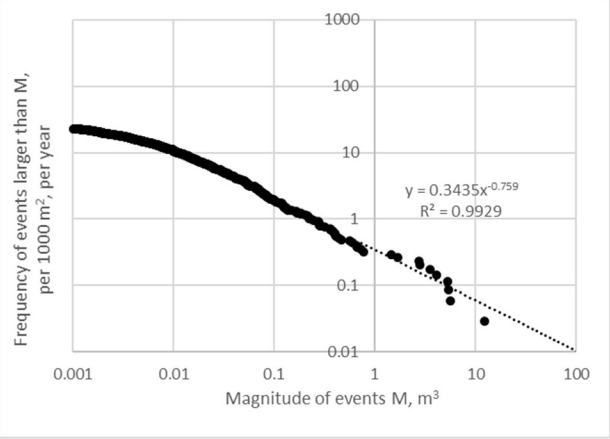

Figure 59. Cumulative Size-Frequency Curve for LL71.

Site	Activity, β	Scaling, α	Observed Volume Flux per 1000m^2 (m^3/yr)	Total Observed Volume Flux (m^3/yr)	Observed Slope recession rate (m/yr)
2012-2013					
LL85.5	0.454	1.524	0.807	0.610	0.0008
LL86.9	0.646	1.754	2.095	3.486	0.0021
LL87	0.429	1.513	1.348	1.942	0.0014
2013-2014					
LL85.5	0.669	1.494	1.010	0.491	0.0010
LL86.9	1.157	1.787	5.128	7.963	0.0051
LL87	0.547	1.814	1.848	2.947	0.0018
LL71	0.478	1.717	5.467	99.655	0.0055
2014-2015					
LL85.5	0.849	1.445	2.484	1.207	0.0025
LL86.9	0.558	1.914	2.514	3.902	0.0025
LL87	0.261	1.888	1.13	1.69	0.0011
LL71	0.416	1.805	3.450	50.957	0.0035
2015-2017					
LL85.5	0.095	1.610	0.121	0.077	0.0001
LL86.9	0.825	1.581	3.231	9.179	0.0032
LL87	0.616	1.598	2.360	4.012	0.0024
LL71	0.261	1.759	2.064	35.647	0.0021

Table 10. Size-frequency parameters and volume flux measurements for the four key Long Lake sites.

2.3 Temporal Variation in Size-Frequency Distributions

Figures 60 through 63, below, show the variation of size-frequency curves between years.

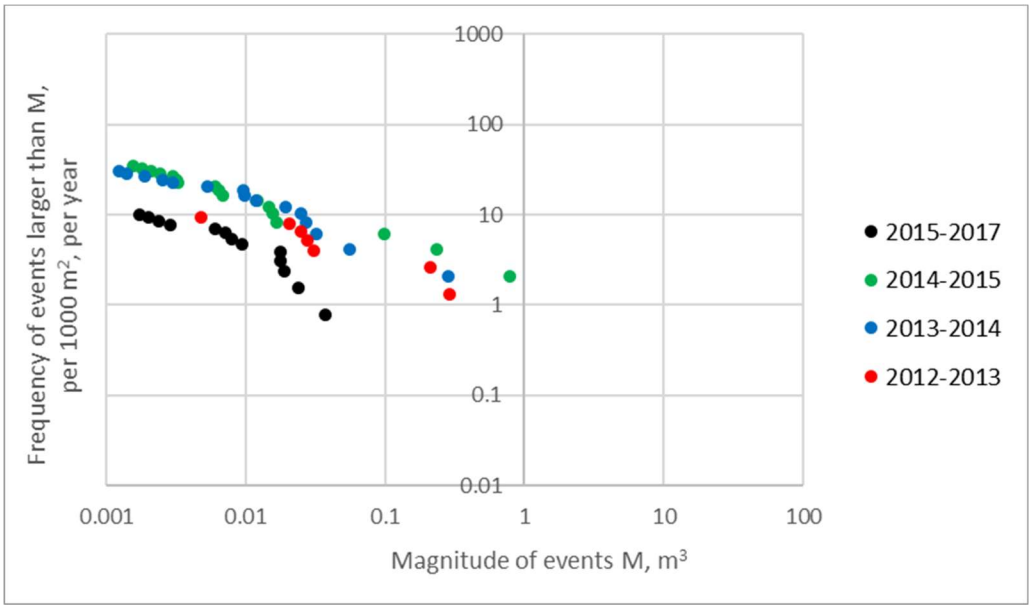

Figure 60. Year-to-Year overall change curves at LL85.5

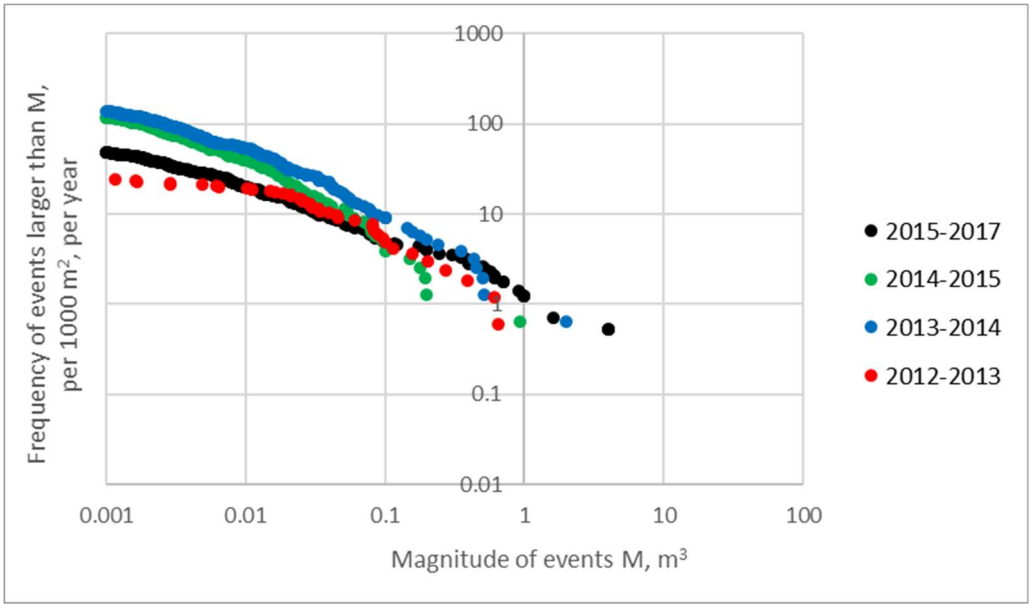

Figure 61. Year-to-Year overall change curves at LL86.9

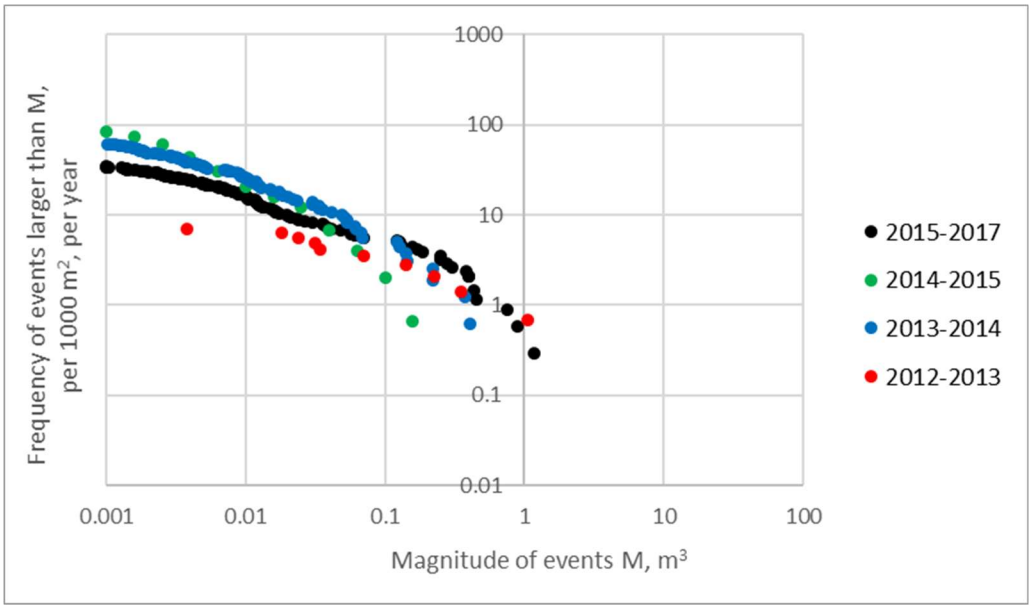

Figure 62. Year-to-Year overall change curves at site LL87

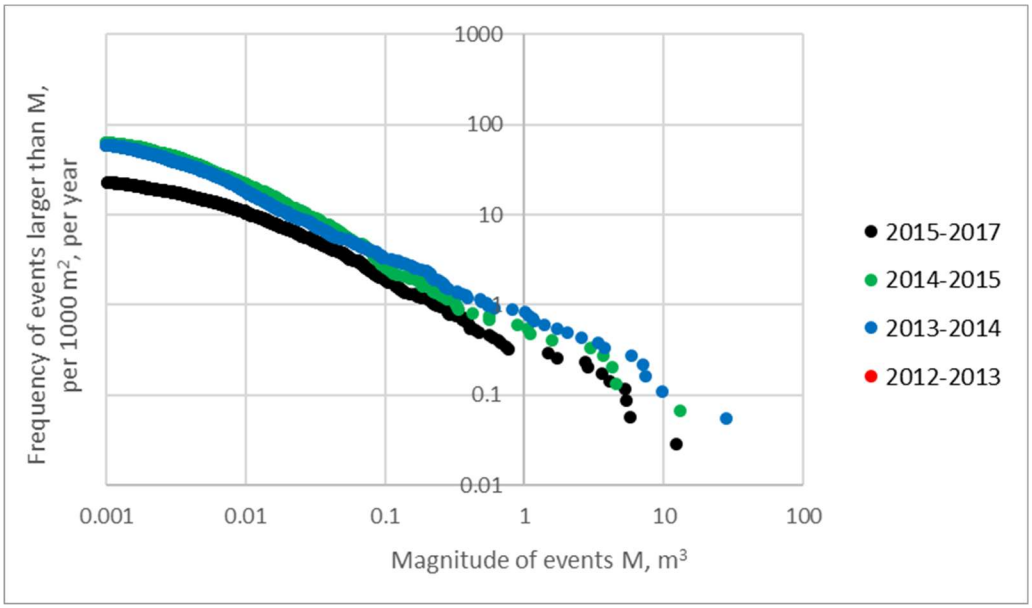

Figure 63. Year-to-Year overall change curves at site LL71

Table 11 provides size-frequency parameters and recession rate measurements for each change epoch, averaged over the four sites. Figures 64 through 66 show the mean and standard deviation of these parameters.

Change Epoch	Average Activity, β	σ of β	CoV of β	Average Scaling, α	σ of α	CoV of α	Average Slope Recession Rate (m/yr)	σ of Slope Recession Rate	CoV of Slope Recession Rate
2012-2013	0.510	0.097	0.190	1.597	0.111	0.070	0.0014	0.0005	0.371
2013-2014	0.713	0.265	0.372	1.703	0.126	0.074	0.0034	0.0020	0.590
2014-2015	0.521	0.216	0.416	1.763	0.188	0.107	0.0021	0.0009	0.356
2015-2017	0.449	0.287	0.639	1.637	0.071	0.043	0.0020	0.0011	0.585

Table 11. Mean and Standard Deviation of size-frequency parameters and recession rate for all sites.

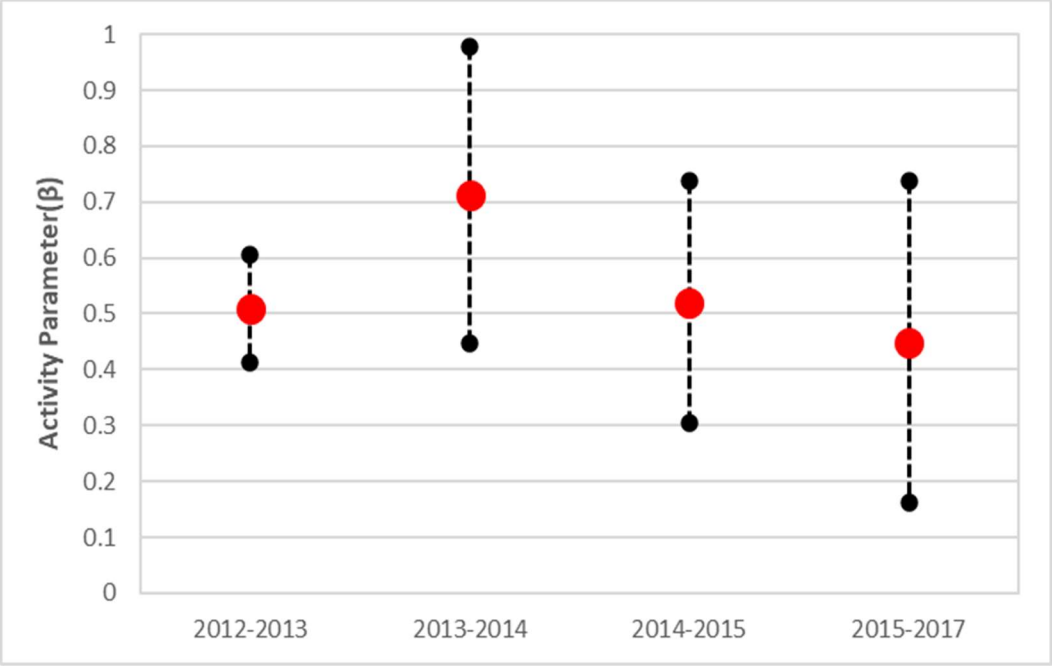

Figure 64. Plots of the mean and standard deviation of the Activity Parameter for each change epoch, across the sites.

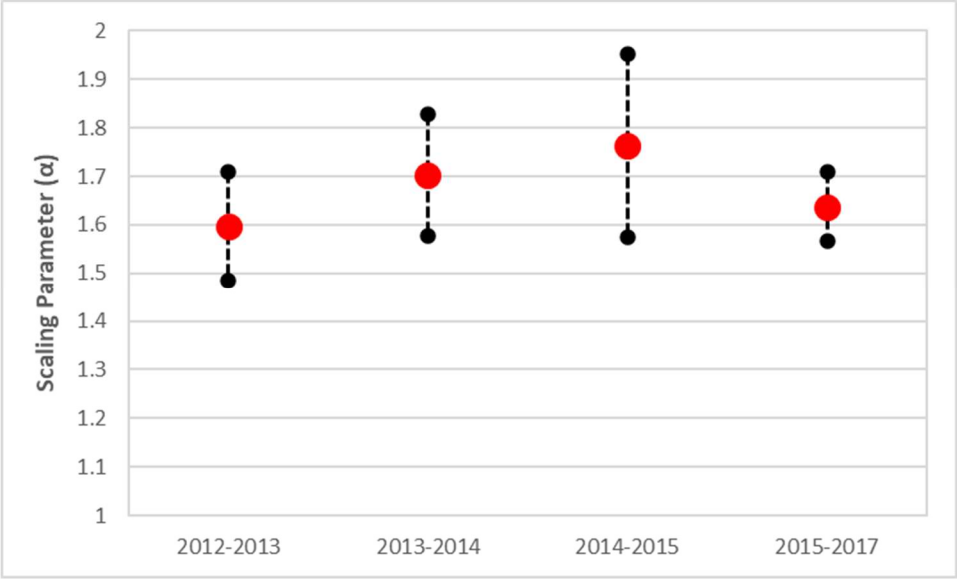

Figure 65. Plots of the mean and standard deviation of the Scaling Parameter for each change epoch, across the sites.

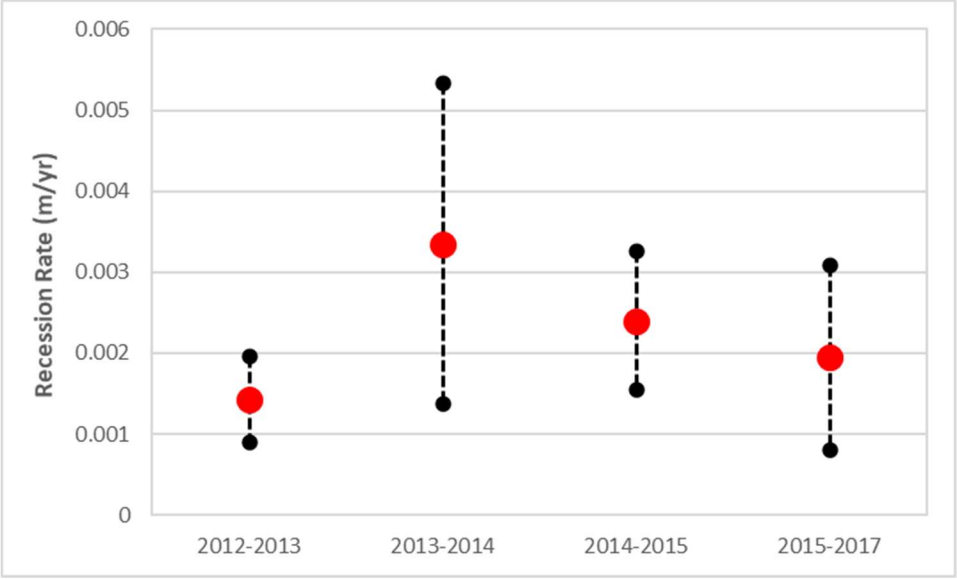

Figure 66. Plots of the mean and standard deviation of the Scaling Parameter for each change epoch, across the sites.

The plots show slight variations in the size-frequency parameters and recession rate values between years, but not substantial difference.

2.4 Spatial Variation of Size-Frequency Distributions

To further understand the degree of variation from year-to-year for each site (outlined above, in 2.3**)**, it is useful to investigate site-to-site variation from each change epoch. Figures 67 through 70, below, show variations between size-frequency curves of distinct sites for each change epoch.

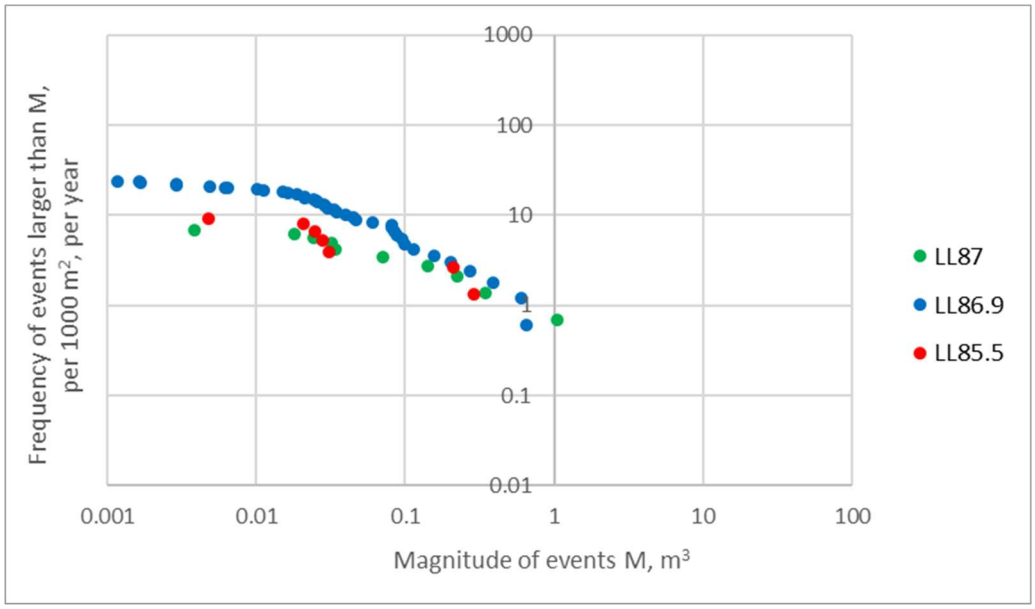

Figure 67. 2012-2013 Site-to-Site Change Curve Comparison

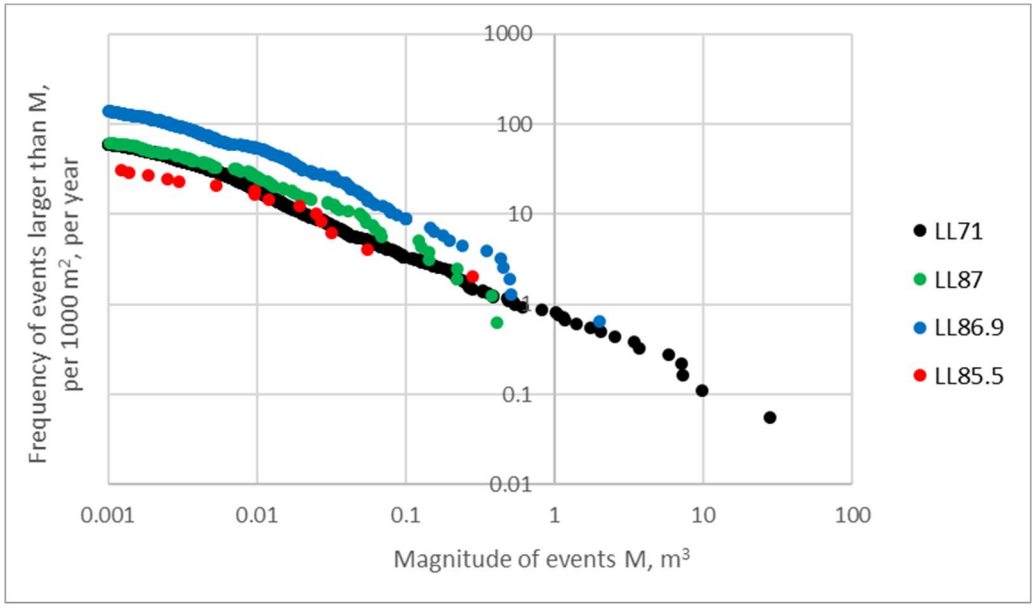

Figure 68. 2013-2014 Site-to-Site Change Curve Comparison

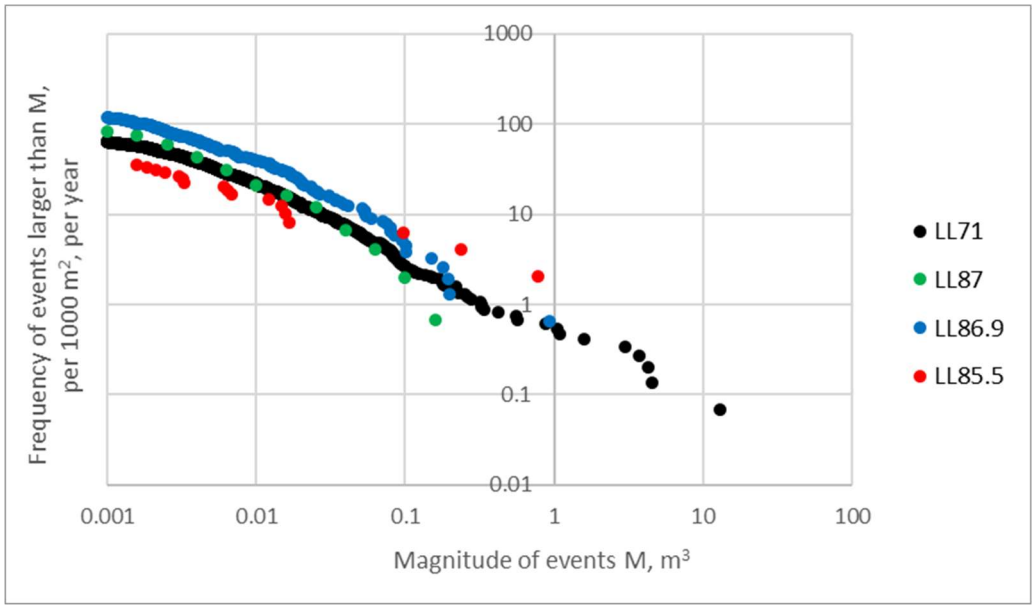

Figure 69. 2014-2015 site-to-site change curve comparison

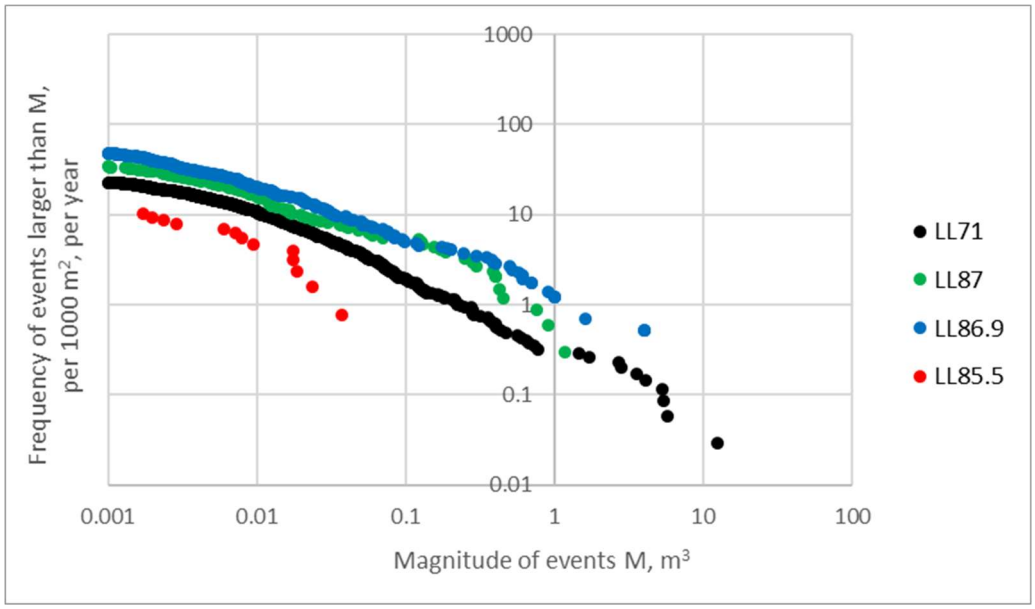

Figure 70. 2015-2017 site-to-site change curve comparison

Table 12 provides size-frequency parameters and recession rate measurements for each site, averaged over the change years. Figures 71 through 73 show plots of the standard deviations and means of these parameters.

Site	Average Activity, β	σ of β	CoV of β	Average Scaling, α	σ of α	CoV of α	Average Slope Recession Rate (m/yr)	σ of Slope Recession Rate	CoV of Slope Recession Rate
LL85.5	0.555	0.281	0.543	1.518	0.060	0.040	0.0014	0.0005	0.795
LL86.9	0.827	0.229	0.288	1.759	0.119	0.068	0.0034	0.0020	0.357
LL87	0.498	0.134	0.290	1.703	0.153	0.090	0.0021	0.0009	0.291
LL71	0.328	0.091	0.270	1.760	0.036	0.036	0.0020	0.0011	0.377

Table 12. Mean and Standard Deviation of size-frequency parameters and recession rate across epochs

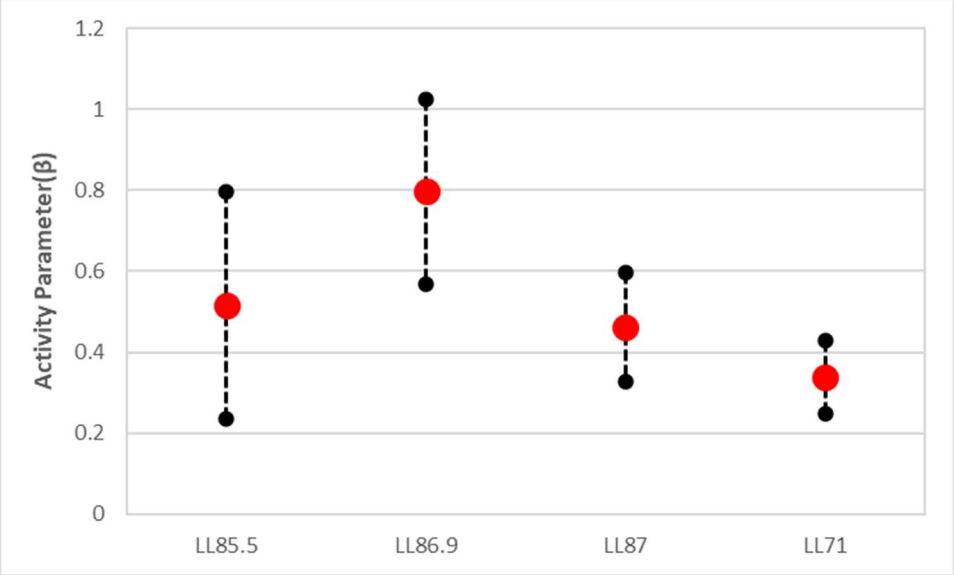

Figure 71. Plots of the mean and standard deviation of the Activity Parameter for each site, across the change epochs.

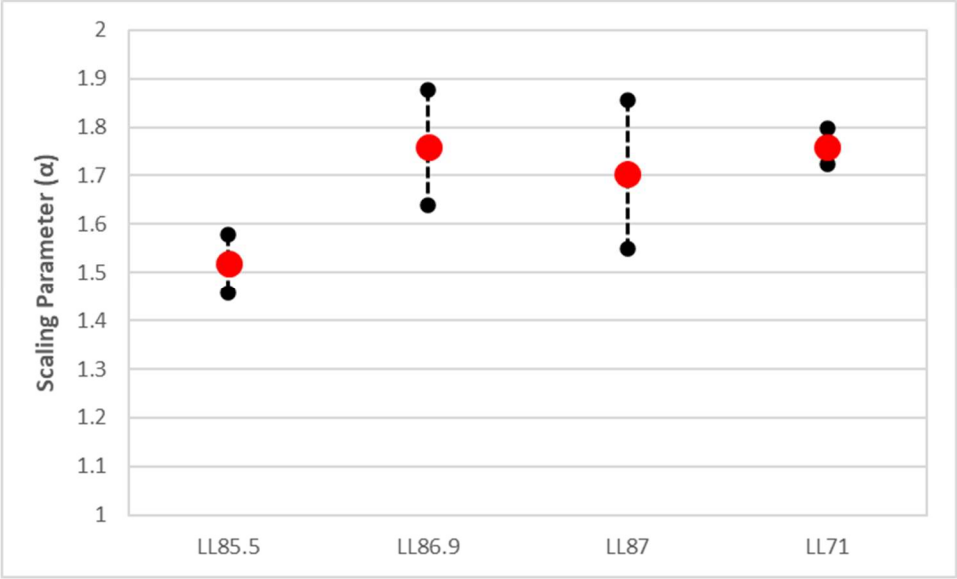

Figure 72. Plots of the mean and standard deviation of the Scaling Parameter for each site, across the change epochs.

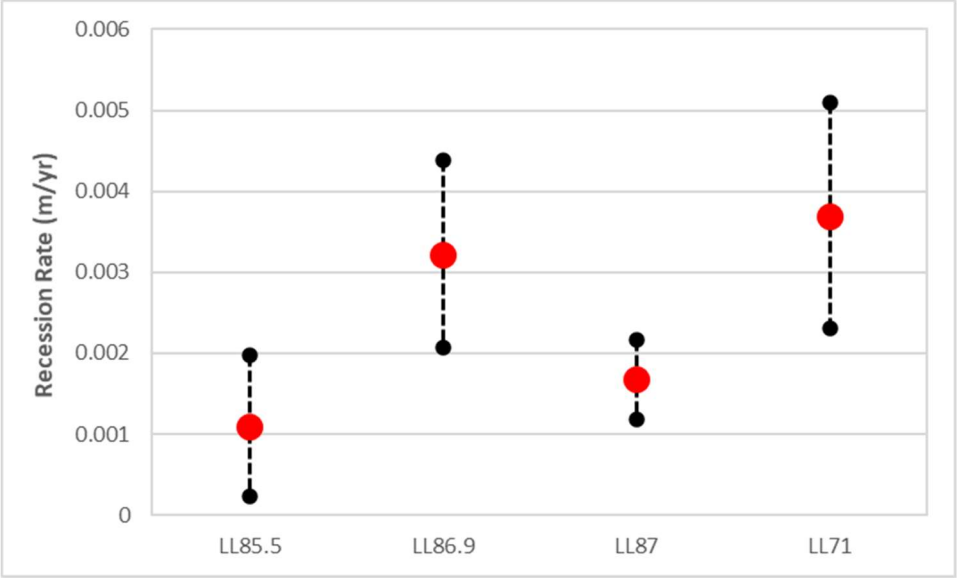

Figure 73. Plots of the mean and standard deviation of the Recession Rate for each site, across the change epochs.

Generally, one can deduce that the parameters and recession rates are not particularly discernible between sites or between change epochs, when the data is all averaged. Figures 74 through 76 track changes in the parameters and recession rate through time for each site.

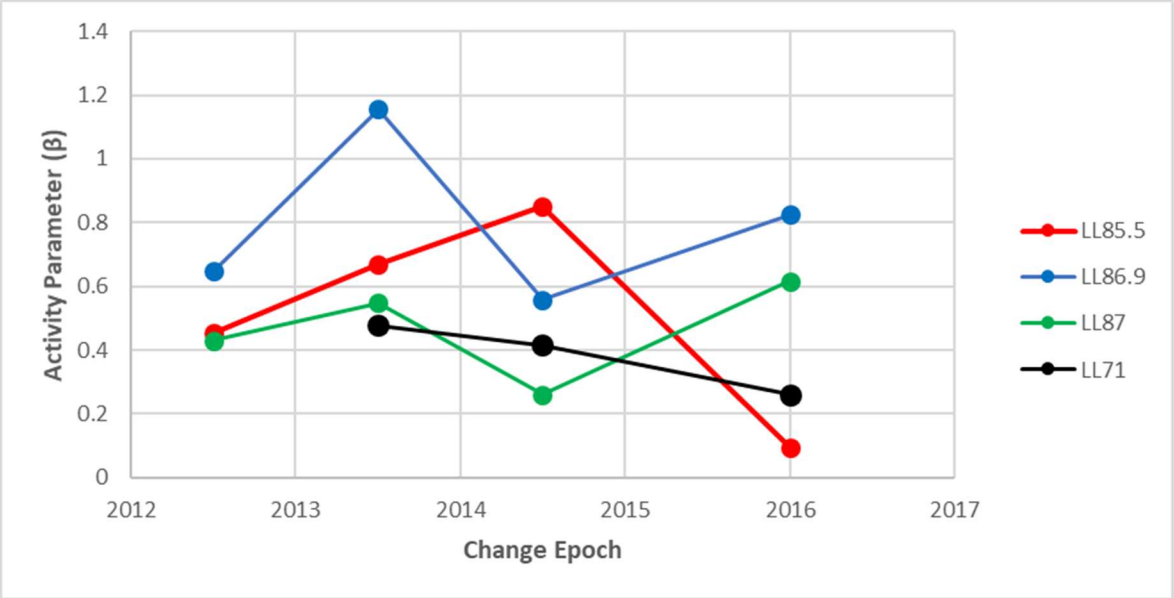

Figure 74. Variations in the activity parameter for the four different sites through time.

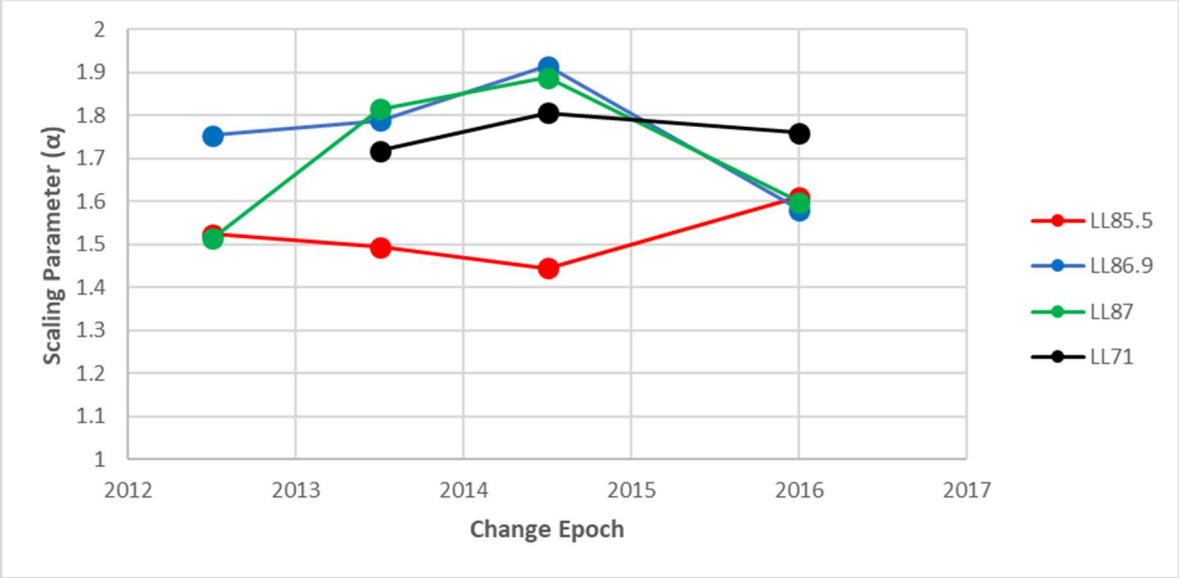

Figure 75. Variations in the scaling parameter for the four different sites through time.

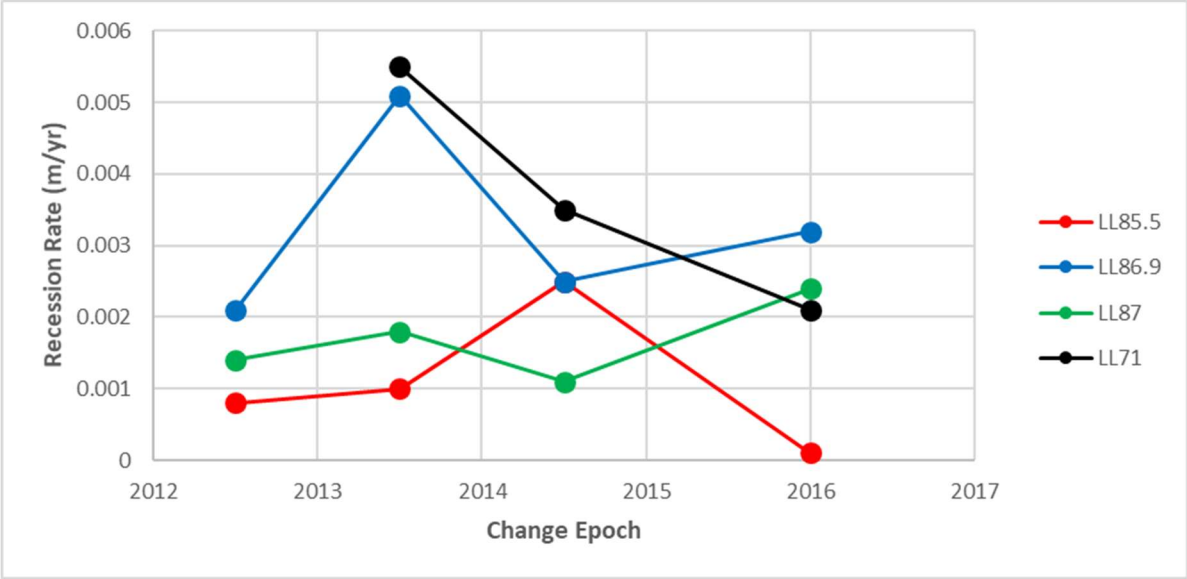

Figure 76. Variations in the recession rate measurement for the four different sites through time.

Two sites with very similar character in terms of RAI Classifications and areal coverage (LL86.9 and LL87) seem to trend with each other in their size-frequency parameters and recession rates through time. Trends between sites that share little in common appear to be non-existent in terms of these parameters. Interestingly, general activity rates have spiked for Talus-dominated sites in the 2015-2017 epoch, whereas activity rates at sites dominated by other RAI Classes and mass-wasting processes seems to have dropped sharply in the same epoch. This phenomenon will be investigated further in the following sections.

2.5 Variation of Size-Frequency Distributions between RAI Classes

The Rockfall Activity Index (RAI) classes explained in Section 1.5 were defined by Dunham *et al*. to attempt to differentiate between areas of the slope with distinct mass wasting processes. Therefore, this paper seeks to analyze differences between size-frequency distribution parameters for different RAI Classes, and investigate whether or not the RAI Classifications properly map the slope by mass-wasting processes. For Long Lake Site 71, the RAI Class magnitude-frequency curves are reported for each

change epoch; for the other sites, because of the small sample size, the magnitude-frequency curves for all years are combined into one plot.

The predominant (by area) RAI Class within an isolated failure was flagged as the class responsible for said failure. Figures 77 through 82 show distinctions between size-frequency curves for RAI Classes at LL71, for the 2013-2014, 2014-2015 and 2015-2017 change epochs.

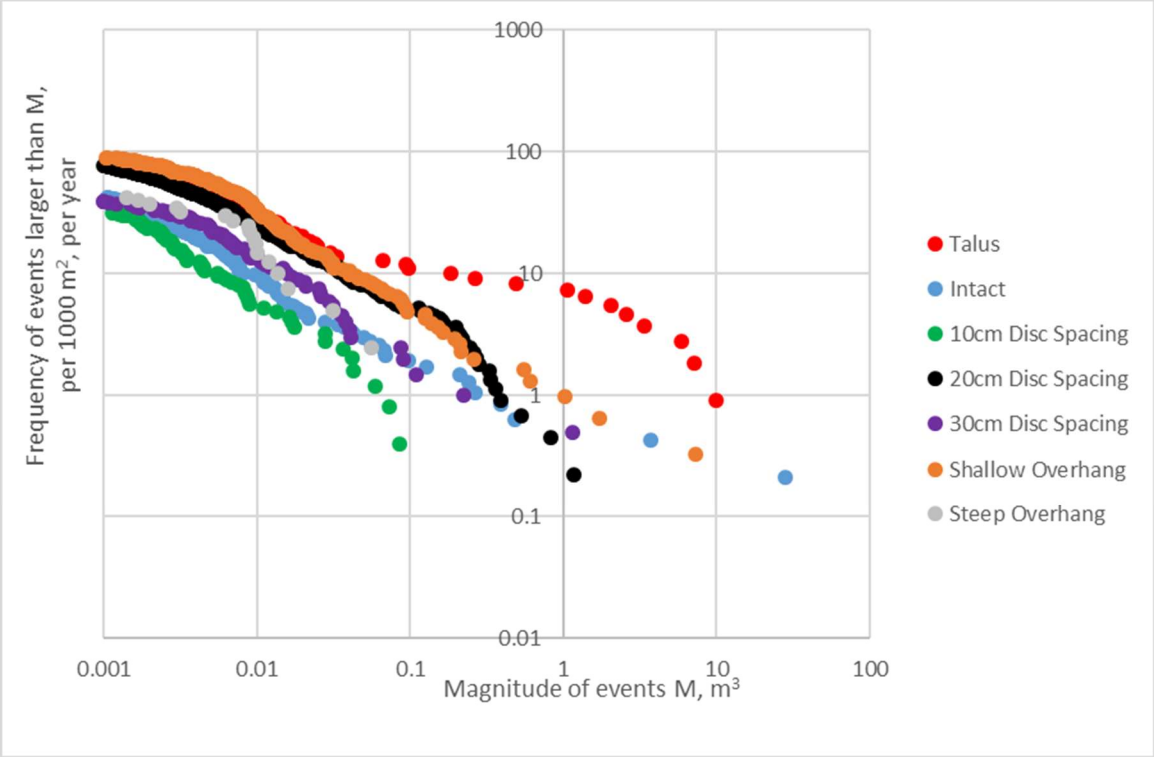

Figure 77. LL71 RAI Class Cumulative Size-Frequency Curve for the 2013-2014 Change Epoch

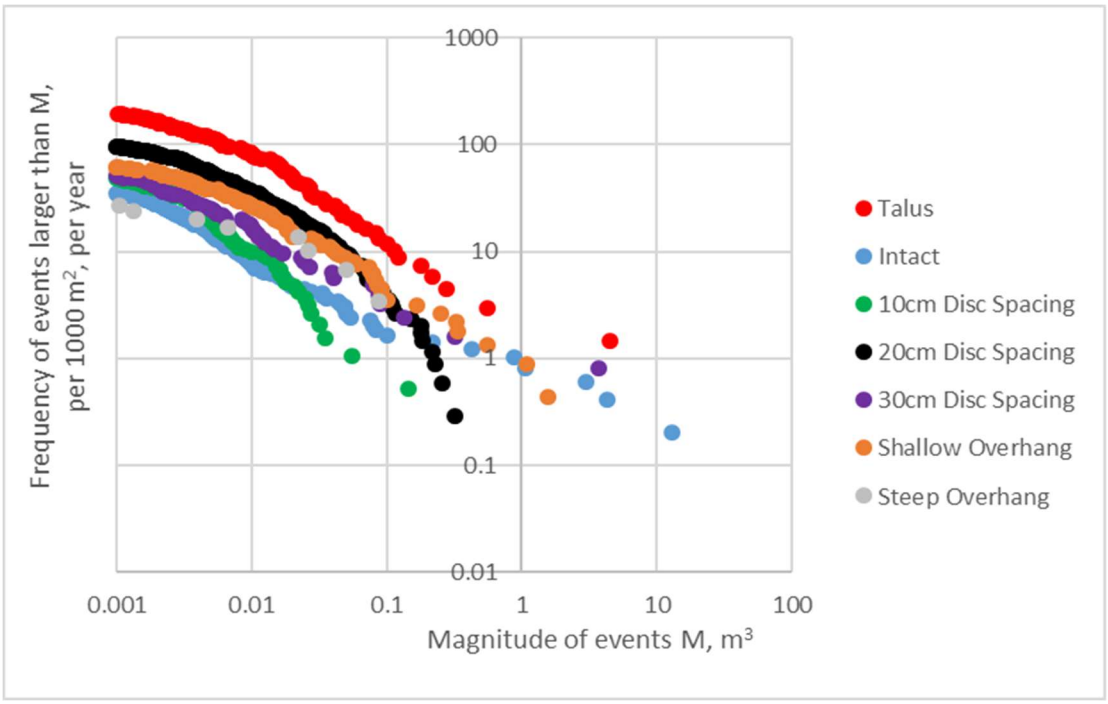

Figure 78. LL71 RAI Class Cumulative Size-Frequency Curve for the 2014-2015 Change Epoch

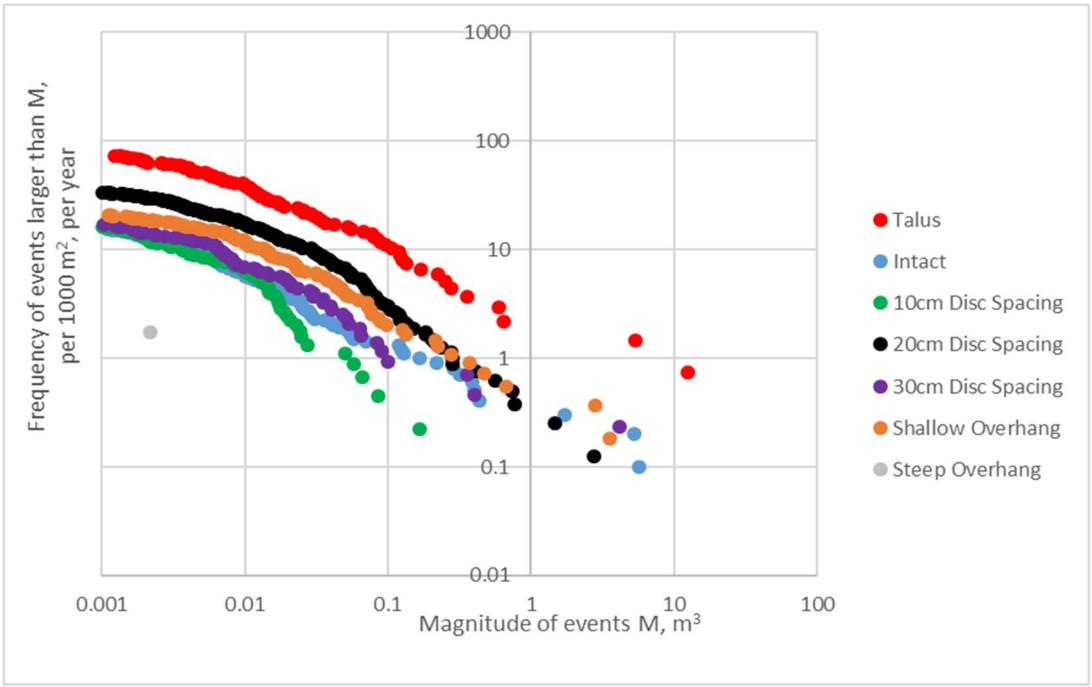

Figure 79. LL71 RAI Class Cumulative Size-Frequency Curve for the 2015-2017 Change Epoch

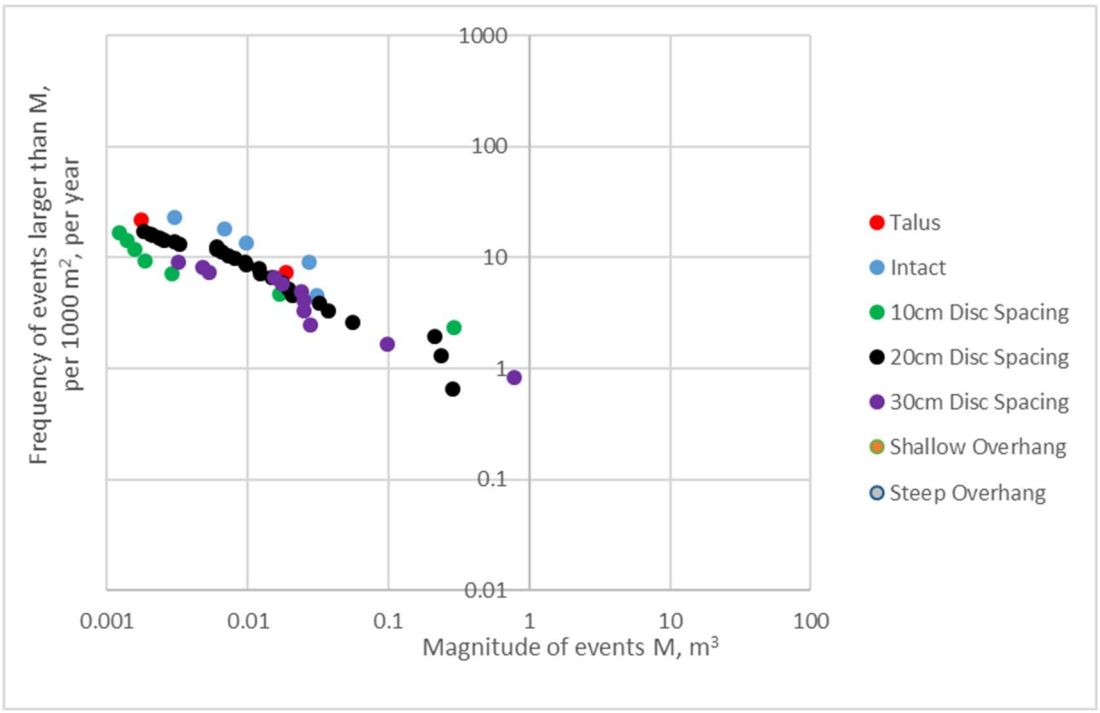

Figure 80. LL85.5 RAI Class Cumulative Size-Frequency Curve for 2012-2017

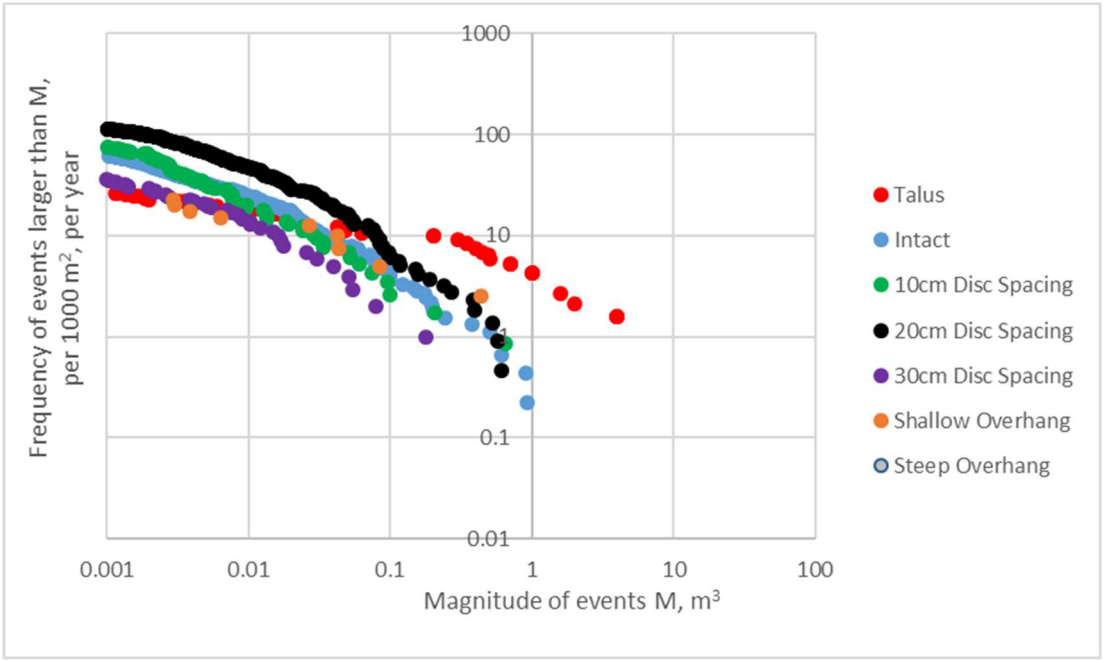

Figure 81. LL86.9 RAI Class Cumulative Size-Frequency Curve for 2012-2017

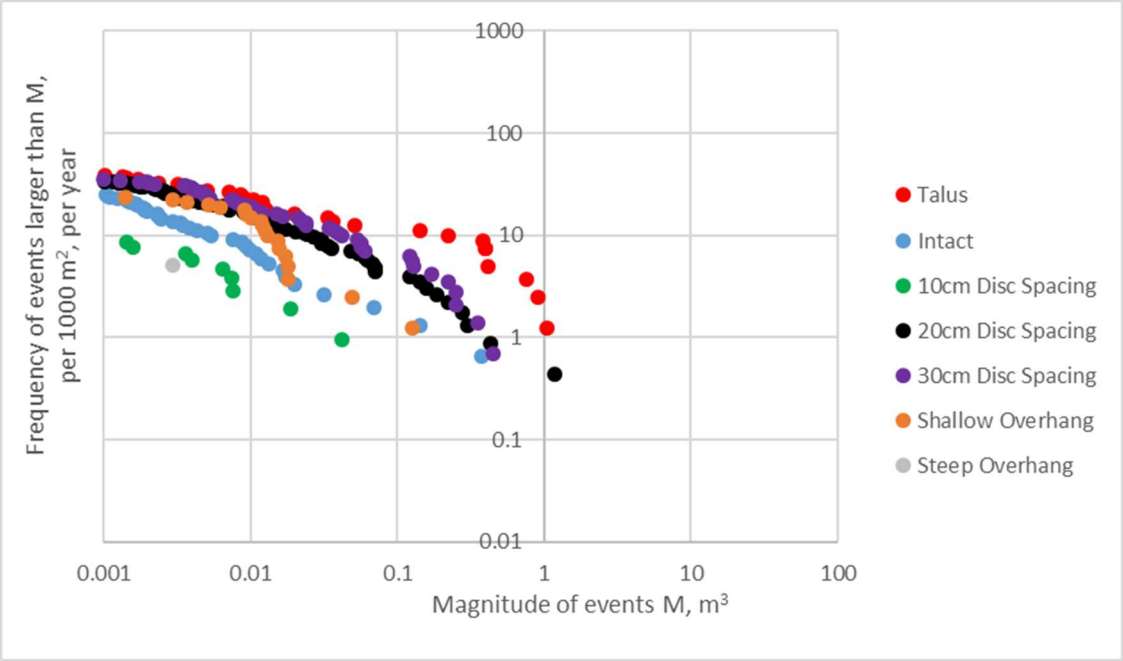

Figure 82. LL87 RAI Class Cumulative Size-Frequency Curve for 2012-2017

Box-and-whisker plots showing distributions of size-frequency parameters and recession rates for different RAI Classes are provided below, in Figures 83 through 85.

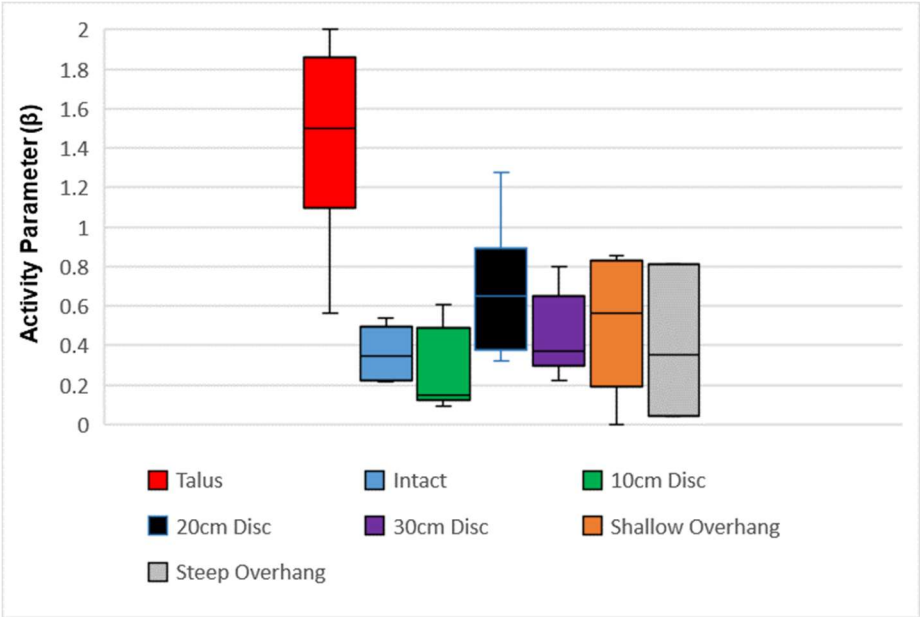

Figure 83. Box-and-whisker plot of the Activity Parameter for all sites and change epochs.

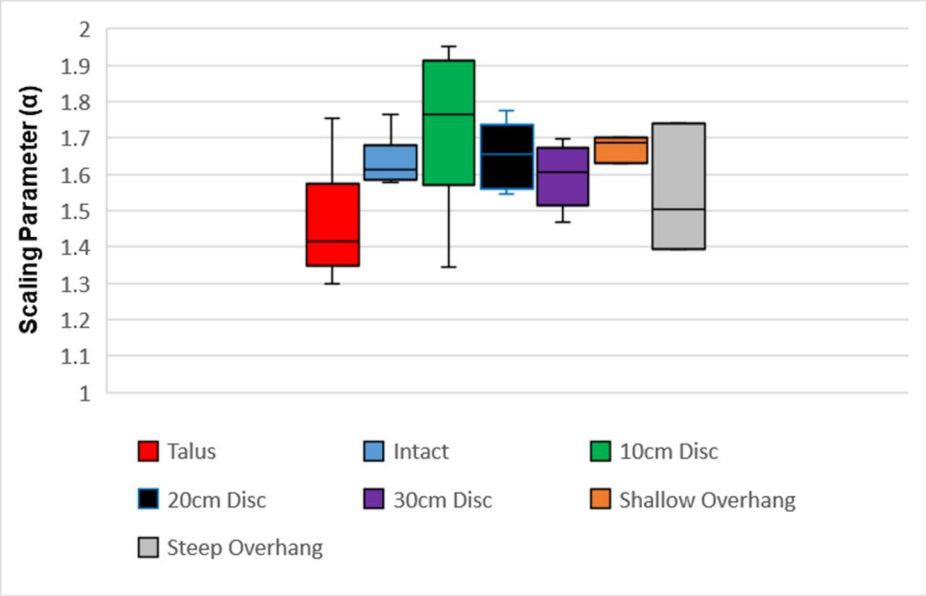

Figure 84. Box-and-whisker plot of the Scaling Parameter for all sites and change epochs.

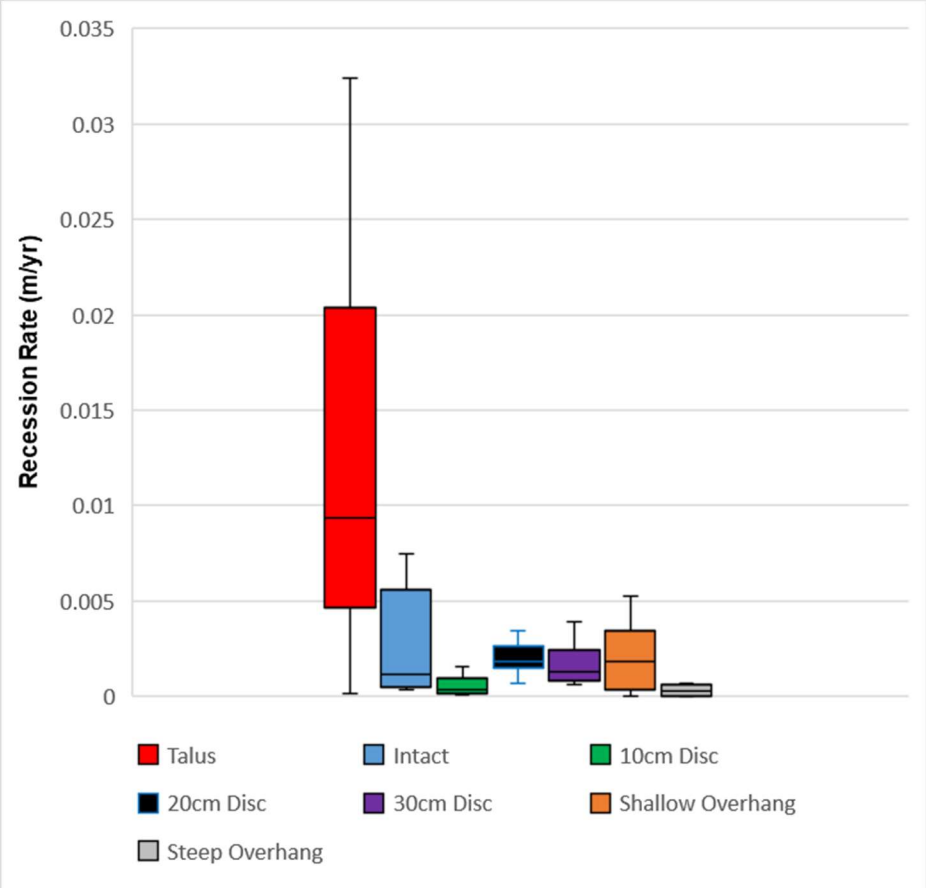

Figure 85. Box-and-whisker plot of the annual recession rate for all sites and change epochs.

Size-frequency parameters and recession rates have a definite distinction between RAI Classes, in both their means and their variability. It is obvious that the RAI classification methodology is at least somewhat capturing distinct mass wasting processes in each of the different classes. Talus has the most distinct behavior of all the RAI Classes. Talus tends to fail much more often, and involve much larger failures, than the other RAI Classes, leading to a much higher recession rate. These values are available below, in Table 13, for reference.

RAI Class	Average Activity, β	σ of β	CoV of β	Average Scaling, α	σ of α	CoV of α	Average Slope Recession Rate (m/yr)	σ of Slope Recession Rate	CoV of Slope Recession Rate
Talus	1.441	0.460	0.319	1.461	0.146	0.010	0.012	0.010	0.835
Intact	0.358	0.119	0.333	1.634	0.063	0.039	0.003	0.003	1.035
10cm Disc	0.264	0.195	0.739	1.729	0.208	0.120	0.001	0.0005	0.895
20cm Disc	0.676	0.311	0.460	1.653	0.081	0.049	0.002	0.001	0.417
30cm Disc	0.448	0.194	0.434	1.595	0.078	0.049	0.002	0.001	0.658
Shallow Overhang	0.611	0.259	0.424	1.635	0.123	0.075	0.002	0.002	0.662
Steep Overhang	0.400	0.316	0.789	1.547	0.144	0.093	0.0002	0.0003	1.218

Table 13. Average size-frequency parameters and slope recession rates for the RAI Classes at all sites, for all epochs.

2.6 Temporal Variation of Size-Frequency Distributions for each RAI Class

To investigate year-to-year changes in the shape of the size-frequency distribution, Figures 86 through 88 show variations in the parameters and the recession rates through time at Long Lake Site 71. The other sites were omitted due to their small sample size; sampling error would skew the data for these sites.

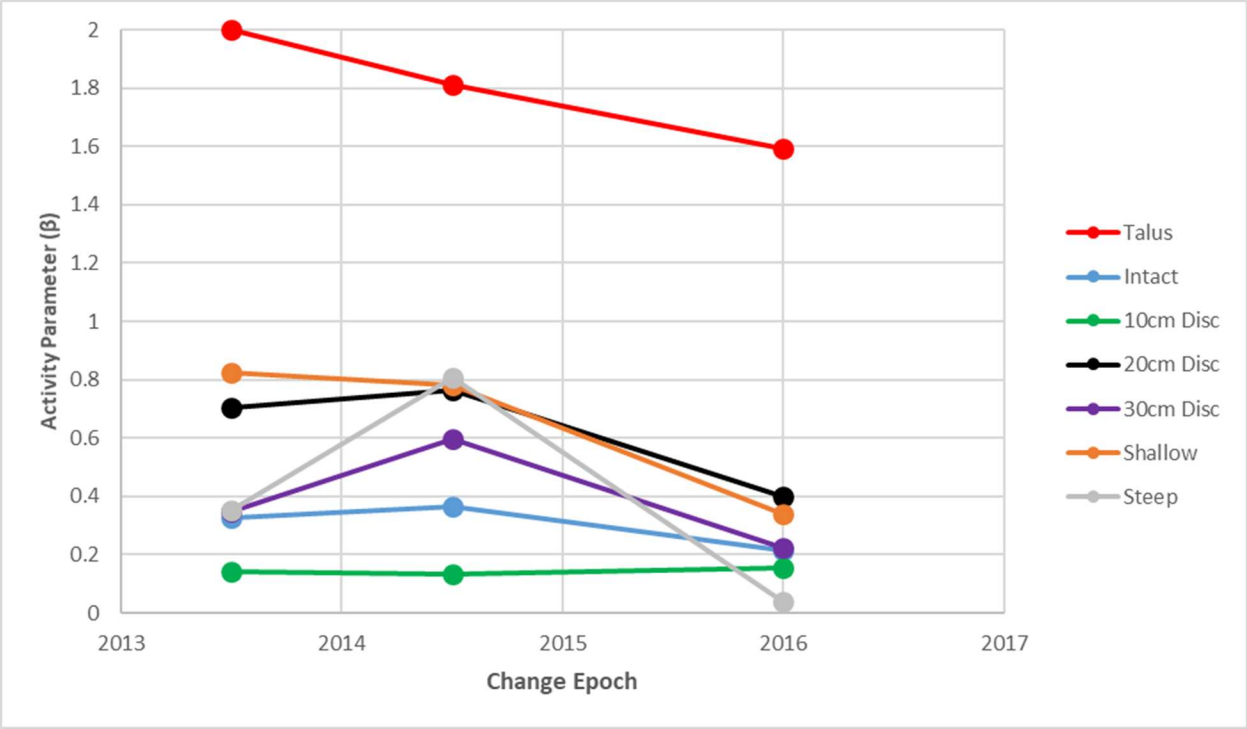

Figure 86. Variation of the Activity Parameter for different RAI Classes through time, at LL71.

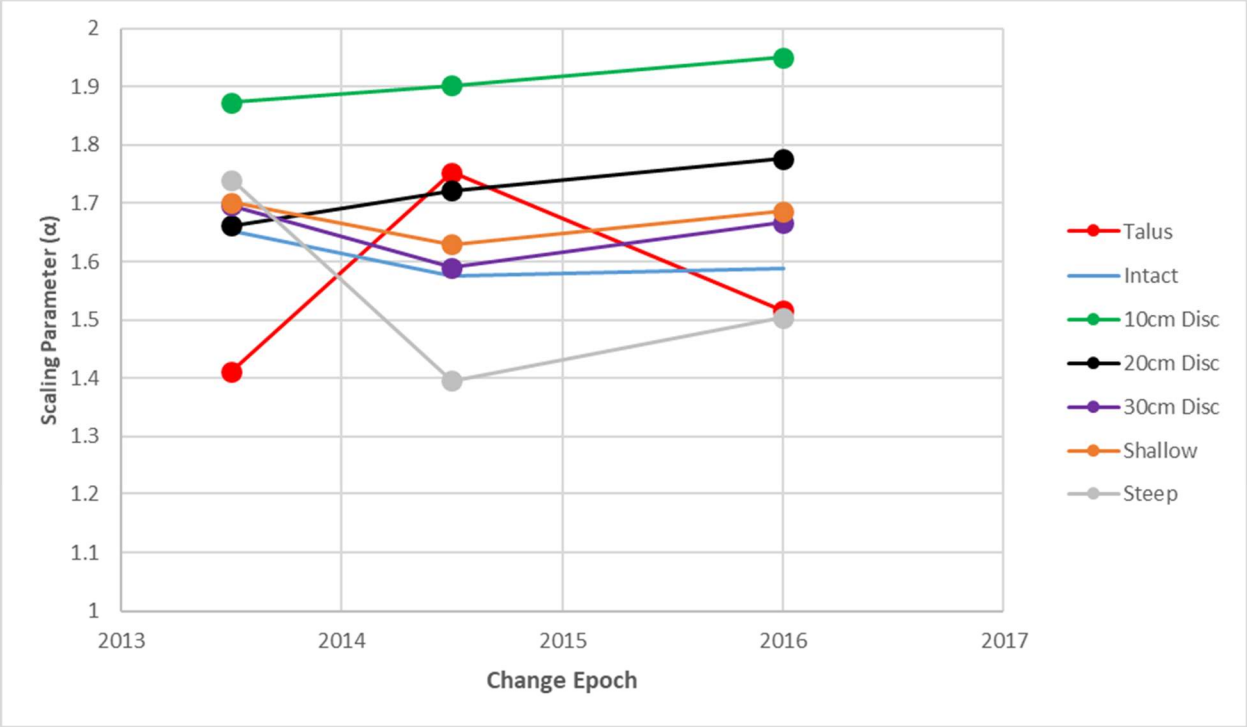

Figure 87. Variation of the Scaling Parameter for different RAI Classes through time, at LL71.

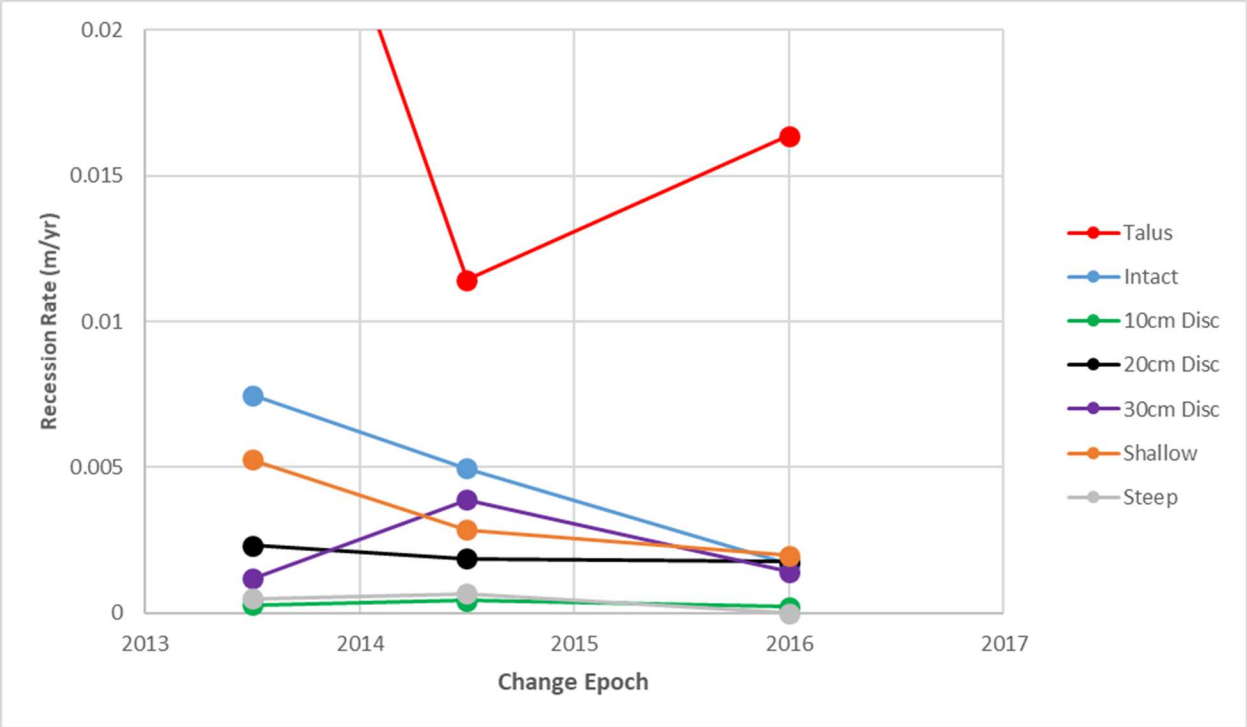

Figure 88. Variation of the Recession Rate for different RAI Classes through time, at LL71.

Interestingly, the dramatic drop in overall recession rate during the last epoch at LL71 was attributed to all classes but the Talus; recession rates in the Talus surprisingly increased dramatically in the lower-activity epoch between 2015 and 2017, and failure sizes decreased slightly. Recession rates from the intact and very rough surfaces dramatically reduced in the 2015-2017 epoch, and the decline in the activity rate shows this trend. Failures in the non-talus areas did tend to get slightly larger during this time period, however. Appendix B provides the raw size-frequency parameters and recession rate measurements for the RAI Classes, for the data analyzed.

2.7 Summary of Fluctuations in Size-Frequency Distributions

To reiterate the findings from these size-frequency distributions and associated parameters, it appears that RAI Classification is differentiating between mass-wasting processes fairly well. Distinction in processes between sites and between epochs is also prevalent, though less so than between RAI Classes. Generally, RAI Classes of similar nature (the discontinuity classes, the overhangs, etc.) have size-frequency parameters that trend similarly through time (see Figures 86 through 88). Enough distinction is visible in size-frequency parameters and recession rate to deduce that the RAI Classification slope process mapping is capturing significantly different behavior between slope areas.

3. Relationship between Cloud Parameters and Failure Characteristics

The RAI Classification methodology assumes that there is a significant relationship between roughness (and roughness at different scales) and size-frequency distributions of failure events. The validity of this assumption is investigated at Long Lake Site 71 (because of the large sample size) in the following section. Additionally, Curvature was investigated as a potential prediction parameter in this study.

3.1 Correlation between Roughness and Failure Probability

Firstly, the average baseline roughness for subsequently failed and non-failed points was simply compared for all roughness window sizes at LL71. This data is available in Table 14 through Table 16, below.

Window Size (cm x cm)	15	25	35	45	55	65	75	85	95	105
Failed Points										
Avg Roughness (Deg)	5.235	6.334	6.942	7.361	7.682	7.936	8.152	8.343	8.511	8.659
Standard Deviation	6.184	6.716	6.994	7.189	7.338	7.454	7.550	7.637	7.711	7.779
Non-Failed Points										
Avg Roughness (Deg)	4.710	5.837	6.501	6.966	7.318	7.599	7.832	8.029	8.201	8.352
Standard Deviation	5.605	6.240	6.597	6.842	7.025	7.169	7.288	7.387	7.473	7.549

Table 14. Average roughness values for failed and non-failed points for LL71, 2013-2014 dataset.

Window Size (cm x cm)	15	25	35	45	55	65	75	85	95	105
Failed Points										
Avg Roughness (Deg)	7.552	9.231	10.173	10.779	11.205	11.524	11.776	11.985	12.162	12.318
Standard Deviation	5.123	5.380	5.466	5.496	5.504	5.500	5.491	5.477	5.458	5.442
Non-Failed Points										
Avg Roughness (Deg)	6.287	7.849	8.796	9.462	9.970	10.377	10.714	11.001	11.249	11.467
Standard Deviation	4.507	4.894	5.075	5.181	5.249	5.292	5.321	5.340	5.353	5.361

Table 15. Average roughness values for failed and non-failed points for LL71, 2014-2015 dataset.

Window Size (cm x cm)	15	25	35	45	55	65	75	85	95	105
Failed Points										
Avg Roughness (Deg)	6.433	7.826	8.585	9.084	9.454	9.746	9.989	10.198	10.384	10.552
Standard Deviation	6.149	6.569	6.755	6.858	6.924	6.970	7.004	7.031	7.053	7.072
Non-Failed Points										
Avg Roughness (Deg)	5.424	6.852	7.704	8.296	8.743	9.098	9.391	9.639	9.853	10.042
Standard Deviation	5.404	6.032	6.353	6.556	6.699	6.808	6.893	6.963	7.022	7.073

Table 16. Average roughness values for failed and non-failed points for LL71, 2015-2017 dataset.

There is a slight difference between average baseline roughness values between subsequently Failed Points and subsequently Non-Failed Points in all data sets. For all roughness window sizes and all data analyzed, failed points had a slightly higher average roughness than non-failed points. Figure 89**,** below, shows the difference in average roughness between failed and non-failed points for the various window sizes, for the three change epochs analyzed.

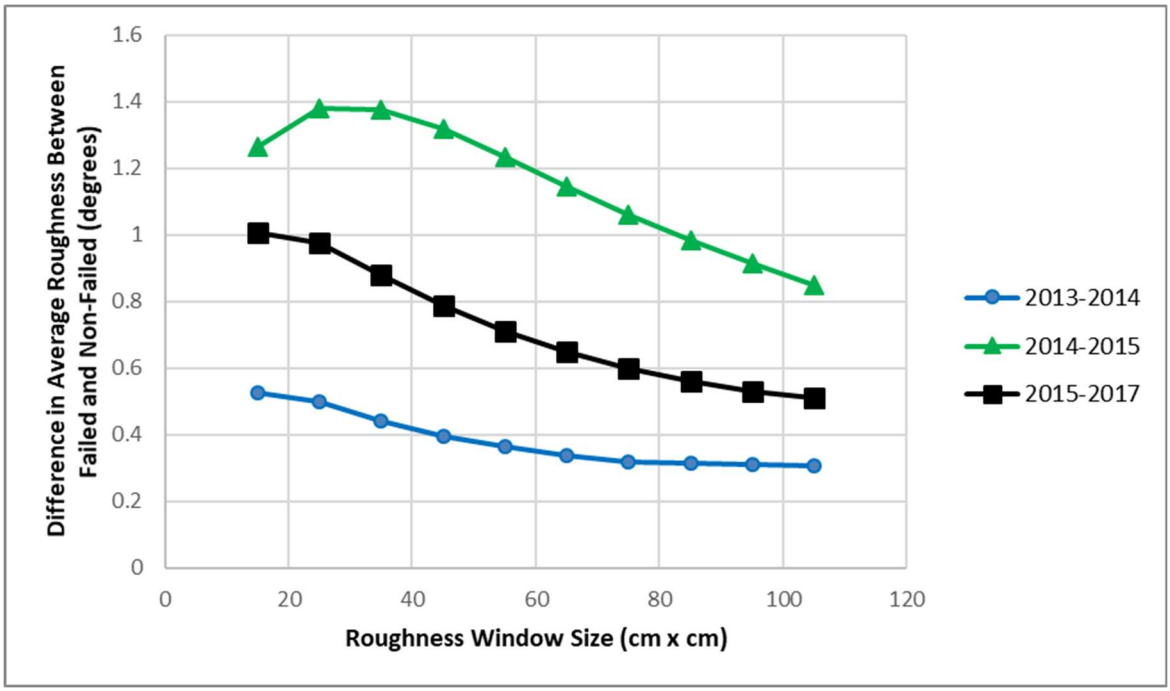

Figure 89. Difference in average roughness between Failed and Non-Failed Points at Long Lake Site 71

. As seen above, roughness over a small window size seems to more clearly predict general probability of failure than roughness at larger window sizes. To further investigate the efficacy of using roughness to predict failure, Figures 90 and 91 show the Probability Density Functions (PDFs) of roughness, for both failed and non-failed points, at the 35-cm and 85-cm roughness window size. Non-failed points are solid lines and failed points are dashed lines. The three change epochs are again included in the following plots. The RAI Class thresholds chosen by Dunham *et al.* (2017) are shown as red vertical dashed lines in the following plots.

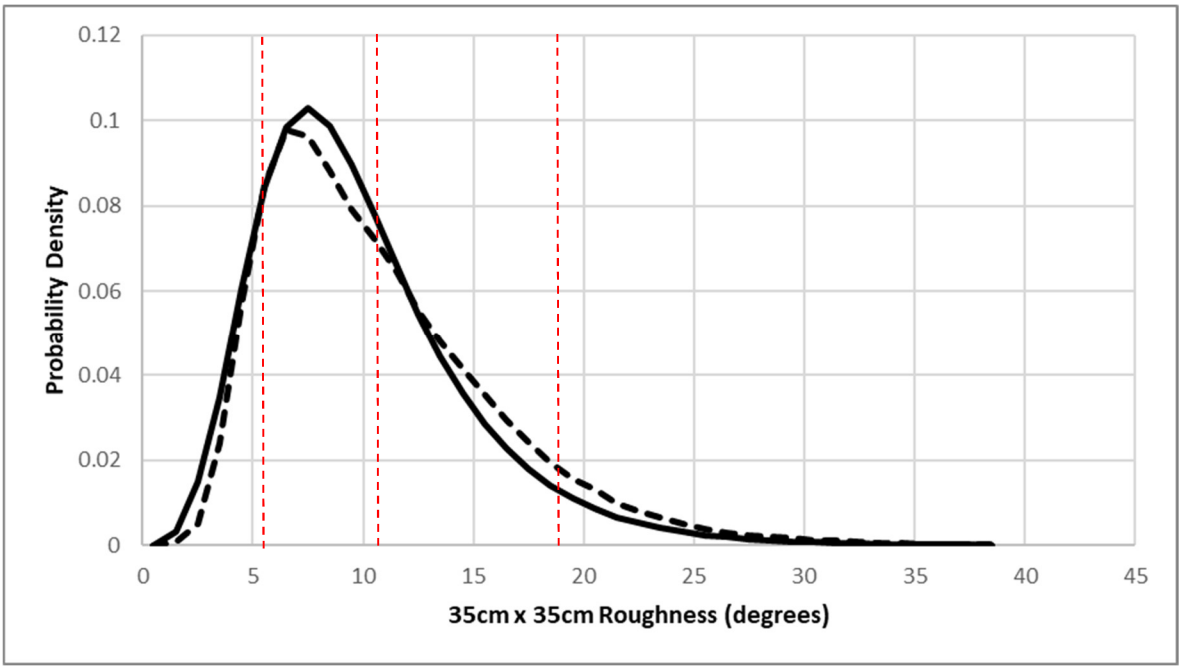

Figure 90. Roughness Probability Densities of non-failed (solid) and failed (dashed) points for LL71, for all change epochs; 35cm x 35cm Roughness Window

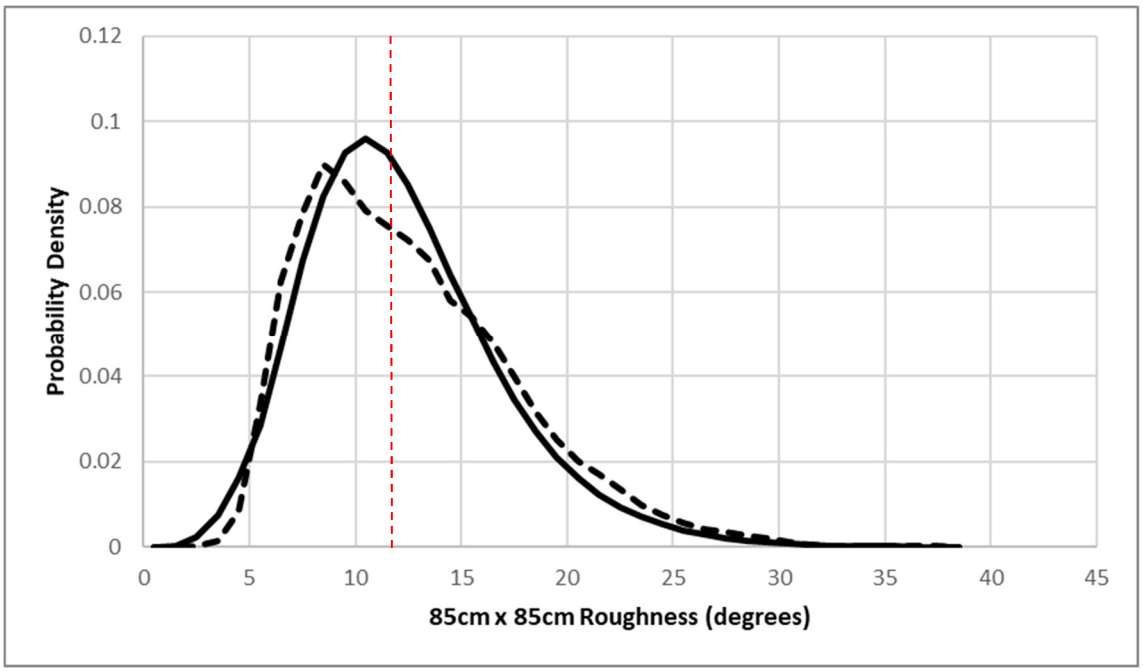

Figure 91. Roughness Probability Densities of non-failed (solid) and failed (dashed) points for LL71, for all change epochs; 85cm x 85cm Roughness Window

Small differences in roughness distributions in failed and non-failed points are visible in this plot, though the difference is not pronounced. To investigate the effect of talus activity on skewing these plots, the following figures, Figures 92 and 93, show the same PDFs considering only points on terrain steeper than 45 degrees from horizontal.

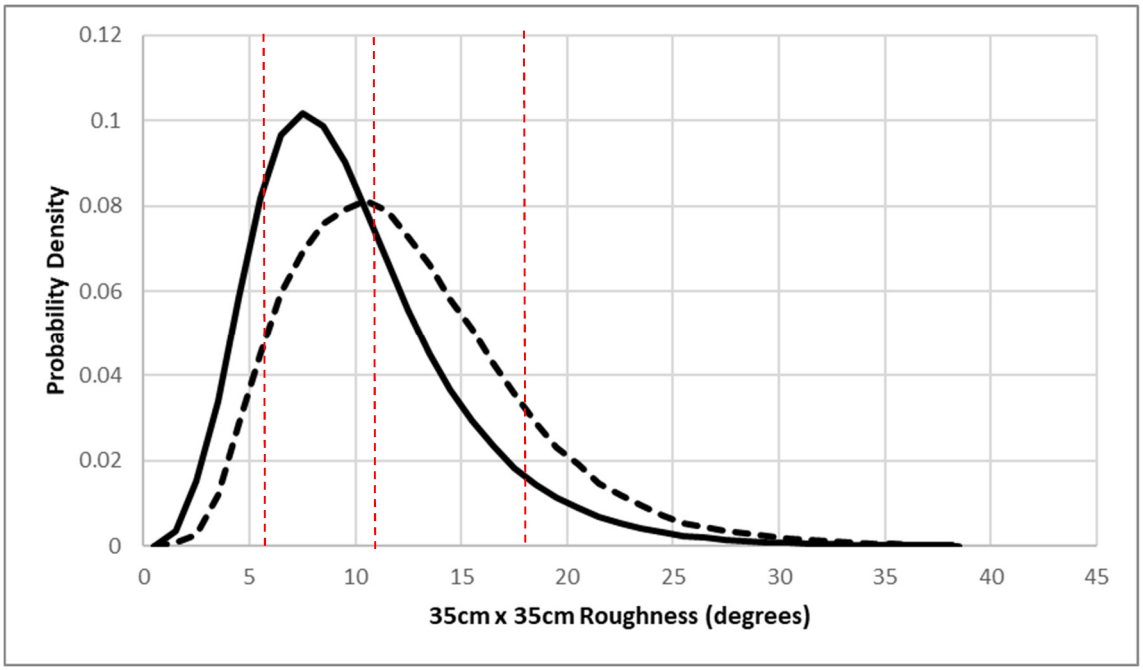

Figure 92. Roughness Probability Densities of non-failed (solid) and failed (dashed) points for LL71, for all change epochs, omitting data shallower than 45 degrees; 35cm x 35cm Roughness Window

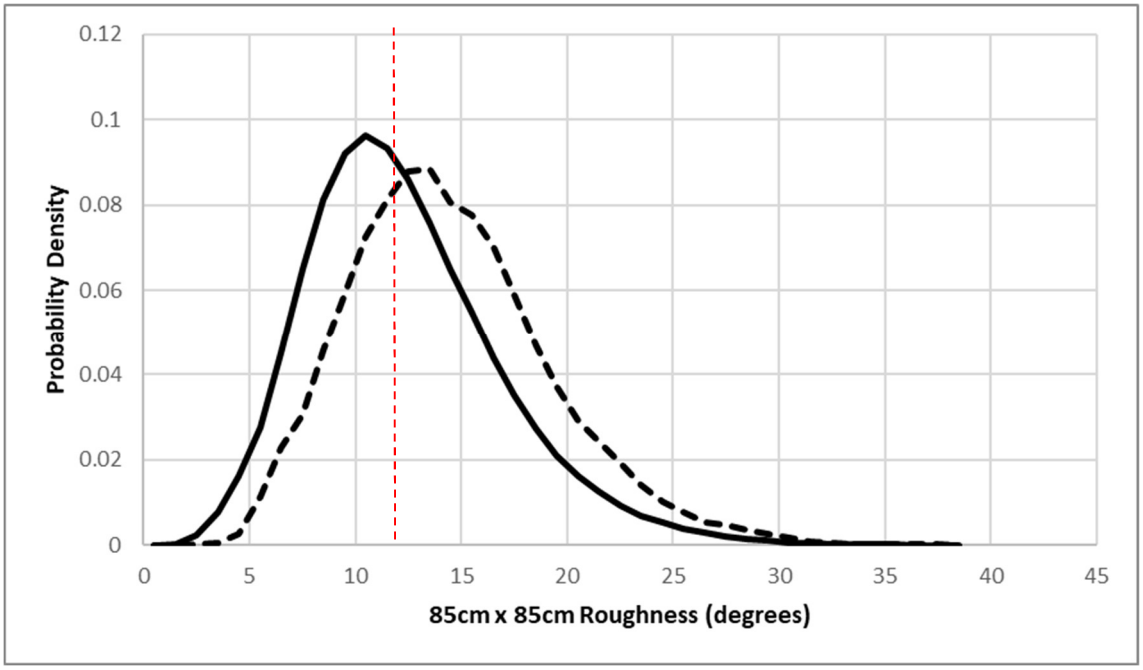

Figure 93. Roughness Probability Densities of non-failed (solid) and failed (dashed) points for LL71, for all change epochs, omitting data shallower than 45 degrees; 85cm x 85cm Roughness Window

The baseline roughness parameter is a significantly different predictor of failure on steep slopes than on shallower slopes; all following analyses for roughness and curvature will only investigate terrain that is steeper than 45 degrees from horizontal, and therefore cannot include talus slopes, unless otherwise noted.

These plots show that roughness is at least a factor in the likelihood of a point to fail. These plots also show that the roughness thresholds utilized by Dunham e*t al.* differentiate between the character of the PDF's remarkably well. As shown in Section 1.5, the RAI system differentiates between Intact Rock/Talus, 10cm-spaced Discontinuities, 20cm-spaced Discontinuities, and 30cm-spaced Discontinuities by 35cm x 35cm roughness as the primary factor (using the thresholds shown in the plot), and 85cm x 85cm as a secondary factor (using the threshold shown in that plot).

A correlation simply between roughness and probability of a point to fail is shown below. Figures 94 and 95 show the probability of a point to fail given its roughness parameter for all change epochs at Long Lake Site 71; both the 35 cm x 35 cm and 85cm x 85cm window sizes are shown below. Again, the vertical dashed red lines indicate roughness thresholds selected by Dunham *et al*. (2017).

Figure 94. Annual probability of failure given 35cm x 35cm roughness for all change epochs, omitting data shallower than 45 degrees from horizontal

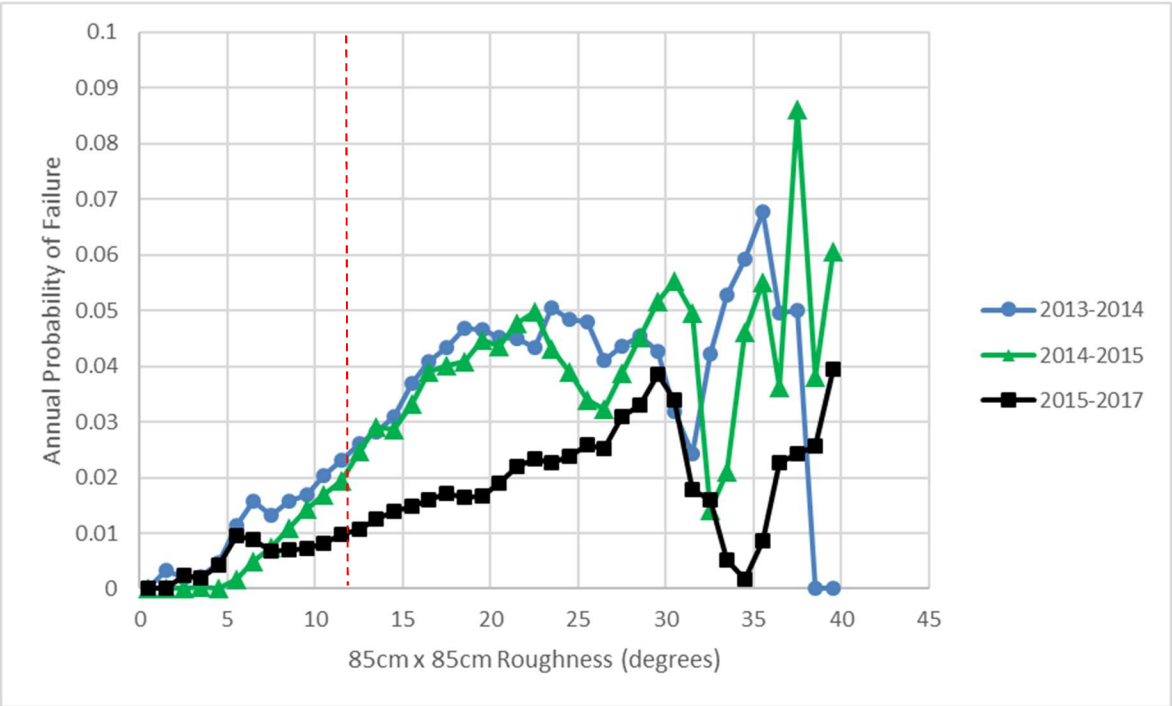

Figure 95. Annual probability of failure given 85cm x 85cm roughness for all change epochs, omitting data shallower than 45 degrees from horizontal

In both roughness windows, roughness appears to be directly correlated with failure probability across all change epochs. In the relatively inactive epoch, 2015-2017, the positive correlation is less pronounced though still linear. This correlation holds true until a certain threshold, above which the correlation is lost. By reviewing the scans, it becomes apparent that areas that are calculated as very rough are typically near data holes or vegetation, where detecting change is difficult; this is especially true for larger roughness windows.

The roughness thresholds differentiating between RAI Class again seem to correlate well to point failure probability. The methodology in Dunham *et al. (2017)*, however, classifies activity rates outright by these thresholds, whereas, as discussed above, the relationship between probability of failure and roughness seems to be a gradient, rather than a threshold.

As previously discussed, talus is generally a very active material. In order to examine the efficacy of roughness in determining activity of low-angle areas, probability of a point to fail for different roughnesses was analyzed for only low-angle slope areas (below 45 degrees from horizontal). See Figures 96 and 97, below.

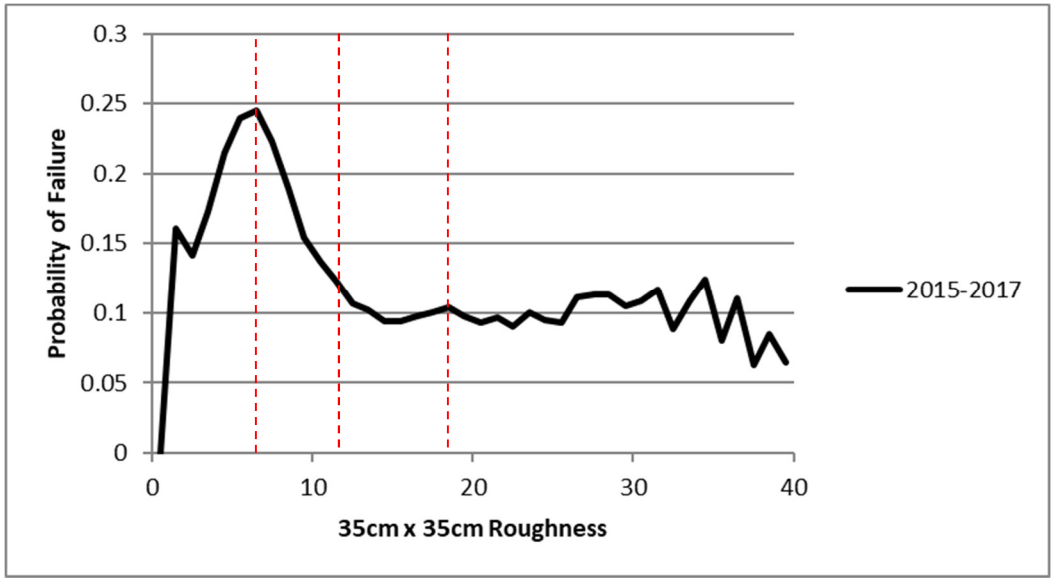

Figure 96. Probability of Failure of slopes less than 45 degrees, vs 35cm x 35cm roughness parameters at LL71.

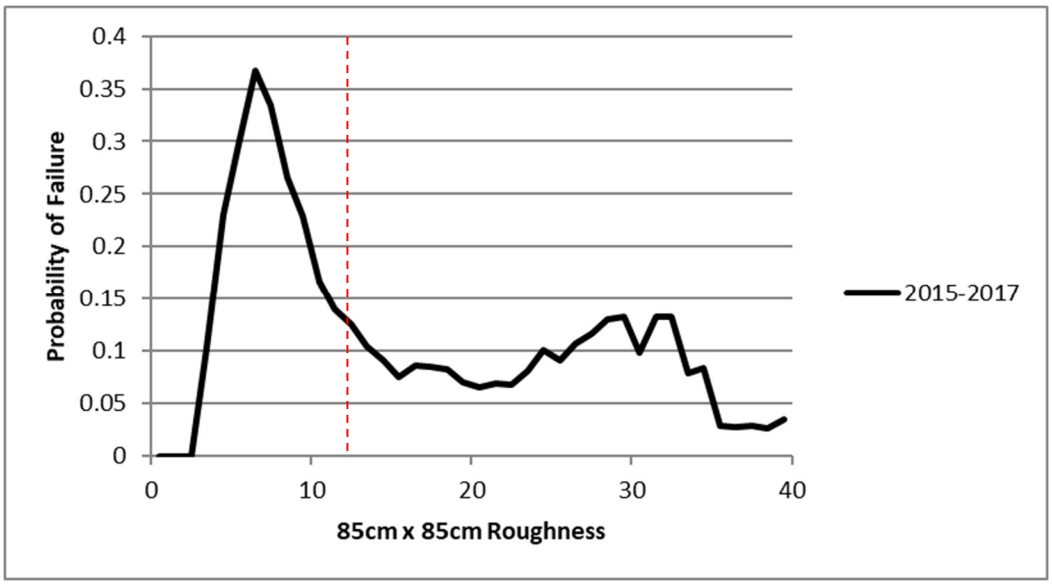

Figure 97. Probability of Failure of slopes less than 45 degrees, vs 85cm x 85cm Roughness Parameter

These figures show that failure is much more probable on smooth areas in low-angle portions of the rock-slope. The RAI system currently classifies Talus as slope areas with $R_{35} < 6^o$, or $R_{35} < 11^o$ and $R_{85} < 12^o$; these talus slopes seem to have a very distinct failure rate compared to other terrain features.

3.2 Correlation between Roughness and Failure Size

The Rockfall Activity Index methodology strives to not only associate failure rate with RAI Classification (and therefore roughness), but it aims to provide insight into likely failure scales that may occur in specific slope areas. In order to investigate whether roughness can be a predictor of failure scale, the same probability of failure vs. roughness plots are presented below (in Figures 98 and 99), for different depths of failure. The failure depths are color coded in this plot, from shallow (cold) to deep (hot). As previously discussed, roughness is calculated as the standard deviation of slope over different window sizes; two window sizes (35-cm and 85-cm) were investigated in this study.

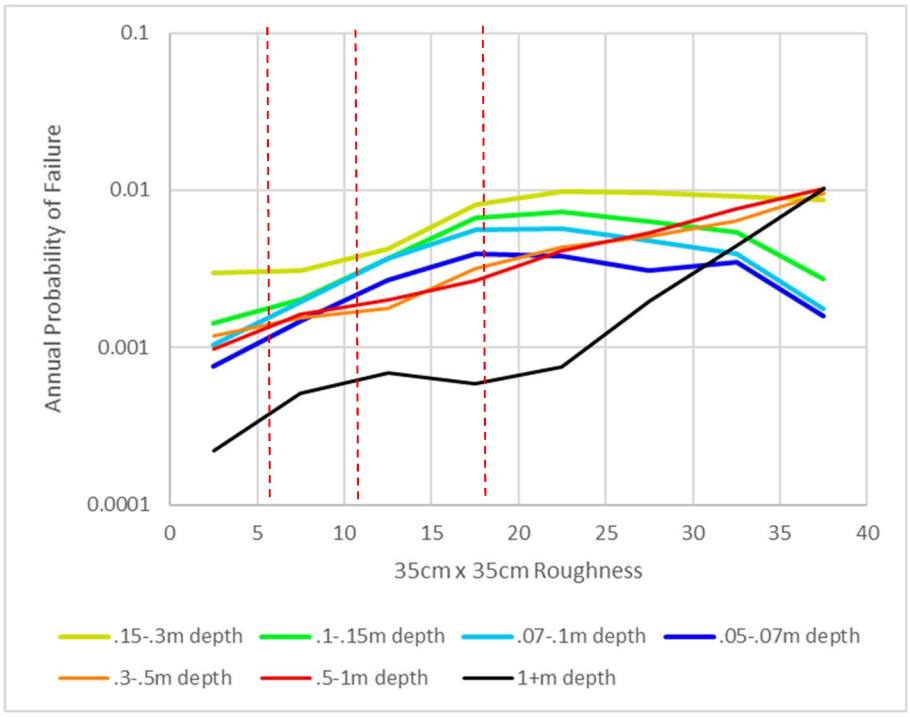

Figure 98. Annual probability of failure given 35cm x 35cm roughness, for all change epochs, to certain failure depths (coded by color). Data shallower than 45 degrees from horizontal is omitted.

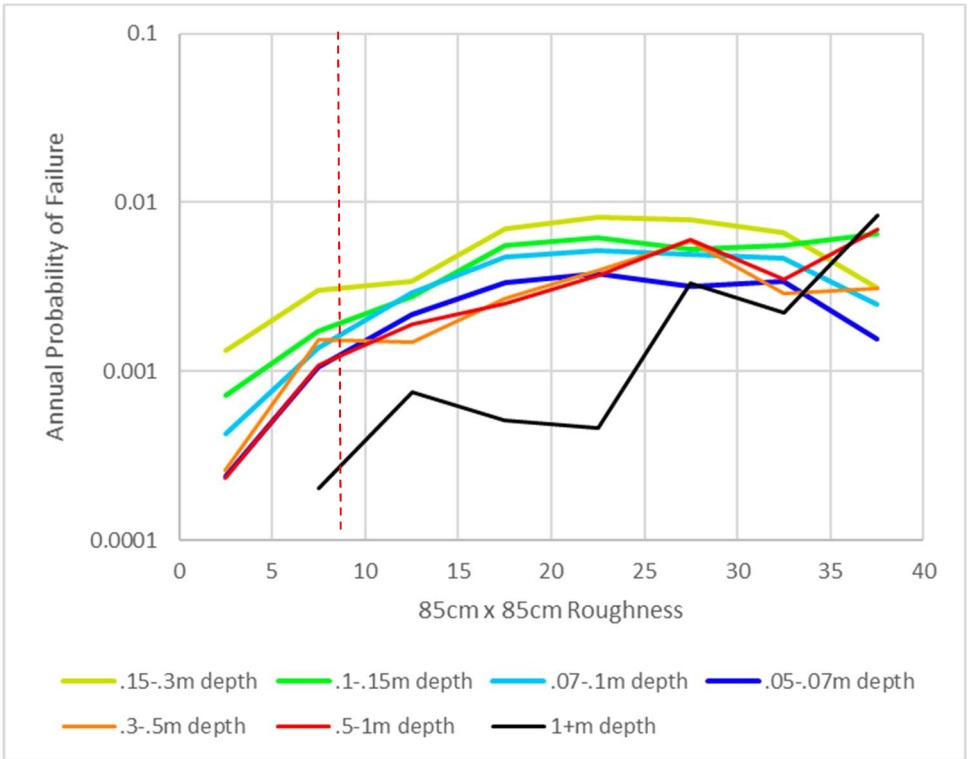

Figure 99. Annual probability of failure given 35cm x 35cm roughness, for all change epochs, to certain failure depths (coded by color). Data shallower than 45 degrees from horizontal is omitted.

Note how the two plots are remarkably similar. At very high roughness values, the probability of shallow failures does not continue to scale with roughness. Contrarily, the probability of deep failures seems to rise dramatically at very high roughness values. Therefore, roughness appears to be correlated with shallow failures at smaller roughness values, and larger failures at larger roughness values; the methodology proposed by the RAI system appears to have a statistical basis in this regard. Figures 100 and 101, below, show size-frequency distributions for the depth of failure of points, for different roughness values (that are color coded).

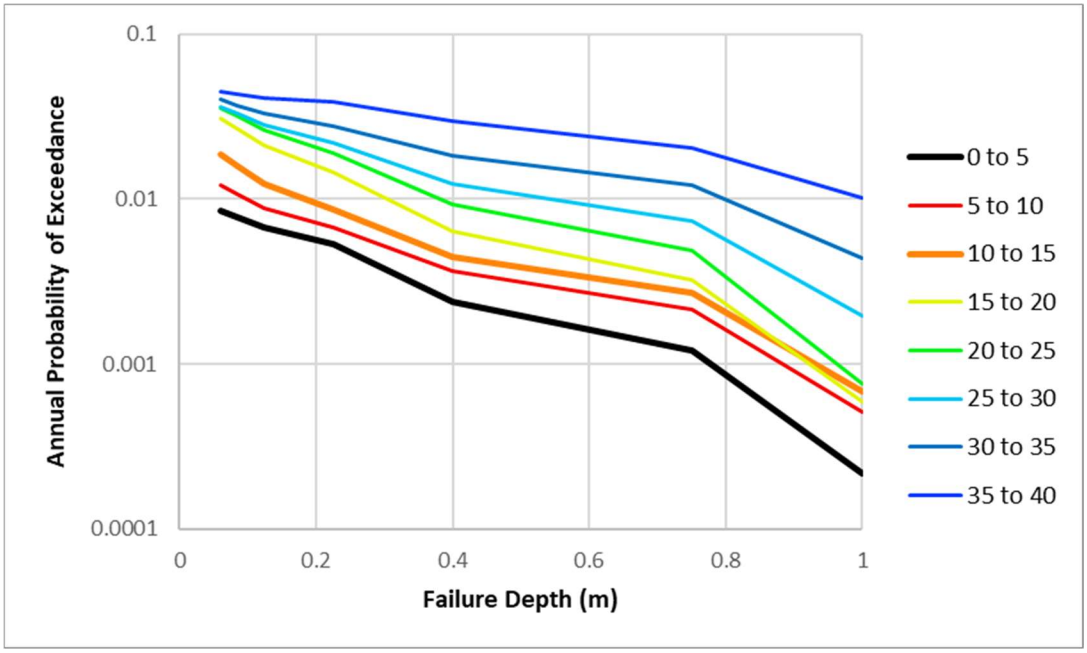

Figure 100. Size-frequency distributions describing annual probability of exceedance of certain failure depths, for given roughnesses, measured in a 35cm x 35cm window. Data shallower than 45 degrees from horizontal is omitted.

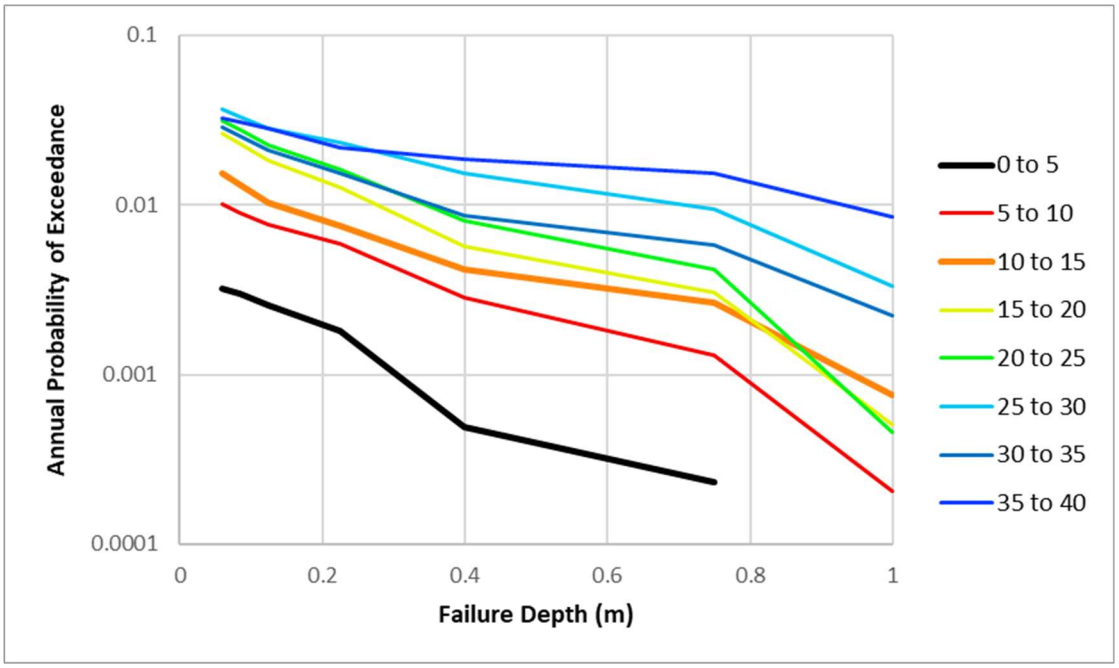

Figure 101. Size-frequency distributions describing annual probability of exceedance of given failure depths, for different roughnesses, measured in an 85cm x 85cm window. Data shallower than 45 degrees from horizontal is omitted.

Again note the similarity between these two plots. These plots reiterate that smooth areas have a low probability to fail to shallow or deep depths, and rough areas have a higher probability to fail to shallow or deep depths, regardless of the roughness window size. It should be noted that the probability to fail to different depths is similarly predicted by small-scale roughness as it is by larger-scale roughness. This is counter-intuitive. One would assume that roughness window size may be correlated to discontinuity spacing, and therefore would be correlated to the scale of asperities and geometries that lead to increased probability of larger failures. The data shows that failure size probability is unrelated to the scale of roughness. Therefore, the RAI system is properly relating elevated roughness at both considered window sizes with both elevated failure rates and elevated failure sizes. As discussed in the next section, other point cloud parameters may be able to address failure scale more properly.

3.3 Correlation between Curvature and Failure Probability

The relationship between point curvature and point probability of failure was investigated as well. The average baseline curvature for subsequently failed and non-failed points was compared for all curvature window sizes at Long Lake Site 71. This data is available in Table 17 through Table 19, below.

Window Size (cm x cm)	15	25	35	45	55	65	75	85	95	105
Failed Points										
Avg Curvature	34.1	45.5	44.7	40.2	34.1	27.9	23.2	19.4	15.8	12.8
Standard Deviation	3917	1421	801	537	400	318	263	222	192	168
Non-Failed Points										
Avg Curvature	-3.3	-2.1	0.8	1.9	2.0	1.9	1.8	1.4	1.2	1.0
Standard Deviation	3282	1222	698	479	363	291	242	206	180	159

Table 17. Average curvature values for failed and non-failed points for LL71, 2013-2014 dataset.

Window Size (cm x cm)	15	25	35	45	55	65	75	85	95	105
Failed Points										
Avg Curvature	74.5	51.6	34.0	22.0	14.6	9.1	5.5	3.2	1.4	0.0
Standard Deviation	3708	1476	854	591	447	356	293	247	212	184
Non-Failed Points										
Avg Curvature	-33.5	-12.6	-4.6	-1.7	-0.6	-0.1	0.0	0.0	-0.1	-0.3
Standard Deviation	2394	1011	616	439	341	277	233	200	175	155

Table 18. Average curvature values for failed and non-failed points for LL71, 2014-2015 dataset.

Window Size (cm x cm)	15	25	35	45	55	65	75	85	95	105
Failed Points										
Avg Curvature	131.1	95.6	91.5	77.9	64.5	53.0	44.0	36.8	31.1	26.6
Standard Deviation	5562	2097	1174	776	562	432	347	287	243	210
Non-Failed Points										
Avg Curvature	7.9	1.9	0.9	0.5	0.4	0.2	0.0	-0.1	-0.1	-0.2
Standard Deviation	3277	1297	752	516	388	310	257	220	192	170

Table 19. Average curvature values for failed and non-failed points for LL71, 2015-2017 dataset.

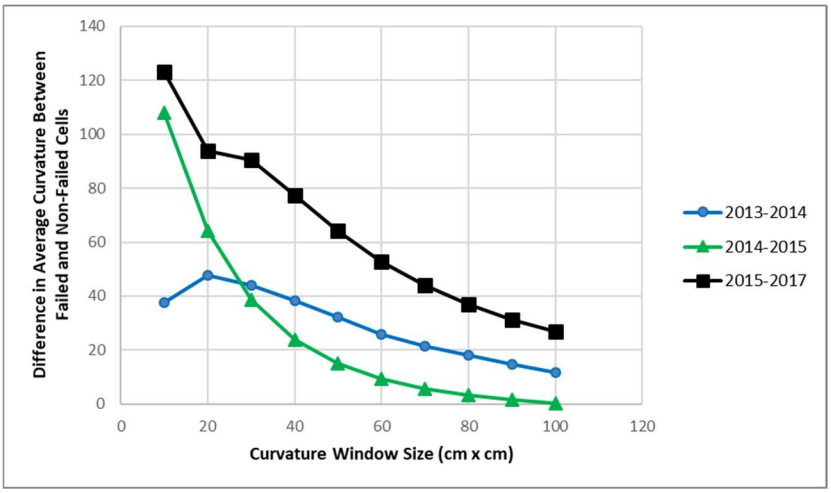

Figure 102. Difference in average curvature between Failed and Non-Failed Points at Long Lake Site 71.

Like roughness, when the averages of curvature for failed and non-failed points are inspected, one can conclude that smaller curvature window sizes better predict probability of failure than larger window sizes. Figures 103 and 104, below, show PDFs for curvature over the same two window sizes (35cm x 35cm and 85cm x 85cm).

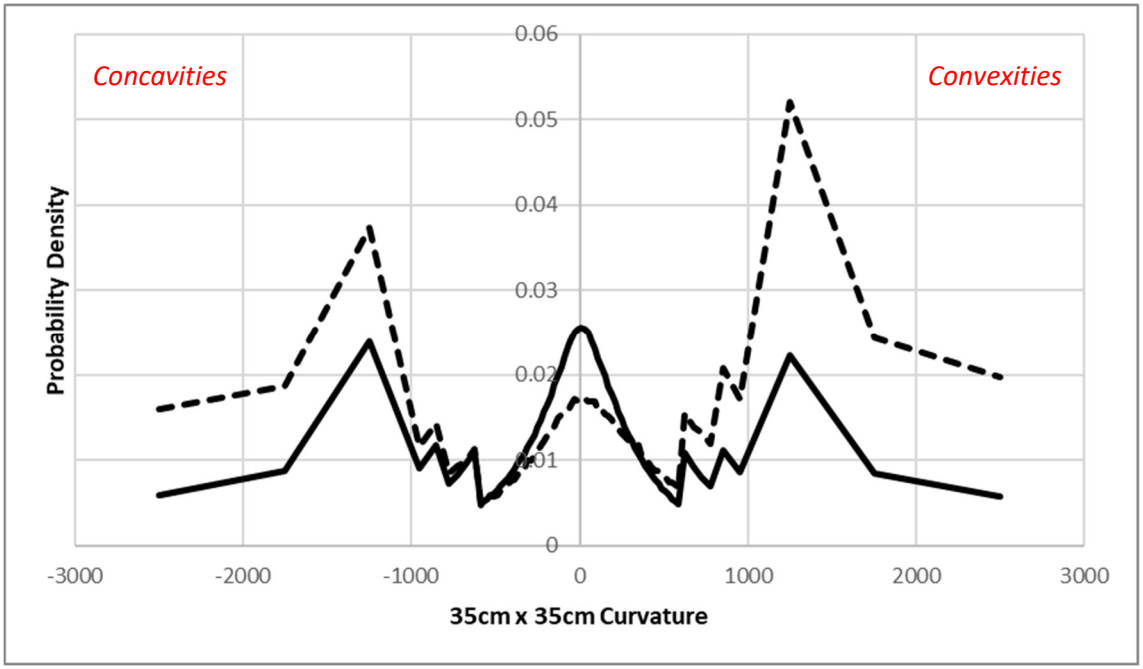

Figure 103. Curvature Probability Densities of non-failed (solid) and failed (dashed) points for LL71, for all change epochs, omitting data shallower than 45 degrees; 35cm x 35cm Curvature Window

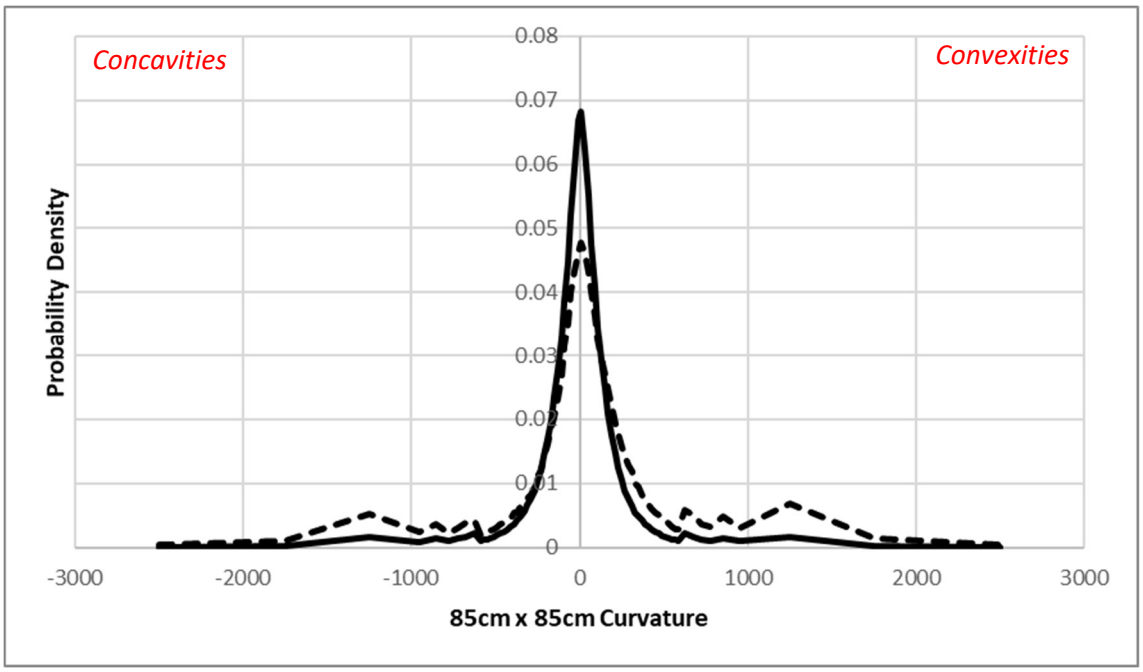

Figure 104. Curvature Probability Densities of non-failed (solid) and failed (dashed) points for LL71, for all change epochs, omitting data shallower than 45 degrees; 85cm x 85cm Curvature Window

From these plots, it is evident that curvature can also be used to determine probability of point failure. Points that failed have typically very high or very low curvature values, and more rarely have curvature values near 0, in both analyzed window sizes. It is also apparent that areas with positive curvature are more prone to failing than areas with negative curvature. In Figures 105 and 106, below, we show the probability of failure given curvature for the all change epochs at Long Lake Site 71.

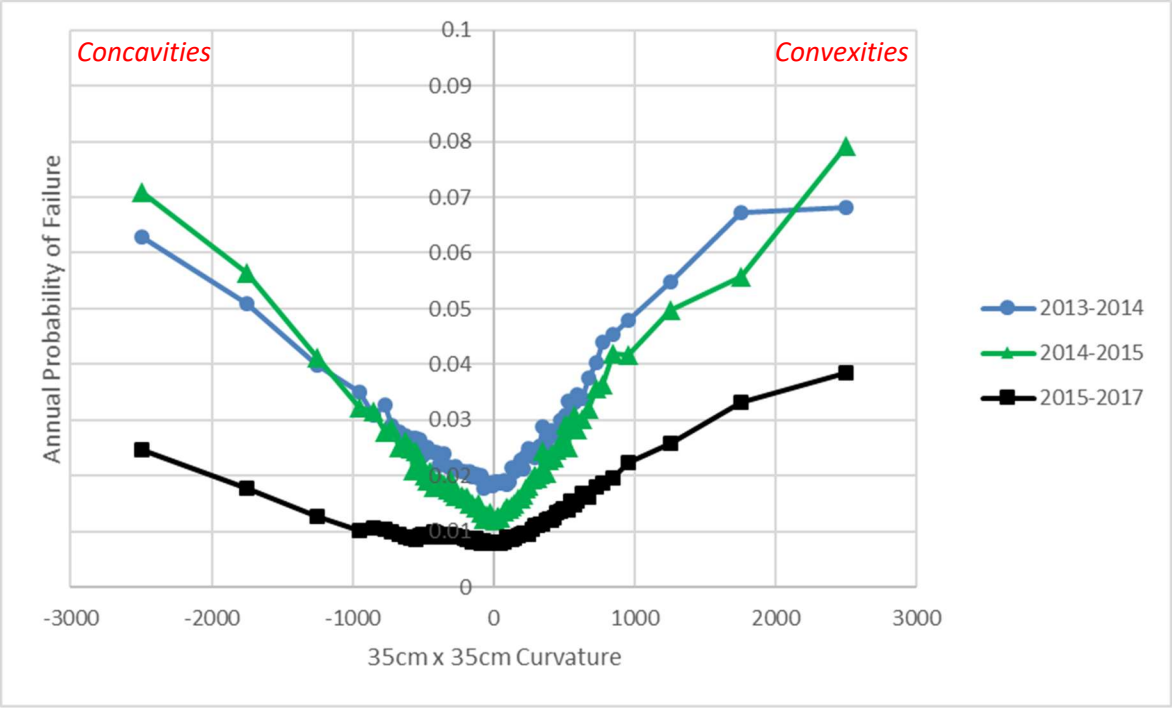

Figure 105. Annual probability of failure given 35cm x 35cm curvature for all change epochs, omitting data shallower than 45 degrees from horizontal

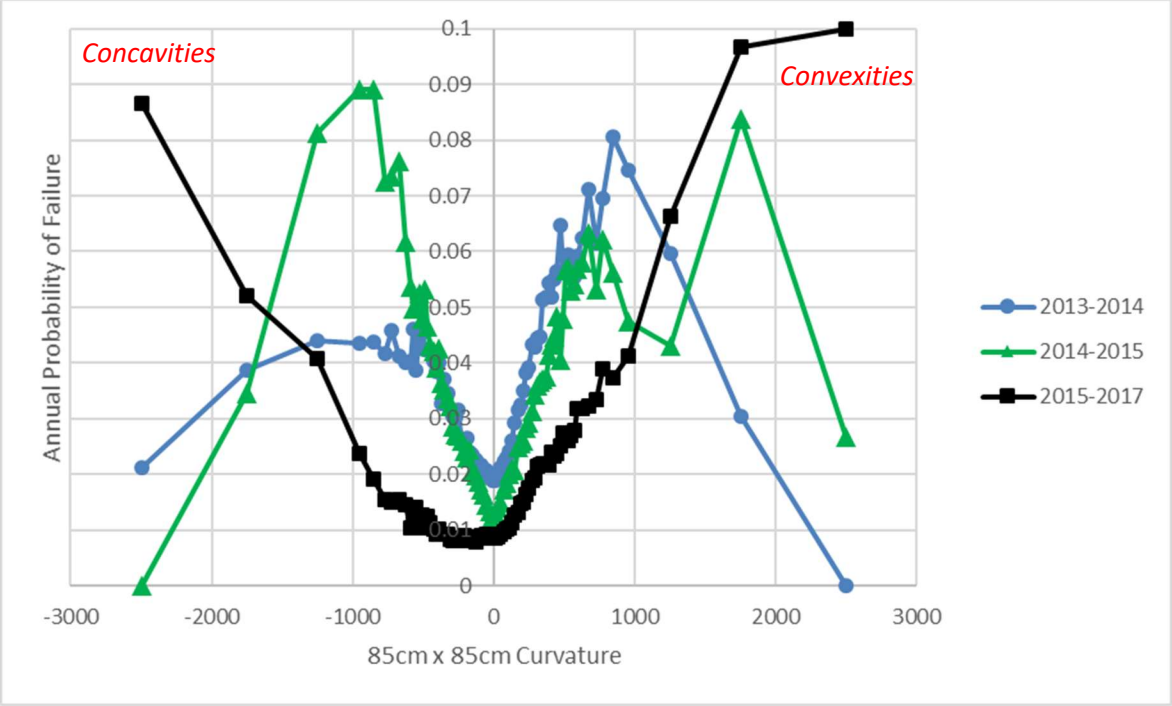

Figure 106. Annual probability of failure given 85cm x 85cm curvature for all change epochs, omitting data shallower than 45 degrees from horizontal

Generally, it appears that failure probability is somewhat independent of the direction of curvature; both concave and convex surfaces are more likely to fail than planar surfaces. This is notably less evident in the 2015-2017 data set, however. In that set, convex features appeared to be significantly more likely to fail than concave features. Below are plots of the probability of failure given the absolute value of curvature.

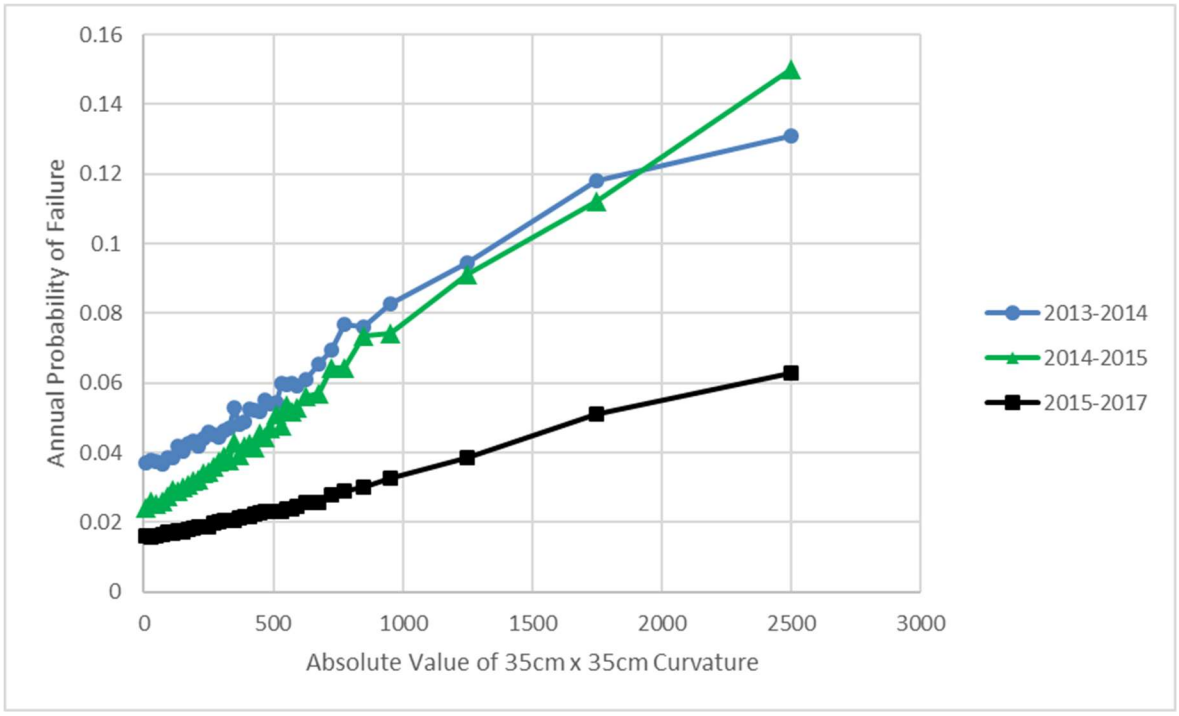

Figure 107. Annual probability of failure given the absolute value of 35cm x 35cm curvature for all change epochs, omitting data shallower than 45 degrees from horizontal

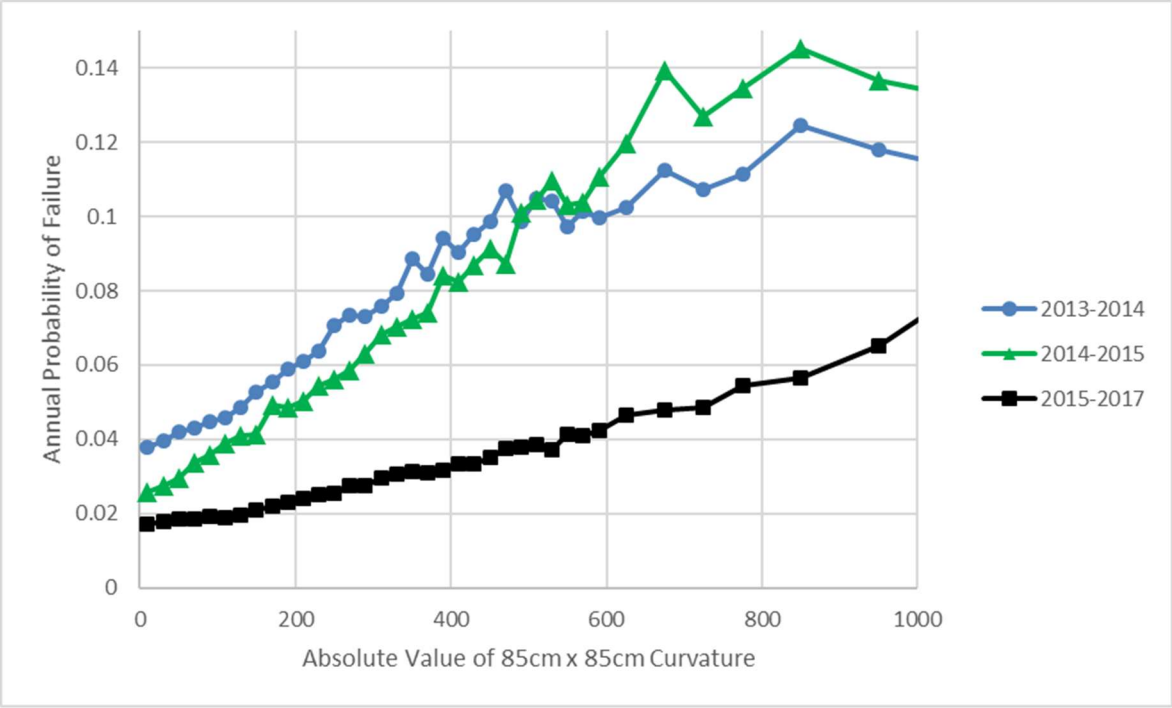

Figure 108. Annual probability of failure given the absolute value of 85cm x 85cm curvature for all change epochs, omitting data shallower than 45 degrees from horizontal

The linearity of Annual Probability of Failure vs Absolute Value of Curvature is again evident, as with the correlation between failure probability and roughness. Again, at the extreme ends of the curvature scale, the relationship degrades, due to those values being associated with edge effects and lower quality data.

3.4 Correlation between Curvature and Failure Size

This thesis also strives to determine the efficacy of using curvature to predict failure volumes. The same Probability of Failure vs Curvature plots are presented below (in Figures 109 and 110), for different depths of failure. The failure depths are color coded in these plots, from shallow (cold) to deep (hot).

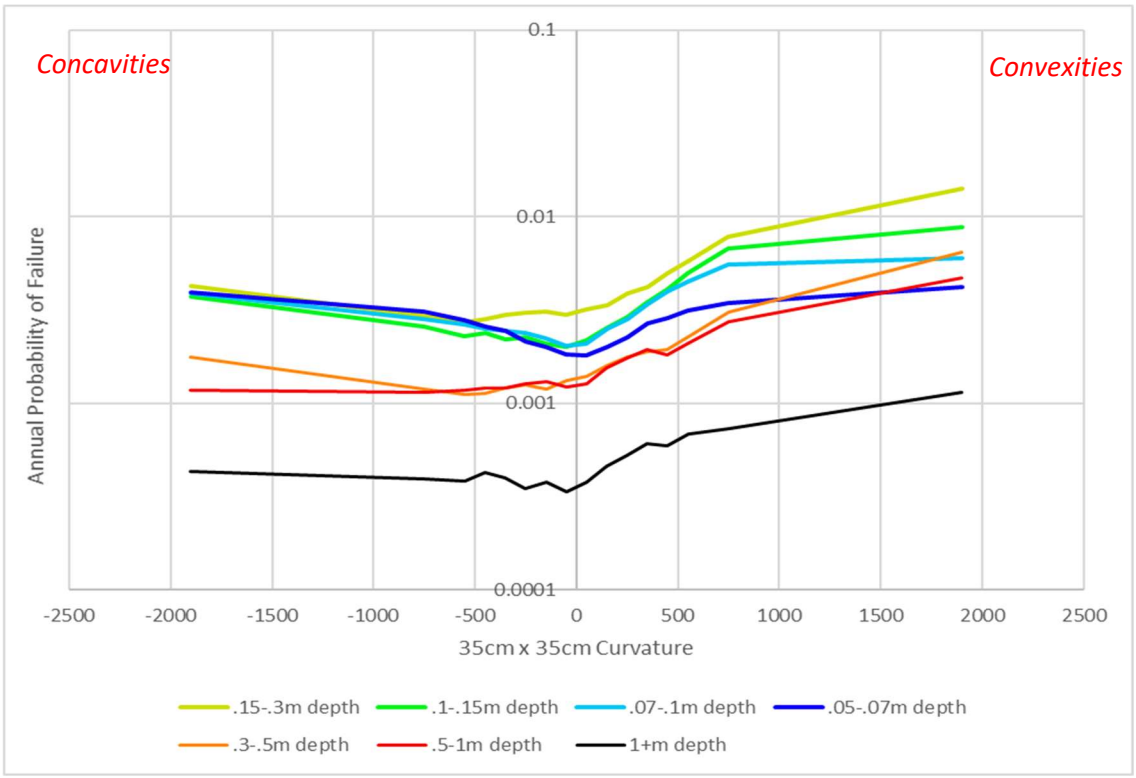

Figure 109. Annual probability of failure given 35cm x 35cm curvature, for all change epochs, to certain failure depths (coded by color). Data shallower than 45 degrees from horizontal is omitted.

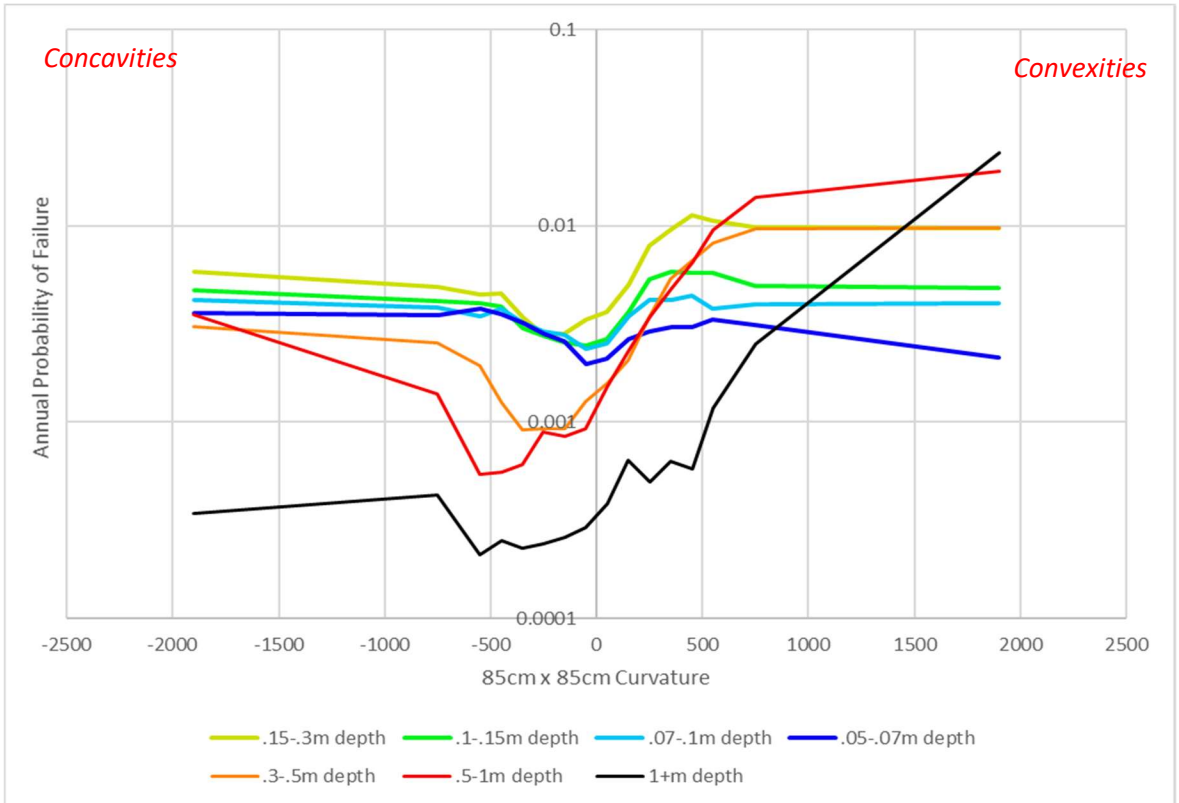

Figure 110. Annual probability of failure given 85cm x 85cm curvature, for all change epochs, to certain failure depths (coded by color). Data shallower than 45 degrees from horizontal is omitted.

The plots here are very different. For the smaller window size, probability of failure grades with curvature moderately, and evenly across the failure depth ranges. For the larger window size, probability of failure grades with curvature generally steeply, and much steeper for deeper failures. This shows that larger-scale convexities statistically predict larger-scale failures, and smaller-scale convexities statistically predict (to a smaller extent) all failure size ranges. Furthermore, small- and large-scale concavities both statistically predict small-scale failures. Figures 111 and 112, below, show magnitude-frequency curves for different curvature bins, for the two investigated curvature windows.

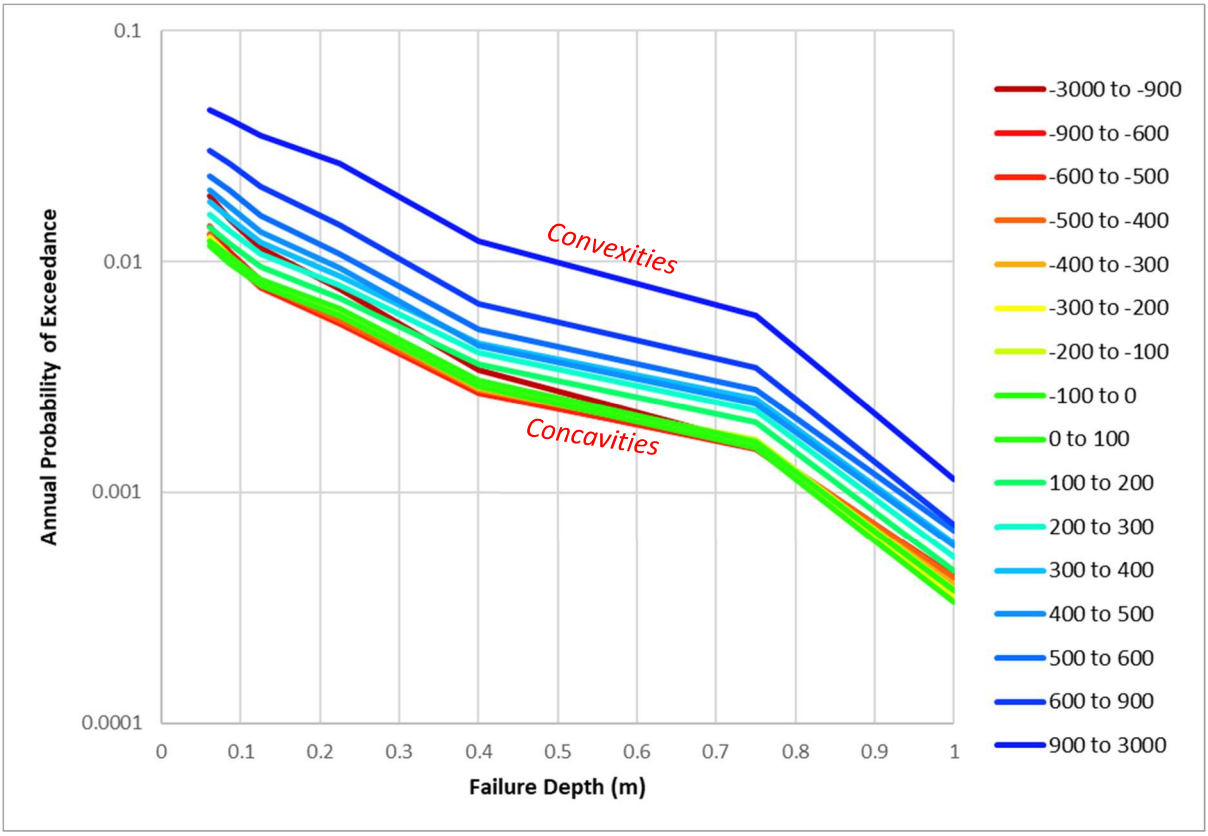

Figure 111. Size-frequency distributions describing annual probability of exceedance of certain failure depths, for given curvature values, measured in a 35cm x 35cm window. Data shallower than 45 degrees from horizontal is omitted.

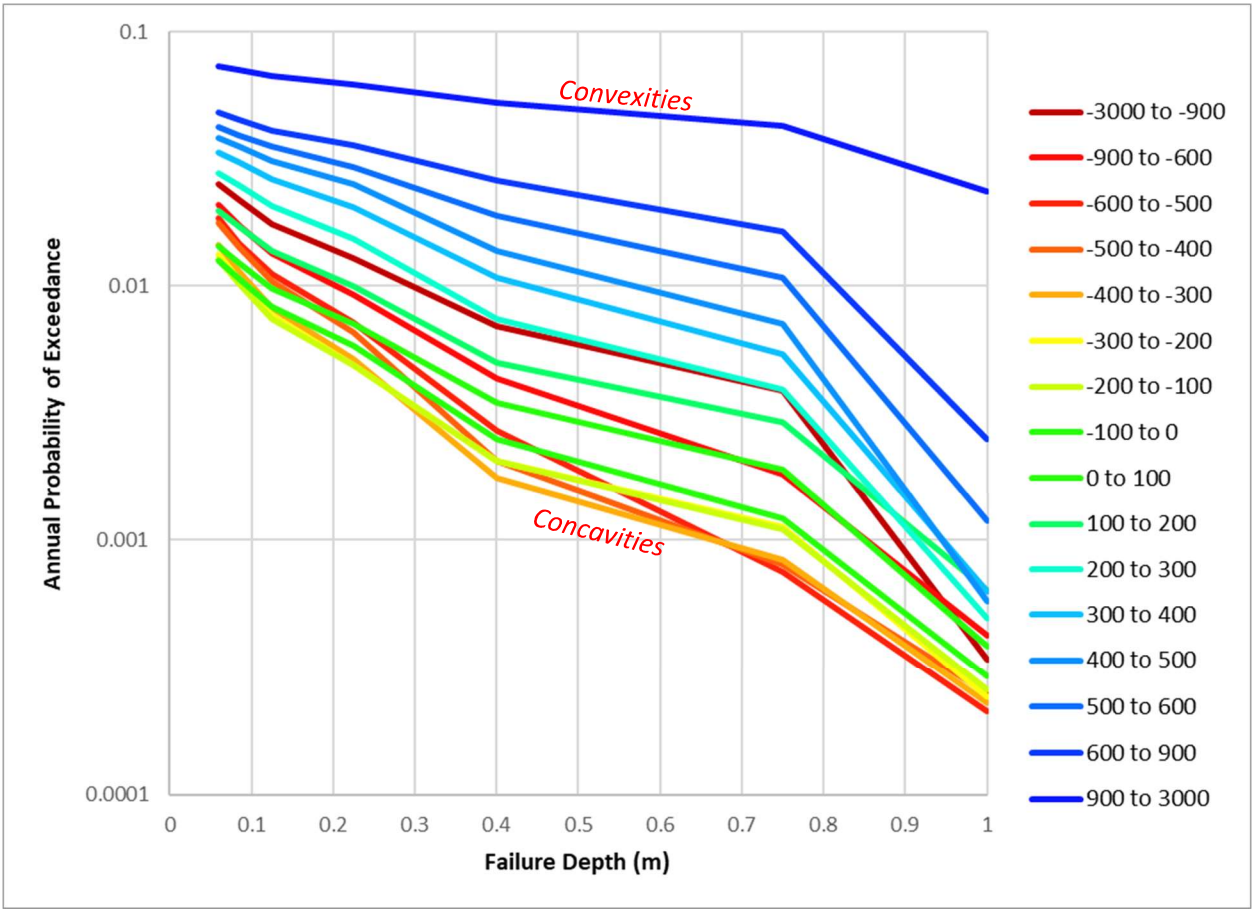

Figure 112. Size-frequency distributions describing annual probability of exceedance of certain failure depths, for given curvature values, measured in an 85cm x 85cm window. Data shallower than 45 degrees from horizontal is omitted.

These two plots reiterate the ability of curvature window size to predict failure size. The 35cm x 35cm curvature size-frequency distributions are generally parallel, meaning large failures scale similarly to small failures across the curvature domain. The 85cm x 85cm curvature size-frequency distributions are very non-parallel. Highly convex surfaces tend to have a higher rate of deep failures compared to planar or highly concave surfaces in this scale.

3.5 Summary of Efficacy of Point Cloud Parameters in Forecasting Failure

Feature Description	35cm x 35cm Curvature Output	85cm x 85cm Curvature Output	35cm x 35cm Roughness Output	85cm x 85cm Roughness Output	Likelihood of Small Failures	Likelihood of Large Failures
Concavities						
Small-Scale Concavity	- -	-	+ +	+	Low	Very Low
Large-Scale Concavity	-	- -	+	+ +	Medium	Low
Convexities						
Small-Scale Convexity	+ +	+	+ +	+	High	High
Large-Scale Convexity	+	+ +	+	+ +	Medium	Very High
Other						
Planar Slopes	0	0	0	0	Very Low	Very Low

Table 20. Results of the Curvature and Roughness study.

Table 20, above, lists the general output (in terms of very negative, negative, near 0, positive, and very positive) for the different point cloud parameters, and the associated likelihood of failures, for different feature types. Since concavities and convexities are identified as having similar roughnesses, the lesser-active concavities cannot be differentiated from the more-active convexities. Furthermore, the distribution of failure sizes is less discernable with roughness, because failure size is shown to relate to concavity scale differently than convexity scale.

The RAI System, overall, seems to be classifying the slope by geomorphologic processes fairly well using roughness. There is a discernible difference in failure probability and failure scale between RAI Classes (See Section 5). However, curvature is better able to identify individual features that are specifically susceptible to failure. Curvature is too specific to be useful as a parameter with which to classify slope areas, but could be implemented to identify specific features readily susceptible to failure. Visual inspection of the point clouds also indicates that curvature over even larger window sizes may be applicable to identifying areas with the potential to fail larger still.

4. Morphologic Evolution of Rock-Slopes

4.1 Spatial Distribution of Rock-Slope Failures

As is apparent in Figures 25 through 28, rockfall events are not uniformly distributed across the rock-slopes. Rather, the events appear to cluster together spatially, somewhat independently from their RAI classifications. Furthermore, the events appear to be concentrated towards the bottom of the slope. For this thesis, the spatial distribution of the elevation of events for each change epoch at Long Lake 71 was analyzed; the lateral distribution was not. Figure 113 shows a histogram of the distribution of elevations of failed cells.

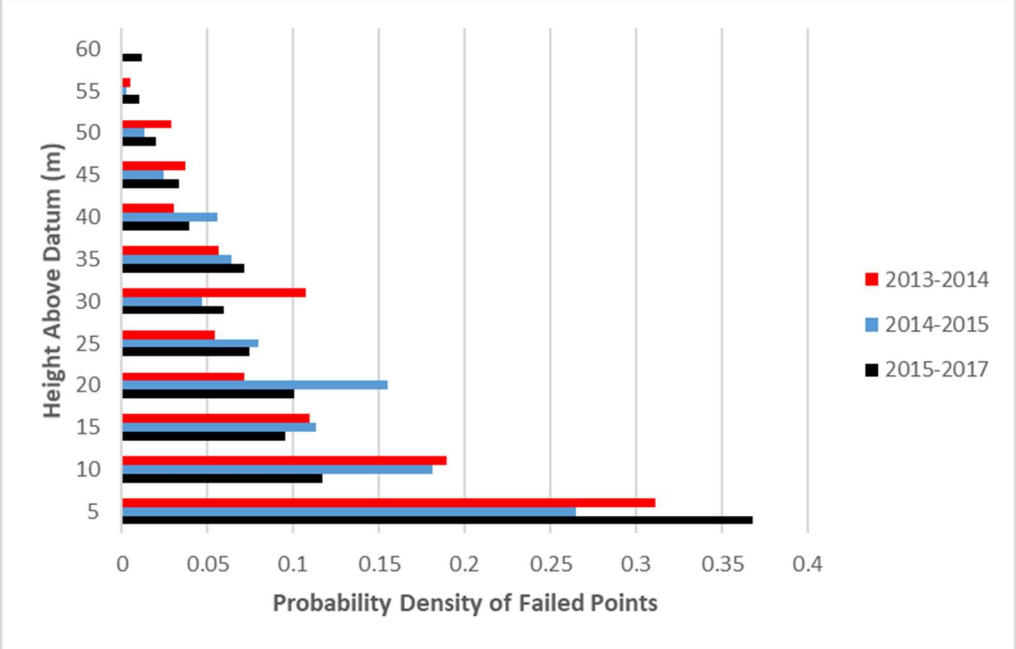

Figure 113. Spatial distribution of elevations of events at LL71, for the three change epochs.

The distribution of events is distinctively non-uniform in elevation. Failures are significantly more likely to occur at lower portions of the slope than at upper portions. This relationship holds true throughout the change epochs. The non-uniform spatial distribution of failure events should be investigated further to understand its contribution to mass-wasting processes at the rock-slopes.

4.2 Tendency of Failures to Overlap

An analysis was conducted to determine if past failure of an area of the slope face indicated increased likelihood of future failure. It was manually determined if the center-of-moment of each failure cluster resided inside a previous failure cluster at LL71, between the 2013-2014 and 2014-2015 epochs. Table 21 shows the results of this study.

RAI Class	% Slope Area Failed, 2013-2014	# of 2014-2015 Failures in Each RAI Class	# of 2014-2015 Failures Expected to Overlap	# of 2014-2015 Failures Actually Overlapped	% Of Expected Rate
Talus	22.2%	104	23.1	21	90.9%
Intact	2.2%	193	4.2	13	311.1%
10cm Disc	0.46%	101	0.47	5	1074.8%
20cm Disc	2.0%	333	6.7	59	876.7%
30cm Disc	2.0%	66	1.4	8	592.4%
Shallow Overhang	2.7%	145	3.9	15	387.9%
Steep Overhang	0.79%	9	0.07	0	0%
Total Slope Area	2.5%	958	24.3	121	497.3%

Table 21. Results of the Failure Overlap Study

Most RAI Classes show a tendency for failures to occur again where failures have occurred in the past. The discontinuous classes are particularly susceptible to this phenomenon. The Talus, however, sees the opposite effect. Failure in the Talus indicates areas that future failures are less likely.

Several factors may play in to this tendency. Firstly, rockfall events could instigate instability in the rock-mass, through stress release and the kinematic allowance of further failures. However, these results could also be skewed by the non-random spatial distributions of failures generally (see Section 4.1), and a tendency for failures to group near one another due to rock-mass-wasting processes not necessarily directly related to failures instigating other failures.

4.3 Evolution of RAI Class through Time

If slope recession rates are significantly different for different RAI Classes, RAI Class would need to change through time in order for the slope to maintain generally planar slope geometry. If failures occur in overhangs, for example, one would assume that the overhangs would eventually become less cantilevered, in an effort to maintain equilibrium. Contrarily, failures in intact rock could change the geometry of the rock to create overhanging or discontinuous areas. The proportion of each RAI Class comprising a site, as a function of time, is shown in Table 22 through Table 25, below.

LL85.5	2013	2014	2015	2017
Unclass.	0.1%	0.5%	0.0%	0.7%
Talus	1.9%	4.3%	5.1%	3.9%
Intact	4.5%	9.7%	3.4%	2.2%
10cm Disc	10.7%	10.3%	10.8%	10.5%
20cm Disc	47.2%	34.7%	38.3%	32.6%
30cm Disc	27.0%	26.8%	29.5%	36.1%
Shallow Overhang	7.8%	11.6%	11.4%	12.0%
Steep Overhang	0.7%	2.2%	1.5%	2.1%

Table 22. Proportion of LL85.5 Slope Comprised of Various RAI Classes

LL86.9	2013	2014	2015	2017
Unclass.	0.1%	N/A	0.0%	0.0%
Talus	8.3%	N/A	22.5%	18.8%
Intact	43.3%	N/A	36.1%	37.7%
10cm Disc	11.4%	N/A	10.0%	10.8%
20cm Disc	23.0%	N/A	19.5%	21.7%
30cm Disc	10.9%	N/A	8.2%	7.2%
Shallow Overhang	2.9%	N/A	3.5%	3.7%
Steep Overhang	0.1%	N/A	0.1%	0.2%

Table 23. Proportion of LL86.9 Comprised of Various RAI Classes

LL87	2013	2014	2015	2017
Unclass.	0.3%	0.3%	0.0%	0.0%
Talus	7.5%	7.2%	13.2%	11.1%
Intact	21.3%	24.7%	14.9%	15.5%
10cm Disc	14.4%	12.5%	12.4%	13.2%
20cm Disc	31.7%	25.6%	28.7%	27.1%
30cm Disc	15.1%	16.6%	18.5%	19.6%
Shallow Overhang	8.6%	10.4%	9.9%	10.5%
Steep Overhang	1.1%	2.8%	2.5%	3.0%

Table 24. Proportion of LL87 Slope Comprised of Various RAI Classes

LL71	2013	2014	2015	2017
Unclass.	0.0%	0.0%	0.0%	0.0%
Talus	3.5%	5.2%	3.5%	2.9%
Intact	30.1%	34.9%	39.0%	35.7%
10cm Disc	12.1%	12.1%	12.3%	10.9%
20cm Disc	23.4%	21.4%	20.8%	17.5%
30cm Disc	11.0%	8.8%	7.6%	12.2%
Shallow Overhang	17.4%	15.8%	15.1%	16.9%
Steep Overhang	2.6%	1.9%	1.8%	3.9%

Table 25. Proportion of the LL71 Slope Comprised of Various RAI Classes

Minor fluctuations in the proportion of RAI Classes are present from year-to-year at each site, but they stay generally consistent. These fluctuations could truly be caused by geomorphologic processes, but they may also be caused by changes in scan resolution from year to year.

5. Assessment of the RAI Assumed Failure Parameters

In Dunham *et al.* (2017), the authors suggested assigning a single rate of failure, r, and a single expected failure depth, D, for points of the specific RAI Classes. This study aims to investigate both the effectiveness of that methodology, and the chosen rates, to determine whether or not modifications to the RAI system need to be made. Below, in Table 26**,** average and standard deviations of Failure Rate and Failure Depths between all sites and epochs are presented. Table 27 shows average values for Failure Rate and Failure Depths weighted by site area. Raw data for these rates, for all sites and epochs, can be found in Appendix C. Also, in Figures 114 and 115, box-and-whisker plots of these results, for all sites and change epochs, are presented. In the plots, the assumed values from Dunham *et al.* (2017) are shown in yellow. 2015-2017 data was weighted more heavily in the calculation of averages, due to it covering two years of change.

RAI Class	Average Rate, r	σ of Rate, r	CoV of r	Rate Prediction, r	Average Depth, D (m)	σ of Depth, D	CoV of D	Depth Assumption, D
Unclass.	.0264	0.0532	1.511	0.000125	-0.119	0.0688	0.578	-0.025
Talus	0.122	0.121	0.776	0.000125	-0.102	0.0483	0.474	-0.025
Intact	0.0466	0.0201	0.466	0.000125	-0.105	0.0581	0.553	-0.05
10cm Disc	0.0454	0.0401	0.623	0.002030	-0.124	0.0464	0.374	-0.10
20cm Disc	0.0449	0.0353	0.557	0.004600	-0.126	0.0468	0.371	-0.20
30cm Disc	0.0316	0.0217	0.531	0.009980	-0.162	0.0639	0.394	-0.30
Shallow Overhang	0.0330	0.0442	1.091	0.029410	-0.149	0.0528	0.354	-0.50
Steep Overhang	0.0406	0.0631	1.360	0.039210	-0.206	0.0562	0.273	-0.75

Table 26. Failure Rates and Depths averaged across the sites, for all sites and epochs, 2012-2013 data omitted.

RAI Class	Weighted Average Failure Rate, r	Weighted Average Failure Depth, D (m)
Unclass.	0.0326	0.1452
Talus	0.1290	0.1240
Intact	0.0234	0.1704
10cm Disc	0.0306	0.1724
20cm Disc	0.0334	0.1702
30cm Disc	0.0295	0.2169
Shallow Overhang	0.0228	0.2125
Steep Overhang	0.0362	0.2316

Table 27. Failure Rates and Depths averaged across the sites, for all sites and epochs, 2012-2013 data omitted, weighted by site area.

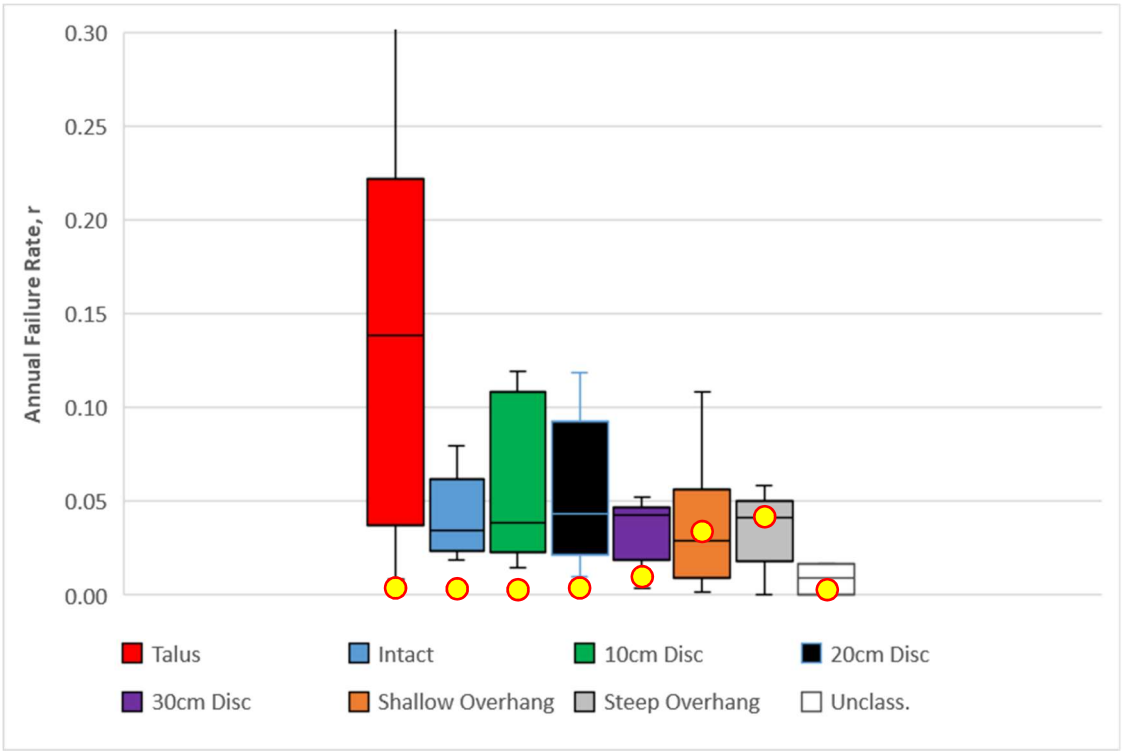

Figure 114. Box-and-whisker plot of annual failure rate of cells, across all sites and years (omitting 2012-2013 data).

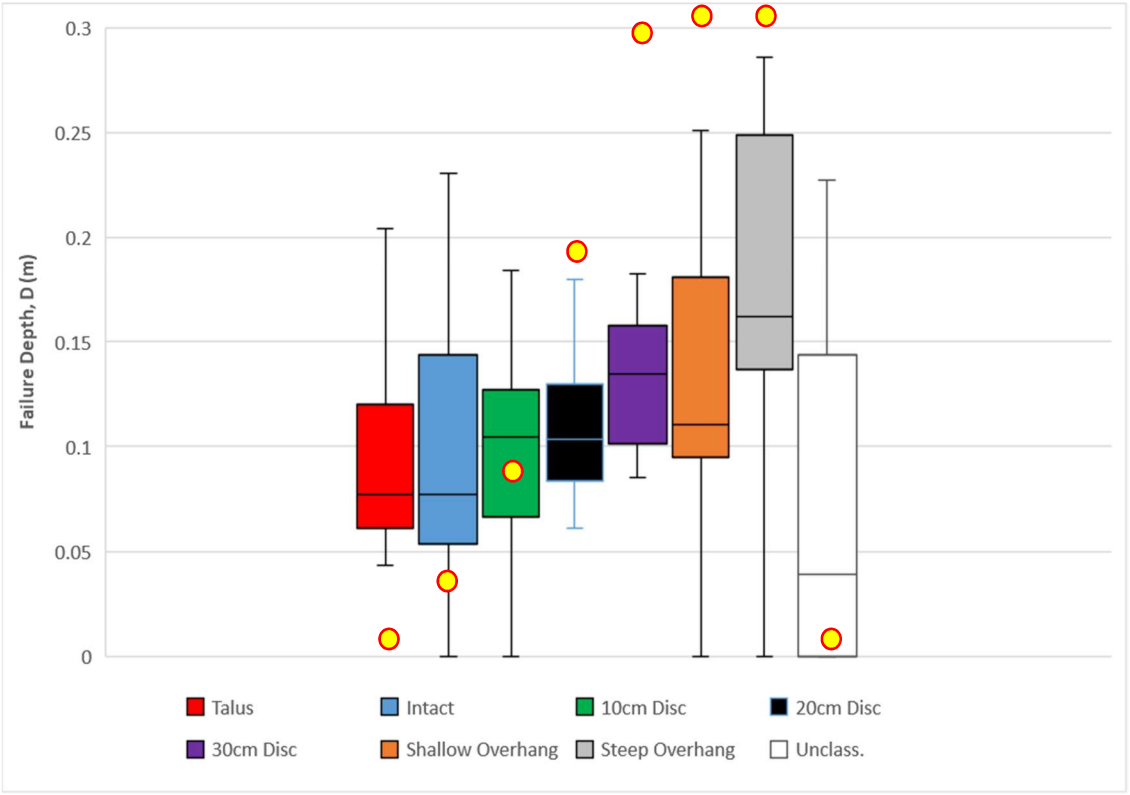

Figure 115. Box-and-whisker plot of average failure depth of failed cells, across all sites and years (omitting 2012-2013 data).

Failure rates and depths are slightly distinct between RAI Classes, but less distinct than the size-frequency parameters previously investigated. The data shows, however, that failure rate is being underestimated across all RAI Classes, and failure depth is being underestimated for Unclassified areas, Talus areas, Intact areas, and 10cm Spaced Discontinuities, but overestimated for 20cm Spaced Discontinuities, 30cm Spaced Discontinuities, Shallow Overhangs, and Steep Overhangs.

The assumed rates and depths (and areal representation of each point) are also used to estimate an expected Kinetic Energy Release (also known as the RAI Score) to the roadway, based on the height of the point in question, per the following equation (Dunham *et al.*, 2017):

$$KE = \frac{1}{2} M V^2$$

Where V is Velocity and M is Mass.

The mass is calculated as follows:

$$M = A * D * SG * \rho_{water}$$

Where
A is the area representation of each grid point
D is the annual expected depth of failure
SG is the Specific Gravity of rock (assumed as 2.70)
ρ_{water} is the density of water (assumed as 1000 kg / m^3).

The velocity is calculated as follows:

$$V = \sqrt{(2 * g * h)}$$

Where g is the acceleration due to gravity and h is the height of the point above the road surface.

Table 28**,** below, gives average and standard deviation of output Kinetic Energy release to the road surface, and the originally-predicted Kinetic Energy Release for the sites, over all change epochs (omitting 2012-2013). Figures 116 through 119 show bar charts of these Kinetic Energy Release outputs for each site, with the prediction values shown in orange. Note that this plot is on a logarithmic y-axis, so slight differences in the plot may be orders of magnitude of difference in reality.

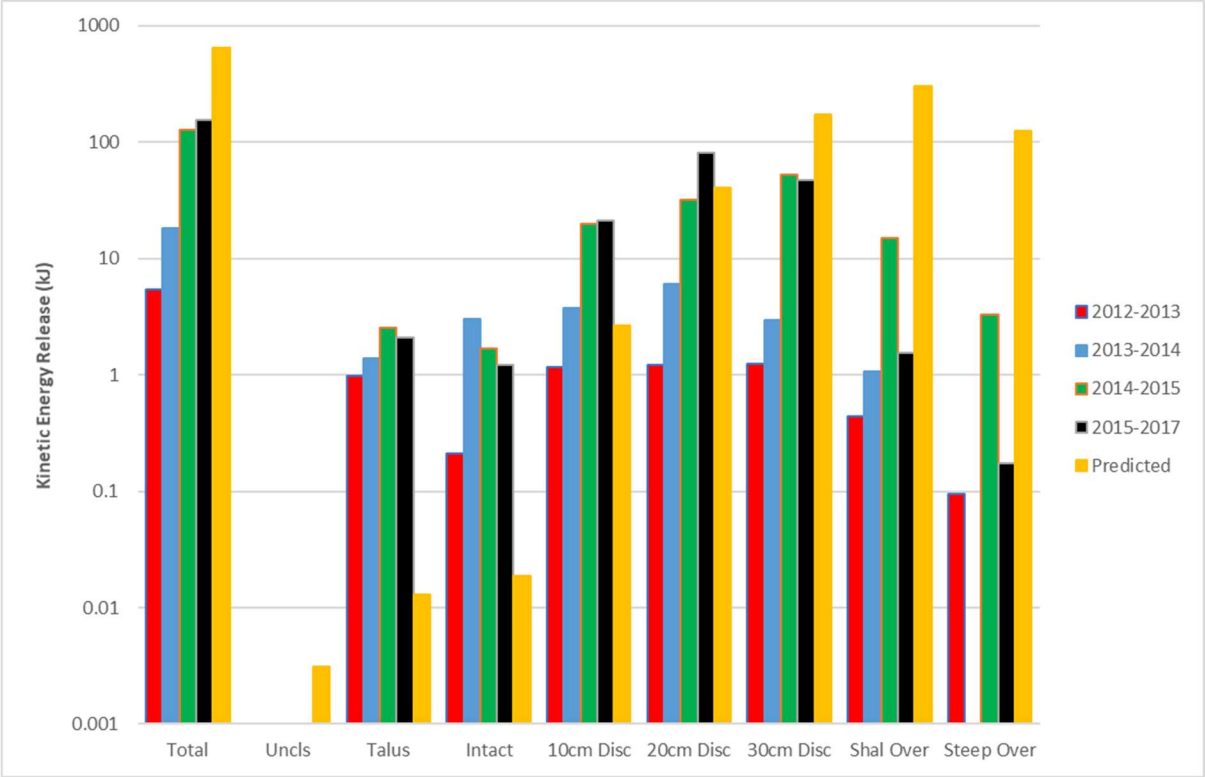

Figure 116. Annual Kinetic Energy Release and Predictions (in kJ) for Each RAI Class, for each Change Epoch, at LL85.5

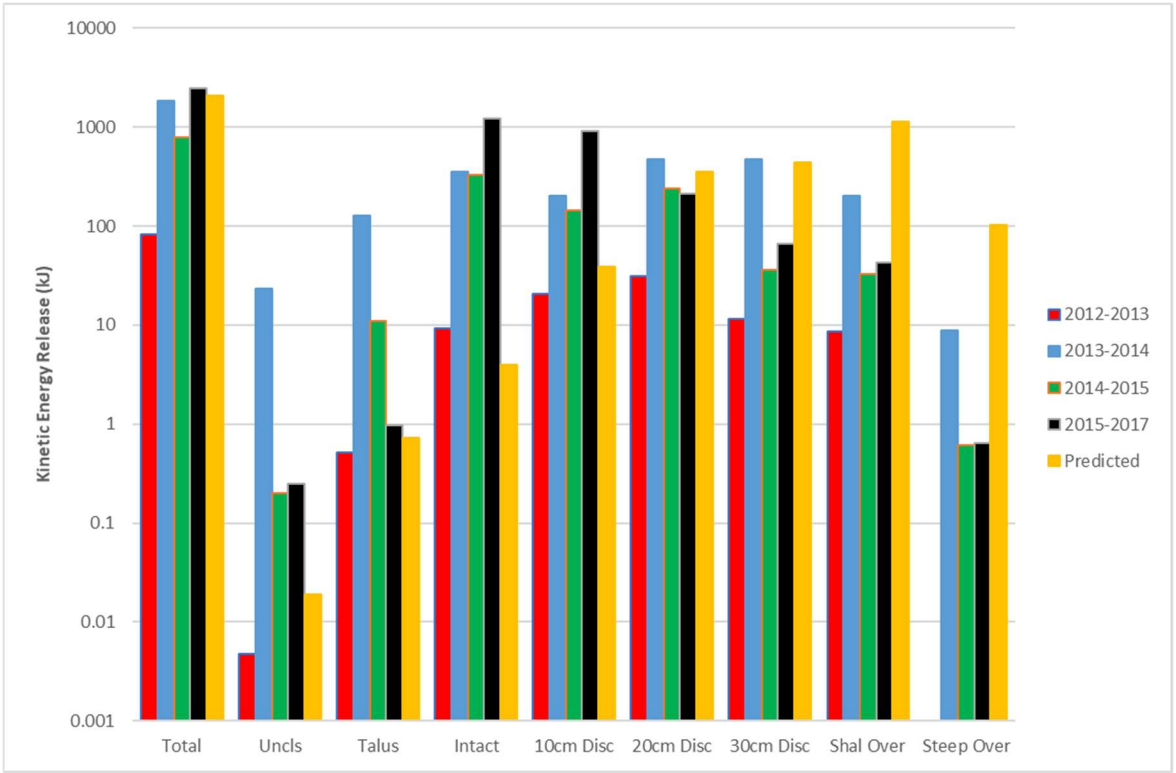

Figure 117. Annual Kinetic Energy Release and Predictions (in kJ) for Each RAI Class, for each Change Epoch, at LL86.9

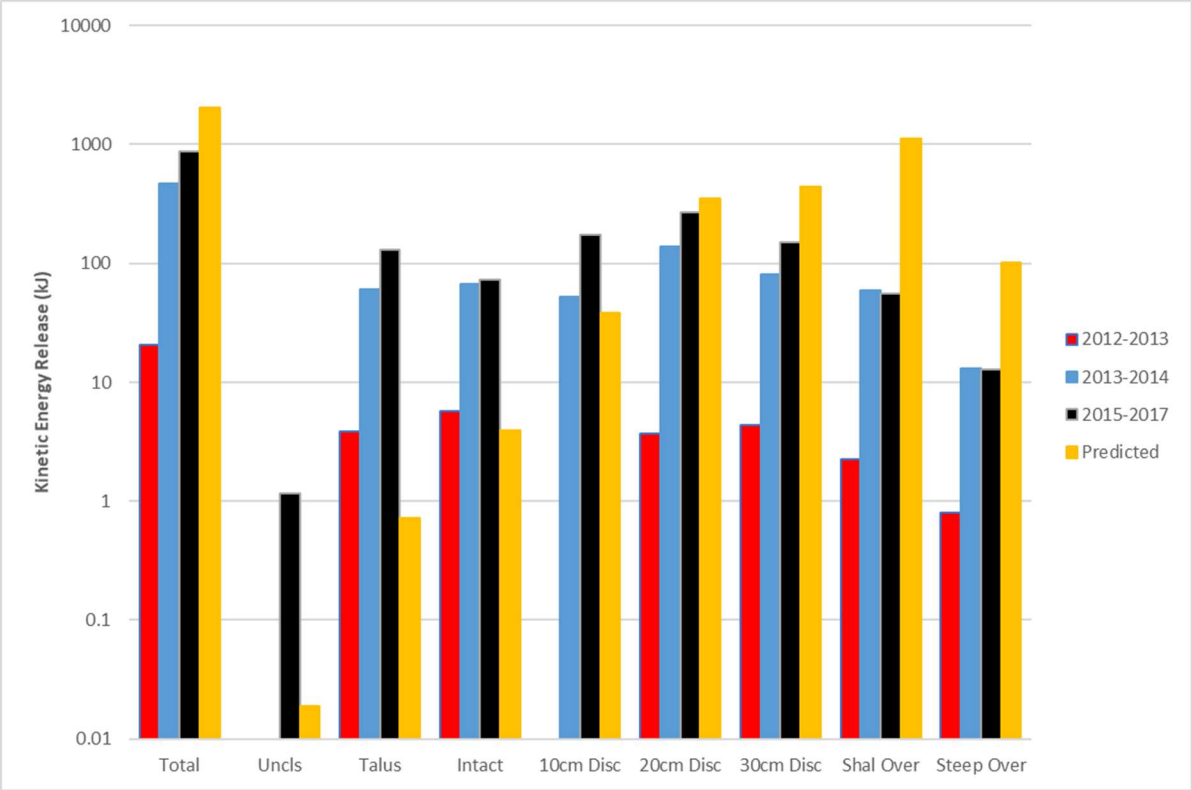

Figure 118. Annual Kinetic Energy Release and Predictions (in kJ) for Each RAI Class, for each Change Epoch, at LL87

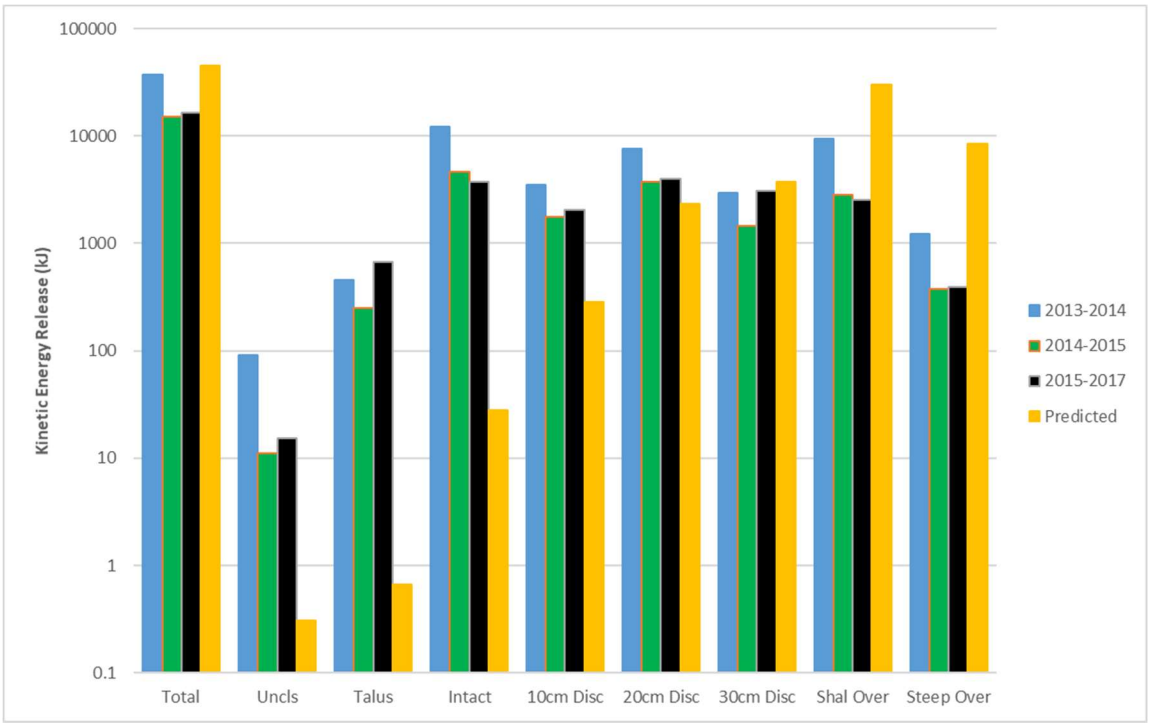

Figure 119. Annual Kinetic Energy Release and Predictions (in kJ) for Each RAI Class, for each Change Epoch, at LL71

	LL85.5			LL86.9			LL87			LL71		
RAI Class	**Avg KE (kJ)**	**σ of KE (kJ)**	**Pred KE (kJ)**	**Avg KE (kJ)**	**σ of KE (kJ)**	**Pred KE (kJ)**	**Avg KE (kJ)**	**σ of KE (kJ)**	**Pred KE (kJ)**	**Avg KE (kJ)**	**σ of KE (kJ)**	**Pred KE (kJ)**
Total	114.3	59.28	647.8	1893	690.4	2060	733.8	197.5	1516	21323	10159	44790
Uncl.	0.00	0.000	0.003	6.06	10.99	0.019	0.773	0.580	0.001	32.98	36.39	0.31
Talus	2.03	0.467	0.013	35.43	58.06	0.716	107.2	34.66	0.095	510.2	170.2	0.67
Intact	1.79	0.755	0.019	779.2	414.4	3.94	71.03	3.17	0.433	6064	3778	27.77
10cm Disc	16.52	7.92	2.65	546.5	352.7	38.48	132.5	60.25	11.34	2339	757.7	283.3
20cm Disc	50.37	31.39	41.05	284.0	116.3	350.2	225.1	65.69	108.4	4822	1735	2325
30cm Disc	37.87	22.49	173.1	159.3	197.0	441.0	127.7	35.18	277.3	2630	724.7	3773
Shall Over	4.80	6.45	305.9	80.14	77.54	1124	56.50	1.79	735.8	4330	3149	29921
Steep Over	0.903	1.500	125.0	2.66	3.84	101.6	12.93	0.194	389.6	595.0	394.0	

Table 28. Average Observed Kinetic Energy Release vs Predicted Kinetic Energy Release

The predictions of Kinetic Energy Release across the entire site have been generally in-line with observed values, especially in more recent data. However, as seen in the deaggregation of the Kinetic Energy Release by RAI Class, this parameter is being substantially over-predicted in 30cm-Disc, Shallow Overhang, and the Steep Overhang Classes, and generally under-predicted in the Unclassified, Talus, Intact, 10cm-Disc, and 20cm-Disc Classes, leading to the relatively accurate predictions of total Kinetic Energy Release.

6. Suggested Modifications to the Rockfall Activity Index

6.1 Adjustments of the Average Failure Rate and Assumed Failure Depth

As discussed in Section 1.5, the RAI methodology is currently using Average Failure Rates, r, and Average Failure Depths, D, that are unrepresentative of observed behavior at these investigated rock-slopes. Table 29 contains recommended modifications for Average Failure Rate, r, Assumed Failure Depth, D for the various RAI Classifications. These values are the point failure rate observed at the four Long Lake study sites between 2012-2017, and the average depth of failure for the same data set.

RAI Class	Current Failure Rate, r	Modified Failure Rate, r	Current Assumed Depth, D	Modified Assumed Depth, D
Unclass.	0.000125	0.0326	0.025	0.1452
Talus	0.000125	0.129	0.025	0.1240
Intact	0.000125	0.0234	0.05	0.1704
10cm Disc	0.002030	0.0306	0.10	0.1724
20cm Disc	0.004600	0.0334	0.20	0.1702
30cm Disc	0.009980	0.0295	0.30	0.2169
Shallow Overhang	0.029410	0.0228	0.50	0.2125
Steep Overhang	0.039210	0.0362	0.75	0.2316

Table 29. Modified Average Failure Rates and Assumed Failure Depths for the RAI System

6.2 Utilizing Size-Frequency Parameters instead of Failure Rate and Depth

Providing an average failure rate and failure depth oversimplifies the distribution of failure events that may occur within the distinct RAI Classes. Mass-wasting behavior within the RAI Classes could instead be better represented by implementing size-frequency parameters into the RAI methodology. Assigning each point on the slope face an Activity Parameter, β, and Scaling Parameter, α, instead of simple failure depth and rate, would better represent the behavior of the rock-slope in the forward projection models. Users could then study the relative severity of events that may occur within distinct RAI Classes, which could be beneficial when planning rockfall hazard mitigation strategies.

6.3 Utilizing Curvature as a Hazard Modeling Parameter

As described in Sections 3.3 and 3.4, curvature has a demonstrable ability to locate specific features susceptible to failure. Furthermore, curvature window size is indicative of the feature size, and therefore can be correlated to the subsequent failure size. It is likely that larger curvature windows not considered in this study would continue experiencing this trend, and would be correlated to the likelihood of even larger failure events occurring. Both curvature and roughness for a portion of LL71 are shown in Figures 120 and 121, below.

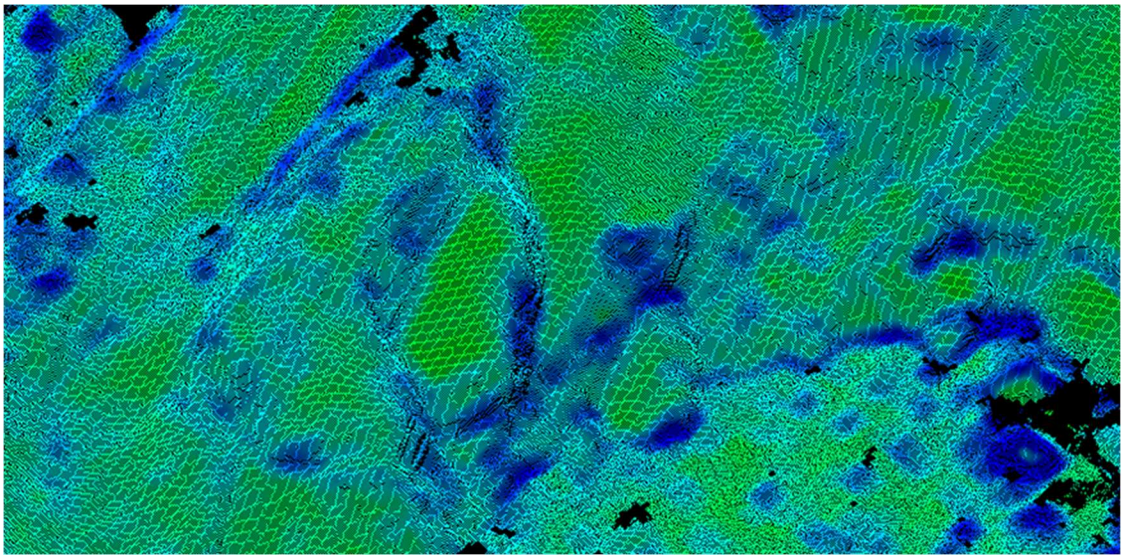

Figure 120. 85cm Roughness for a portion of the LL71 site. Green indicates smoother areas, blue indicates rougher areas.

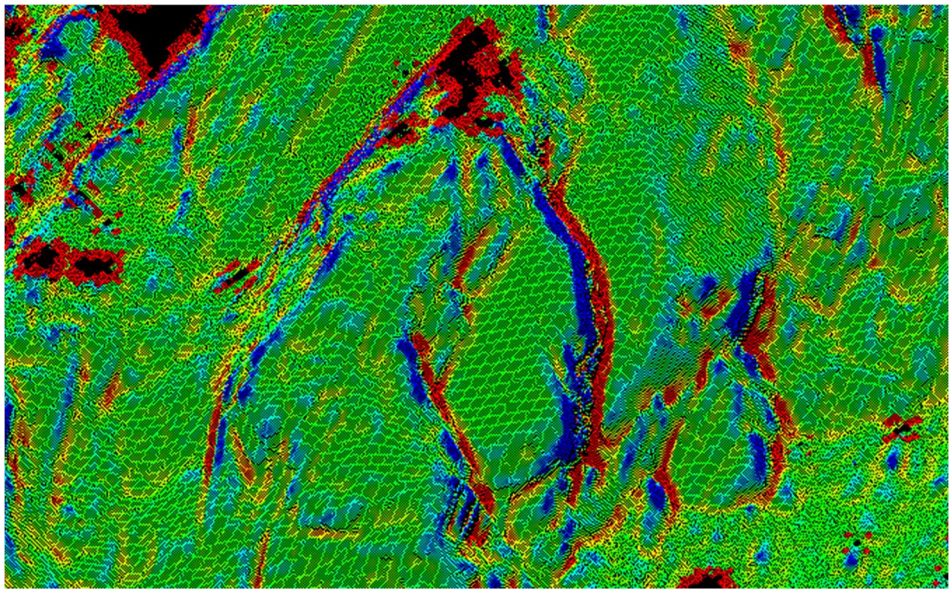

Figure 121. 85cm Curvature for a portion of the LL71 site. Green indicates planar areas, red indicates concavities, and blue indicates convexities.

As seen in the above figures, classifying slope areas by curvature results in choppy, discontinuous process mapping. Furthermore, roughness has shown to adequately differentiate between areas with different mass-wasting processes. Curvature could be implemented as a multiplier,

able to identify specific features susceptible to failure, if finer resolution of hazard mapping is desired, but roughness differentiates the slope mass-wasting processes significantly well as is.

6.4 Adjustment of the Talus Slope Angle

During observations of RAI classification of failure events, it was noted that some events on some sites were errantly classified as occurring in Intact Rock when they actually occurred in Talus. Upon further investigation, we noted that talus slopes were standing steeper than expected at some sites, and the maximum talus angle of 35^{o} presented by Dunham *et al.* (2017) is mis-classifying some slope areas. We measured talus slope angles using Maptek I-Site Studio Strike and Dip Query. The histogram of the angle of talus slopes LL86.9, LL87, and LL71 is presented in Figure 122, below, as measured in the 2015 point clouds. LL85.5 does not have a significant amount of talus and was omitted from this study.

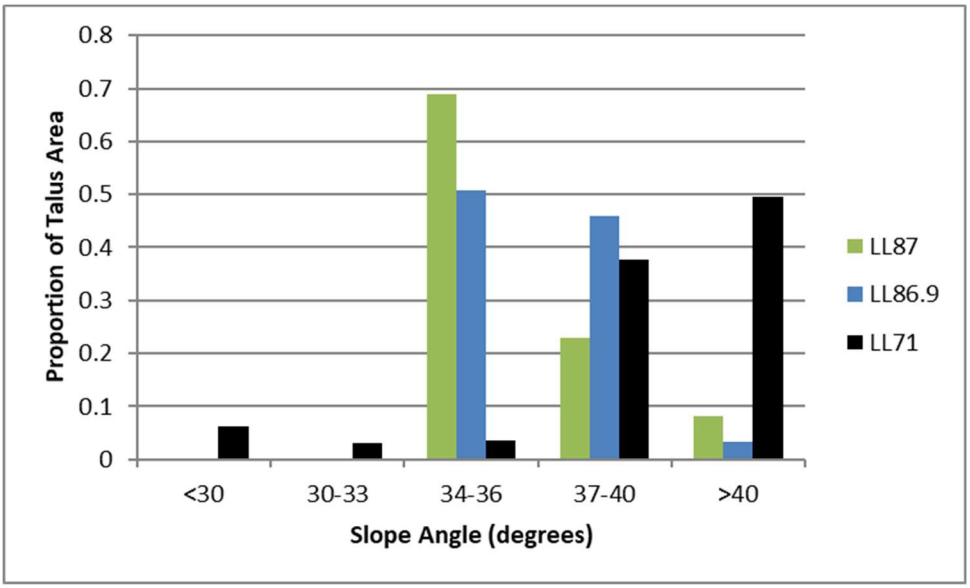

Figure 122. Histogram of Talus Slope Angle for LL87, LL86.9, and LL71

It should be noted that our measured talus slopes at Long Lake 71 are significantly steeper than average natural talus slope angles reported in literature. For example, Carson (1977), Sæter (2008), Katsube and Oguchi (1999) all list a typical well-drained talus slope angle of about 35^{o}. Notably, this is far lower than the angle of repose and effective friction angle of fragmented rock, which is typically highly angular and very coarse-grained. Chandler (1973) suggests that the discrepancy between natural talus slope angles and the effective friction angle may be due to the dynamic, high-energy deposition mode of talus materials. Chandler (1973) reports typical effective friction angles of highly angular rock fragments in excess of 39^{o} in a loose condition, and as high as 55^{o} when densely configured.

It has also been shown that talus slopes incurring toe erosion by river or wave action stand systematically steeper than slopes without toe erosion, and typically approach the effective friction angle. Suspended talus slopes tend to stand slightly steeper than other talus slopes as well. The talus slopes at the study sites are likely being undercut by maintenance activity at their toes, allowing the slope angles to approach the loose friction angle of the angular rock fragments, which could be at least 39^{o}. Also, some talus slopes at the sites are suspended, so their slope angle would stand steeper than 35^{o}.

To properly classify the talus slopes and differentiate between them and intact rock for rock-slope hazard assessment, a variable intact/talus slope threshold may be necessary. The user could investigate the point clouds at a particular site, find a maximum talus slope angle for the area, and adjust the talus slope threshold accordingly. Below, in Figures 123 and 124, the RAI classification at Long Lake 71 is shown with a talus slope threshold of 35 degrees and 42 degrees. The important distinction should be made between green (intact) and blue (talus).

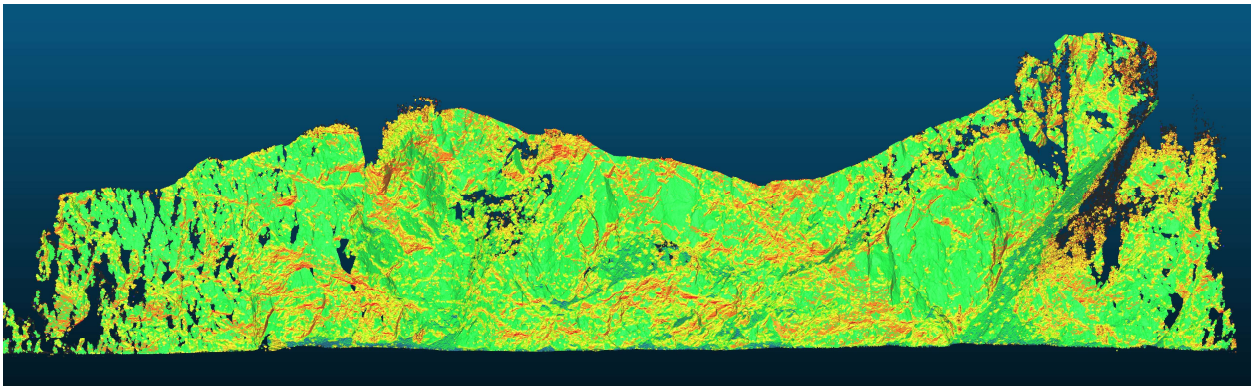

Figure 123. RAI Classification at LL71 with a Talus Slope Threshold of 35 degrees. Green is Intact and Blue is Talus.

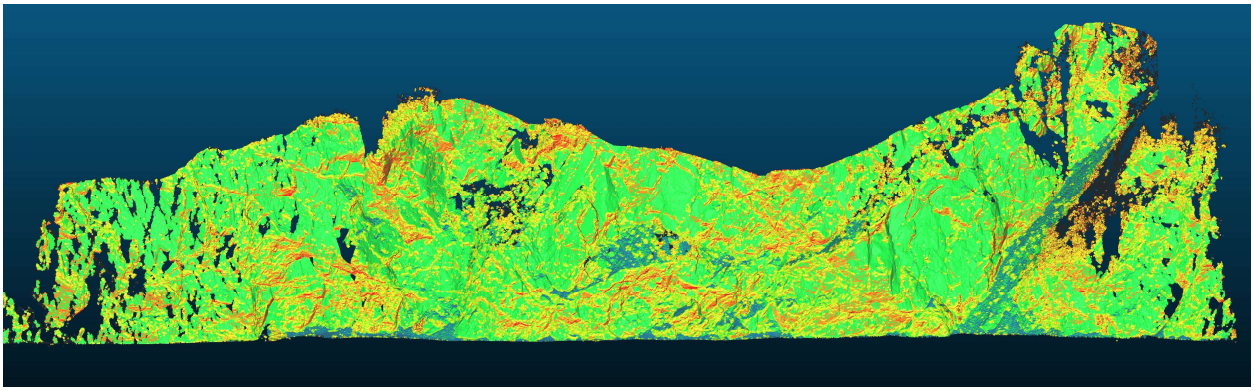

Figure 124. RAI Classification at LL71 with a Talus Slope Threshold of 42 degrees. Green is Intact and Blue is Talus.

The modified Talus Slope Threshold appears to identify talus areas more properly than the original 35^{o} threshold.

6.5 Results of Modifications to the RAI Methodology

The Rockfall Activity Index algorithm was tested with new Failure Rates and Assumed Depths, and a new talus slope angle of 42^{o}, at all sites. The average observed Kinetic Energy Release, along with the Kinetic Energy Release prediction using old and new rate and depth parameters, are seen in Figures 125 through 128, and Table 30, below. Images of the point clouds colored by expected Kinetic Energy Release are given in Appendix D, with both the old and new RAI parameters.

	LL85.5			LL86.9			LL87			LL71		
RAI Class	Avg KE (kJ)	Old KE (kJ)	New KE (kJ)	Avg KE (kJ)	Old KE (kJ)	New KE (kJ)	Avg KE (kJ)	Old KE (kJ)	New KE (kJ)	Avg KE (kJ)	Old KE (kJ)	New KE (kJ)
Total	114.3	647.8	1448	1893	2060	6625	733.8	1516	2768	21323	44790	66365
Uncl.	0.00	0.003	0	6.06	0.019	8	0.773	0.001	0.86	32.98	0.31	418
Talus	2.03	0.013	87	35.43	0.716	2797	107.2	0.095	645	510.2	0.67	3995
Intact	1.79	0.019	14	779.2	3.94	1237	71.03	0.433	263	6064	27.77	15502
10cm Disc	16.52	2.65	88	546.5	38.5	469	132.5	11.34	306	2339	283.3	6480
20cm Disc	50.37	41.05	297.2	284.0	350.2	955	225.1	108.4	666	4822	2325	11848
30cm Disc	37.87	173.1	705	159.3	441.0	903	127.7	277.3	539	2630	3773	13837
Shall Over	4.80	305.9	176	80.14	1124	239	56.50	735.8	243	4330	29921	9907
Steep Over	0.903	125.0	80	2.66	101.6	17	12.93	389.6	107	595.0	8669	4377

Table 30. Kinetic Energy Release (kJ) vs KE Expected (old parameters) vs KE Expected (new parameters)

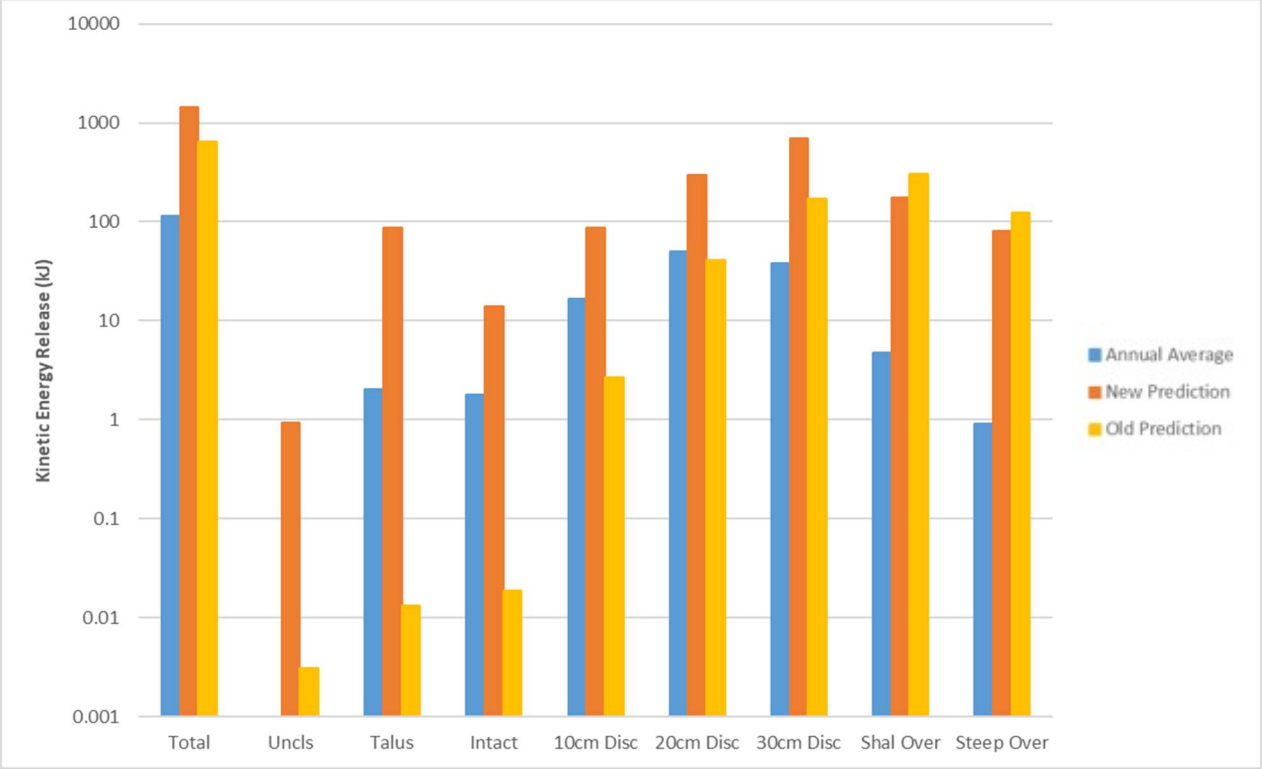

Figure 125. Annual Kinetic Energy Release (average) and KE Prediction using Original and Modified Parameters, LL85.5

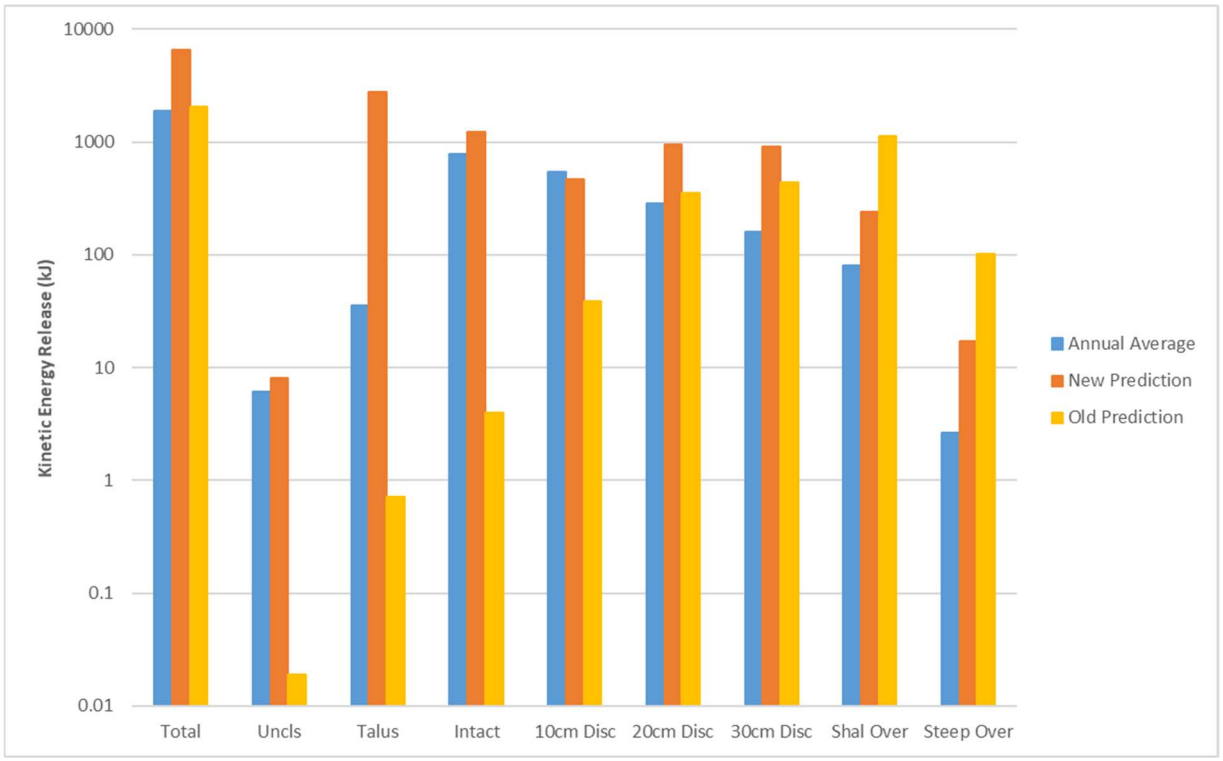

Figure 126. Annual Kinetic Energy Release (average) and KE Prediction using Original and Modified Parameters, LL86.9

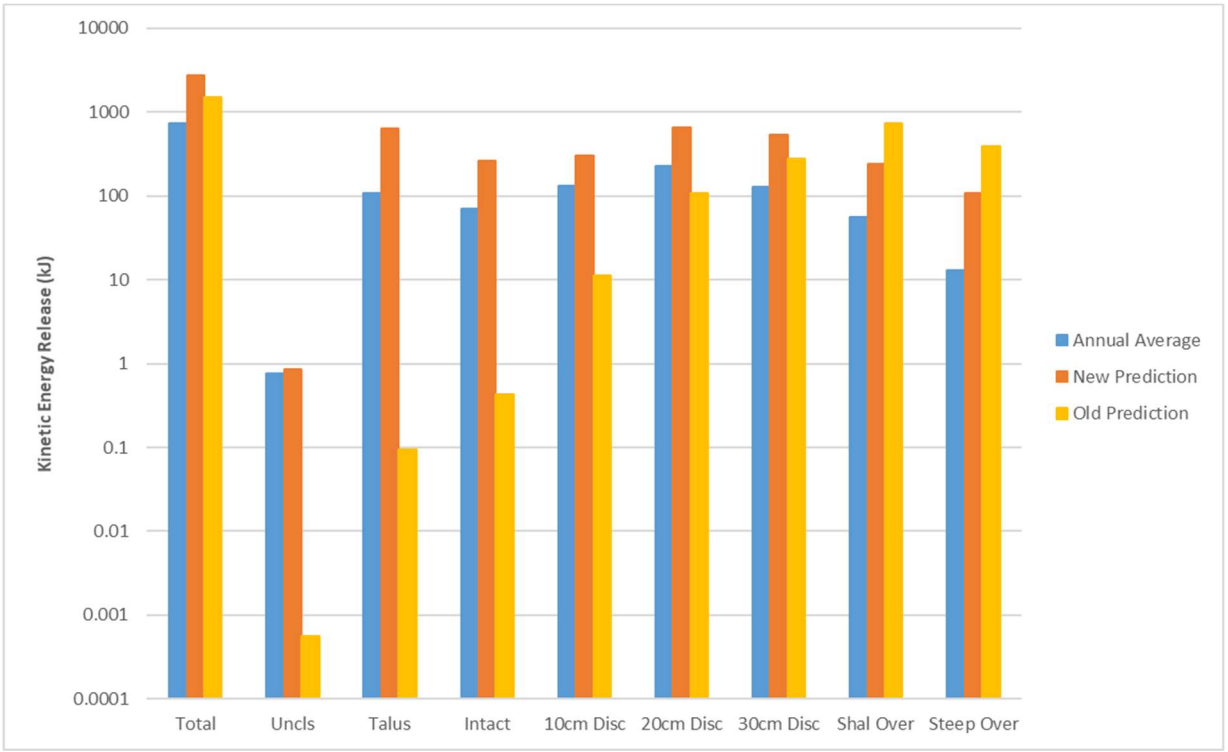

Figure 127. Annual Kinetic Energy Release (average) and KE Prediction using Original and Modified Parameters, LL87

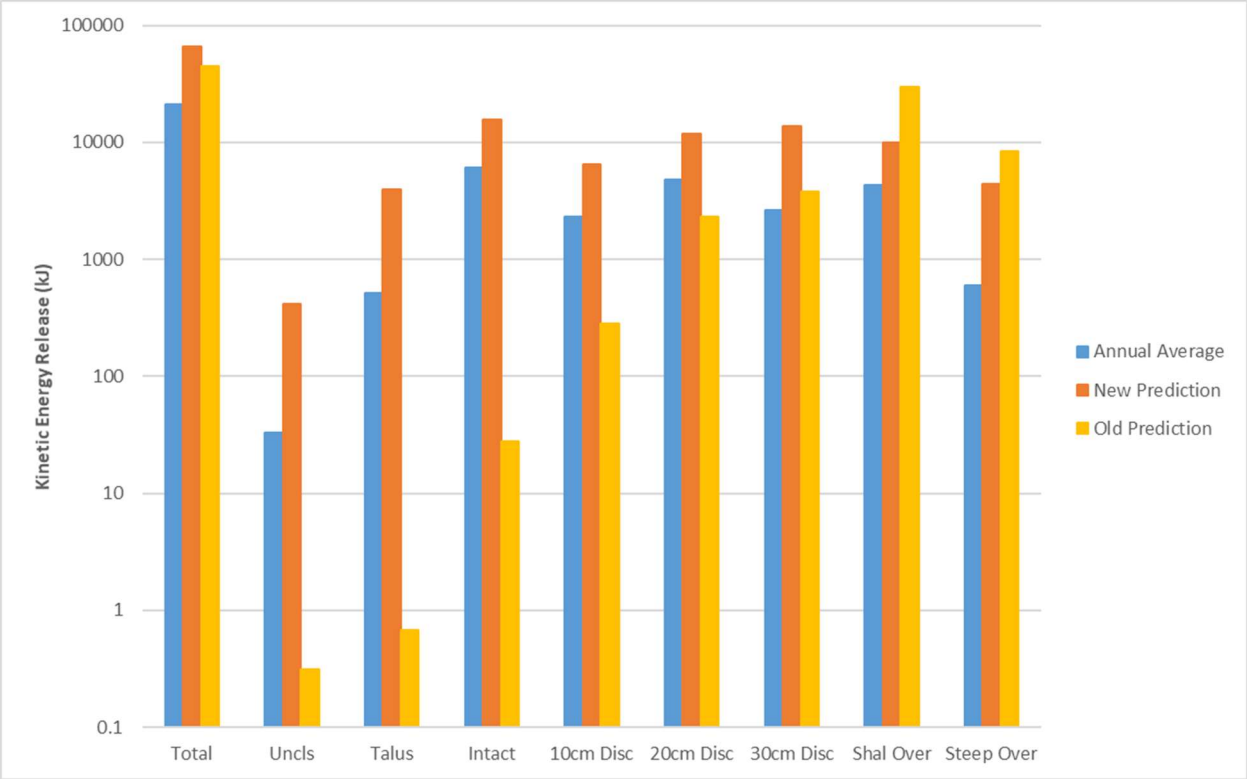

Figure 128. Annual Kinetic Energy Release (average) and KE Prediction using Original and Modified Parameters, LL71

As seen in Figures 125 through 128, Expected Kinetic Energy Release with the new Failure Rate and Failure Depth parameters has substantially exceeded the annual average of the recorded Kinetic Energy Release. This discrepancy is likely related to the non-uniform spatial distribution of failures, which has not been accounted for in this methodology. The RAI methodology assumes uniform spatial distribution of failures within each RAI Class, which has been shown to be unrealistic (See Section 4.1). For example, failures have a tendency to cluster on lower portions of the slope (see Figure 113. Spatial distribution of elevations of events at LL71, for the three change epochs. If we apply one correction factor for the average elevation of failures at Long Lake Site 71 (and, therefore, assume that the correction is uniform across RAI Classes), the Predicted Kinetic Energy Release can be re-calculated roughly accounting for vertical spatial distribution. Figures 129 through 132, below, show the new

predictions of Kinetic Energy Release, with this rudimentary method for accounting for spatial distributions of failures.

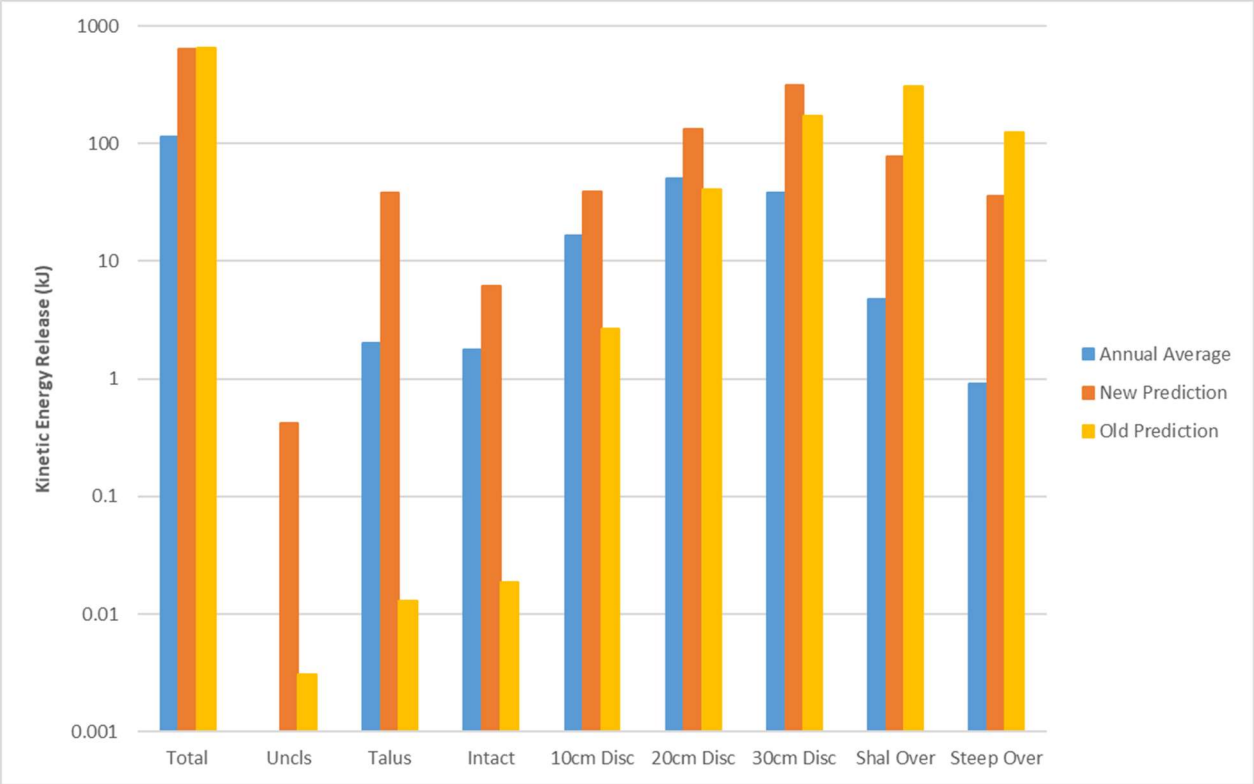

Figure 129. Annual Average KE Release, and KE Prediction using Original and Modified Parameters, accounting for Spatial Distribution, LL85.5

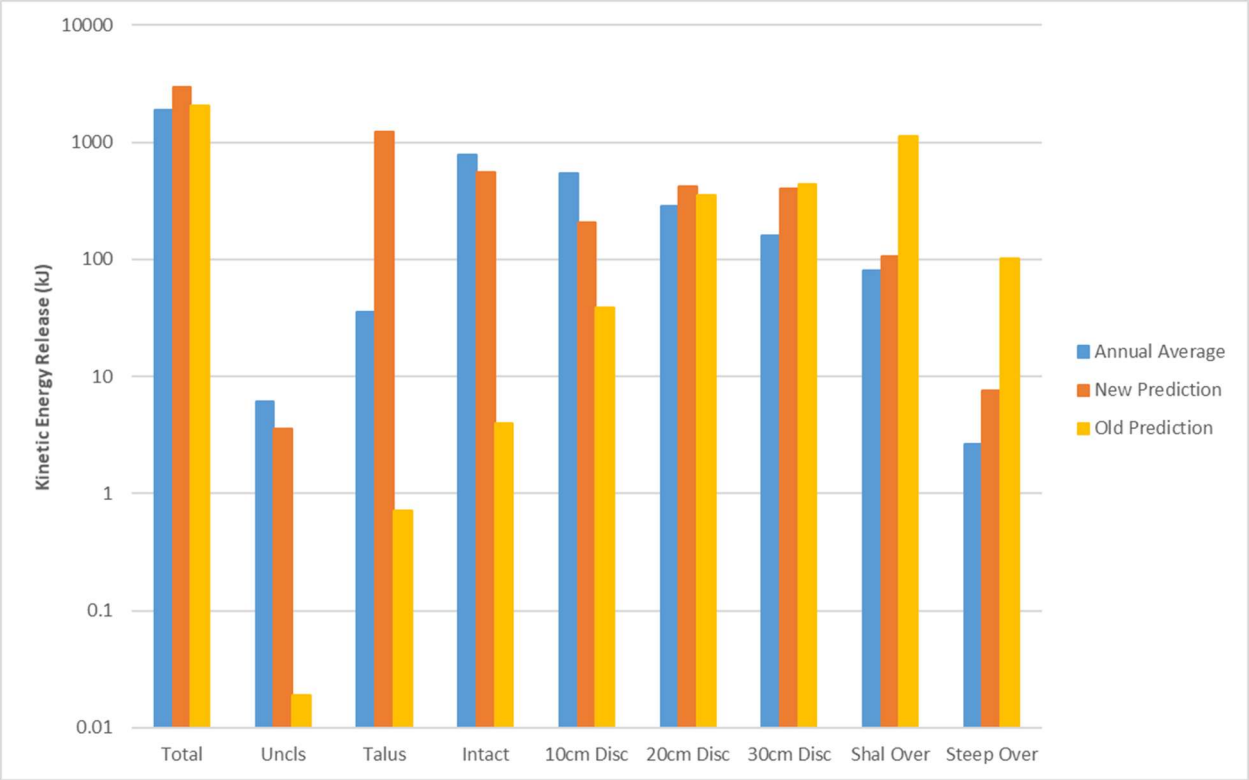

Figure 130. Annual Average KE Release, and KE Prediction using Original and Modified Parameters, accounting for Spatial Distribution, LL86.9

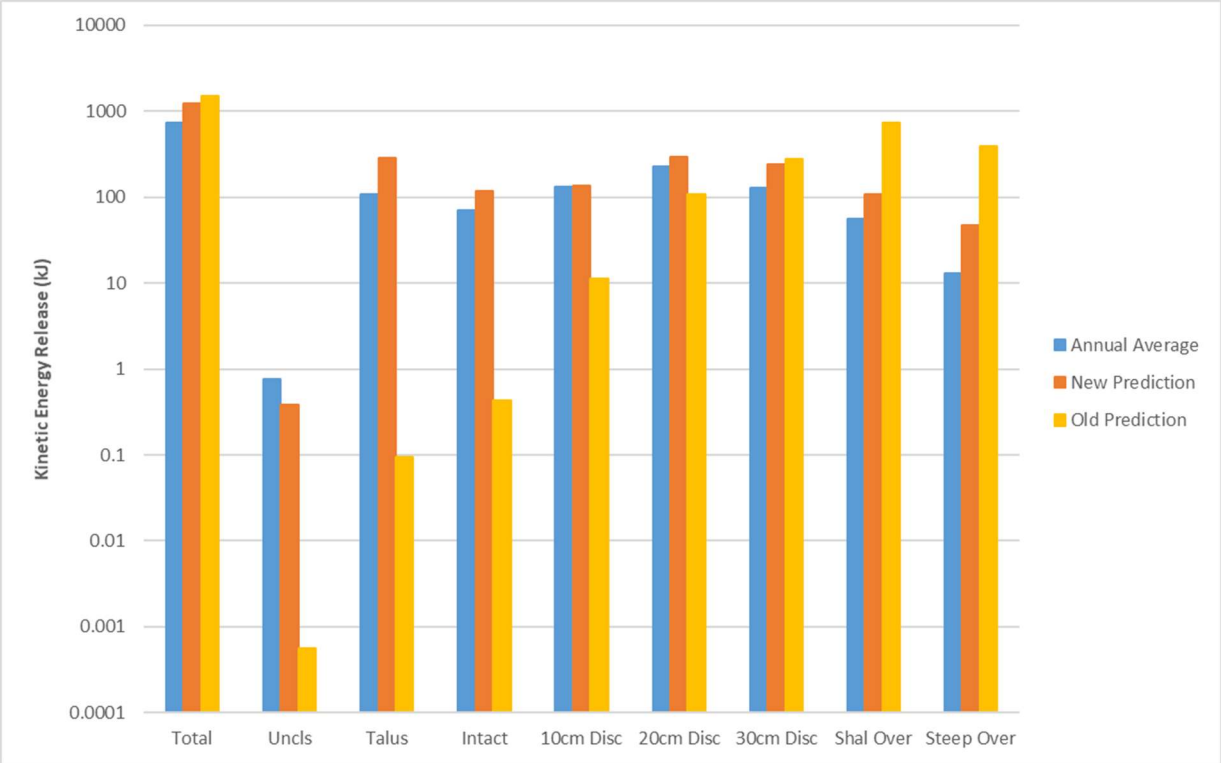

Figure 131. Annual Average KE Release, and KE Prediction using Original and Modified Parameters, accounting for Spatial Distribution, LL87

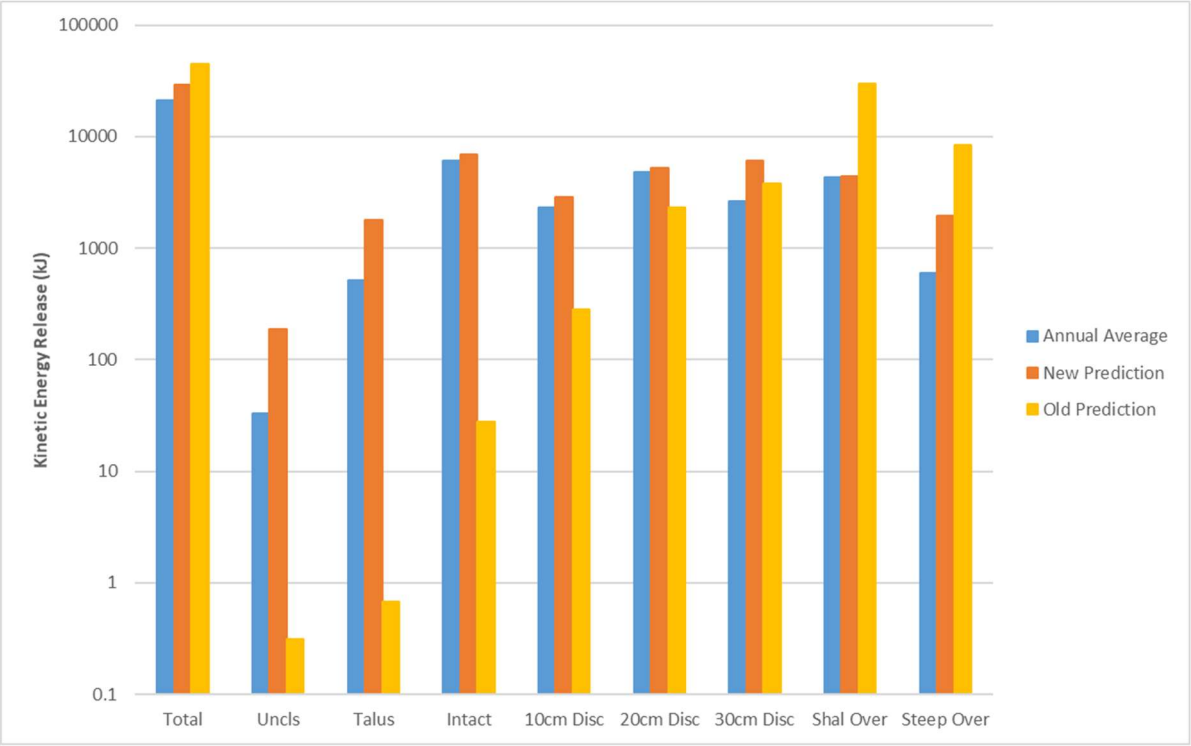

Figure 132. Annual Average KE Release, and KE Prediction using Original and Modified Parameters, accounting for Spatial Distribution, LL71.

With the rudimentary correction for spatial distribution of failures, the Kinetic Energy Release prediction is far closer than the observed value for all sites and RAI Classes. Spatial Distribution will need to be accounted for in future improvements to the RAI methodology, though will likely depend on change detection data for each rock-slope to properly understand spatial distributions of failures.

Below, in Figure 133, the distribution of failures at Long Lake Site 71 (in blue) overlies the expected Kinetic Energy Release, with red indicating greater expected contribution to this parameter.

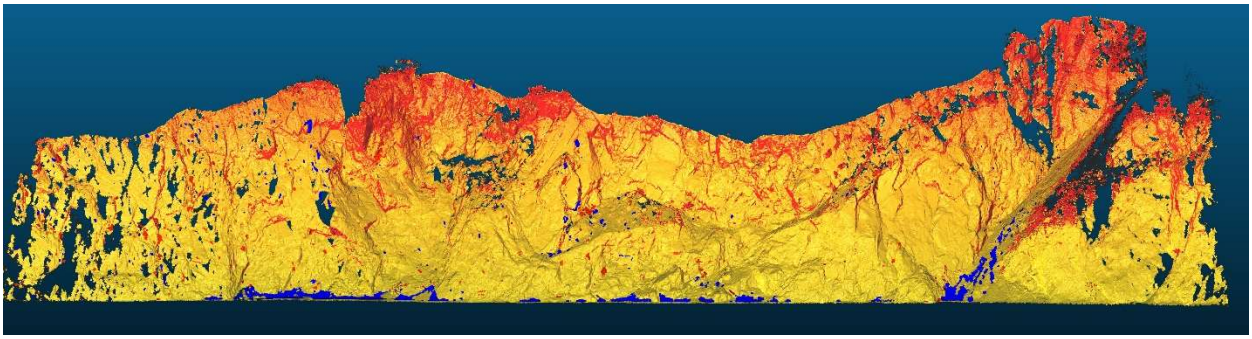

Figure 133. Failures (in blue) overlying Expected Kinetic Energy Release at LL71, 2015-2017.

Appendix A – RAI Size-Frequency Site Comparisons

Below are comparisons of the size-frequency curves compared between sites. Size-frequency parameters for all RAI Classes are provided as well. Note that data for all of the years was combined at LL85.5, LL86.9, and LL87; the data set was too small to provide adequate yearly RAI Class size-frequency parameters at these sites.

RAI Class	Talus	Intact	10-cm Disc Spacing	20cm Disc Spacing	30cm Disc Spacing	Shallow Overhang	Steep Overhang
Activity, β							
LL71, 2013-2014	1.99923	0.327153	0.142299	0.706155	0.349392	0.826254	0.35224
LL71, 2014-2015	1.810212	0.364896	0.131692	0.763154	0.59826	0.78246	0.808632
LL71, 2015-2017	1.59444	0.213218	0.154062	0.397824	0.224779	0.340065	0.039816
LL85.5	0.564728	0.476833	0.453052	0.320578	0.319925	N/A	N/A
LL86.9	1.2732	0.538009	0.607578	1.277986	0.394568	0.853007	N/A
LL87	1.4051	0.228025	0.092607	0.592729	0.801678	0.252556	N/A
Scaling, α							
LL71, 2013-2014	1.412	1.653	1.873	1.662	1.696	1.702	1.74
LL71, 2014-2015	1.753	1.576	1.902	1.722	1.59	1.63	1.396
LL71, 2015-2017	1.516	1.589	1.951	1.777	1.667	1.687	1.504
LL85.5	1.419	1.601	1.346	1.564	1.468	N/A	N/A
LL86.9	1.3	1.764	1.655	1.648	1.62	1.401	N/A
LL87	1.363	1.622	1.644	1.547	1.53	1.753	N/A
Recession Rate (m/yr)							
LL71, 2013-2014	0.032404	0.007482	0.000278	0.002334	0.001183	0.005266	0.000497
LL71, 2014-2015	0.011426	0.004963	0.000428	0.001884	0.003892	0.002853	0.000672
LL71, 2015-2017	0.01637	0.001691	0.000217	0.001778	0.001416	0.00199	2.28E-06
LL85.5	0.000167	0.000358	0.000748	0.000672	0.000845	N/A	N/A
LL86.9	0.007263	0.000595	0.001557	0.003446	0.000633	0.001621	N/A
LL87	0.006129	0.000529	8.77E-05	0.001757	0.001915	0.000448	1.5E-05

Table 31. Size-Frequency Parameters for RAI Classes for All Sites and Years Considered.

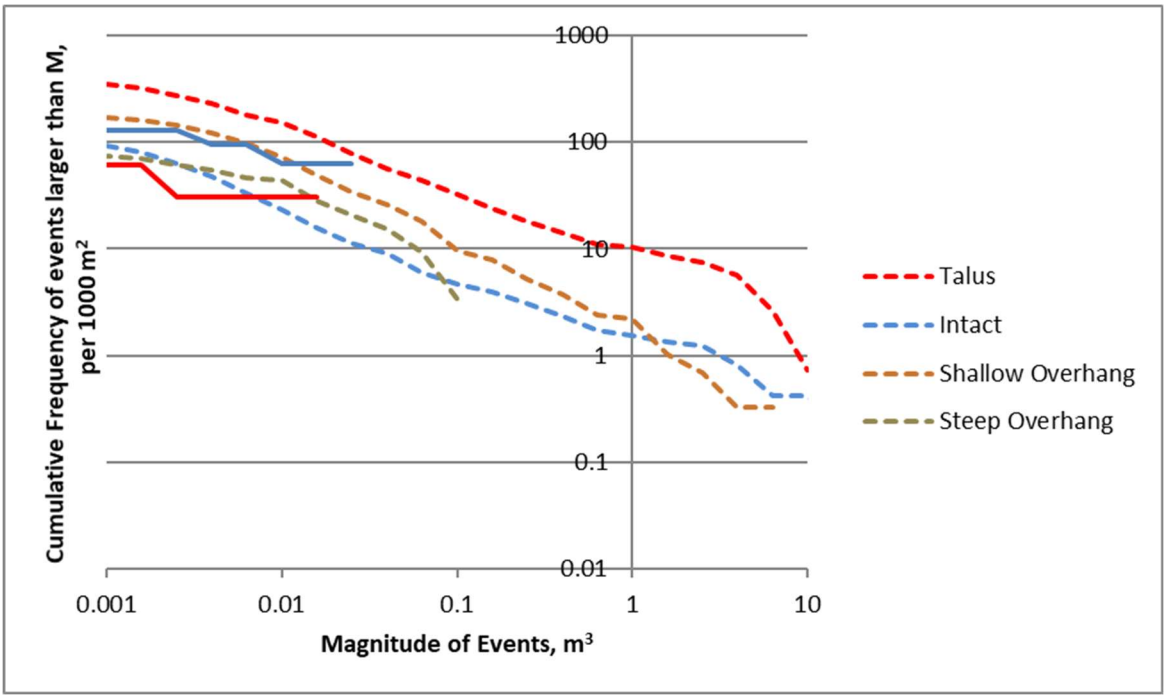

Figure 134. RAI Class Comparison between LL85.5 (solid) and LL71 (dashed) for four years of data.

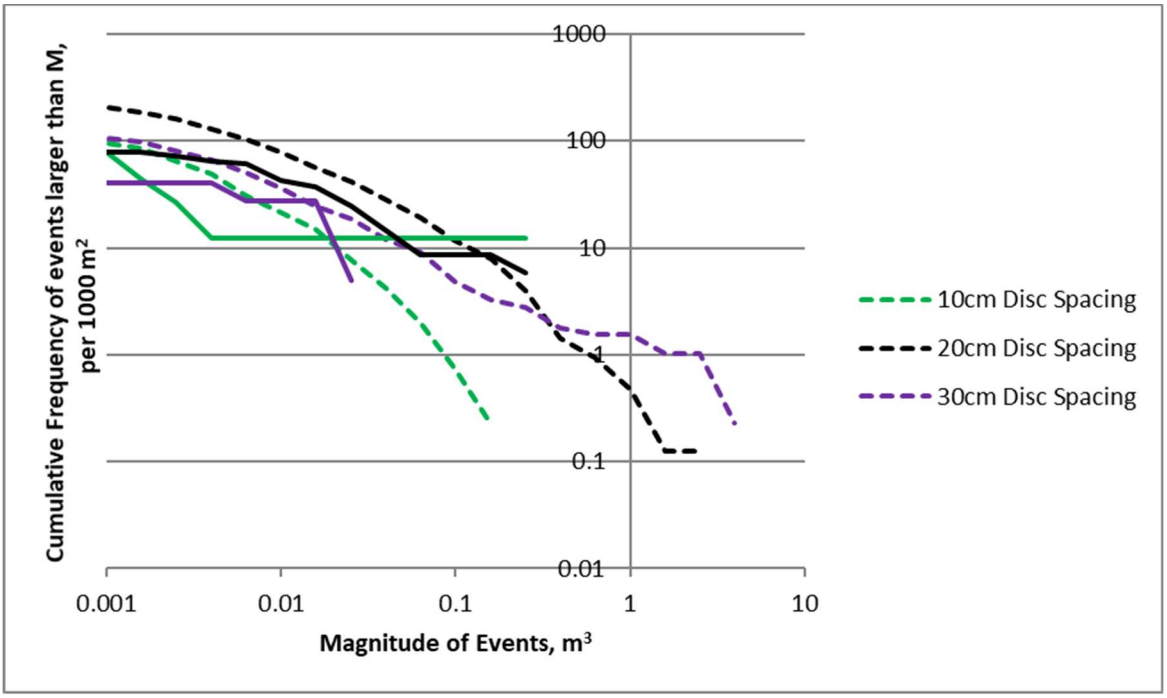

Figure 135. RAI Class Comparison between LL86.9 (solid) and LL71 (dashed) for four years of data.

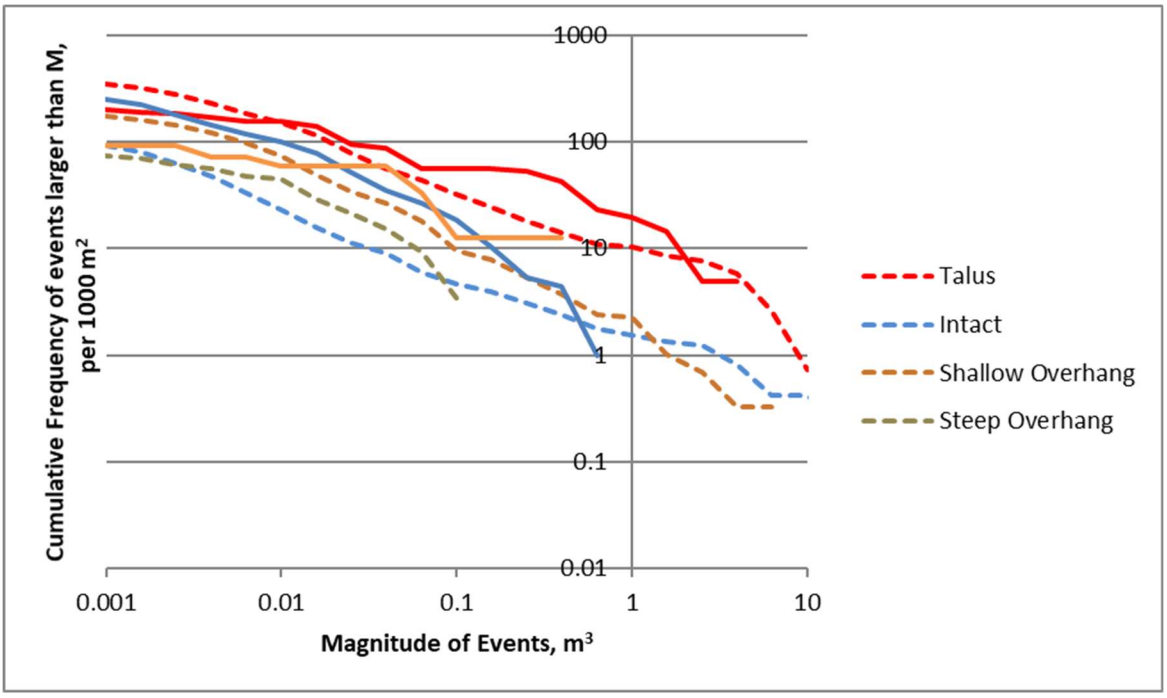

Figure 136. RAI Class Comparison between LL86.9 (solid) and LL71 (dashed) for four years of data.

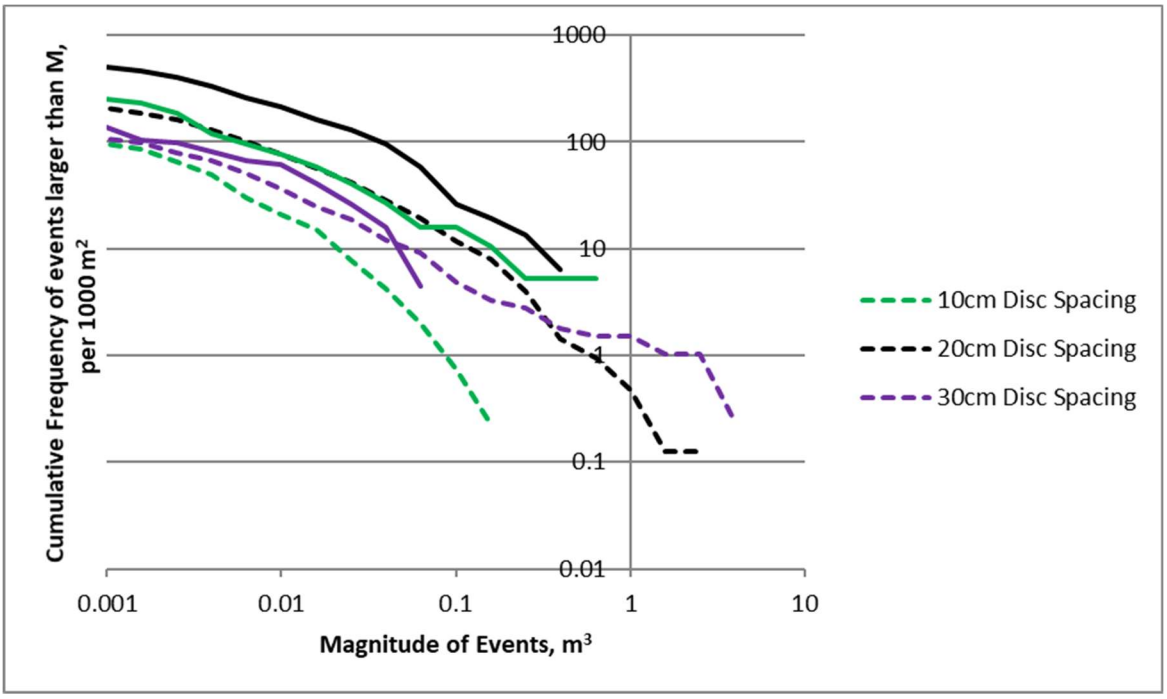

Figure 137. RAI Class Comparison between LL86.9 (solid) and LL71 (dashed) for four years of data

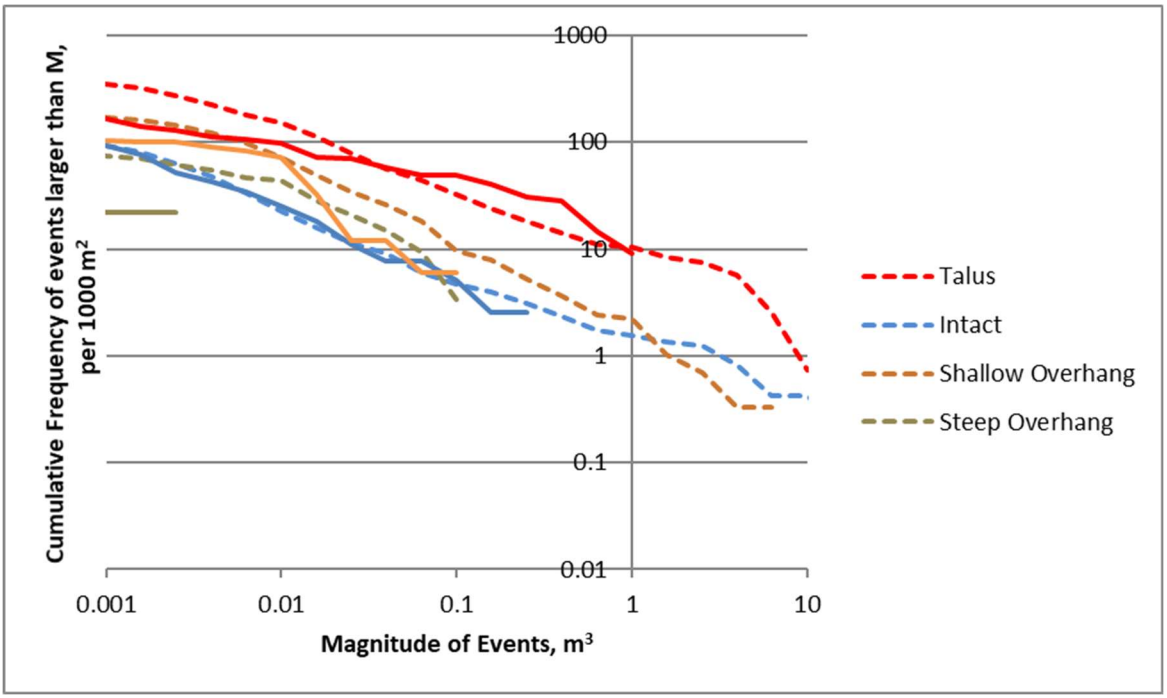

Figure 138. RAI Class Comparison between LL87 (solid) and LL71 (dashed) for four years of data.

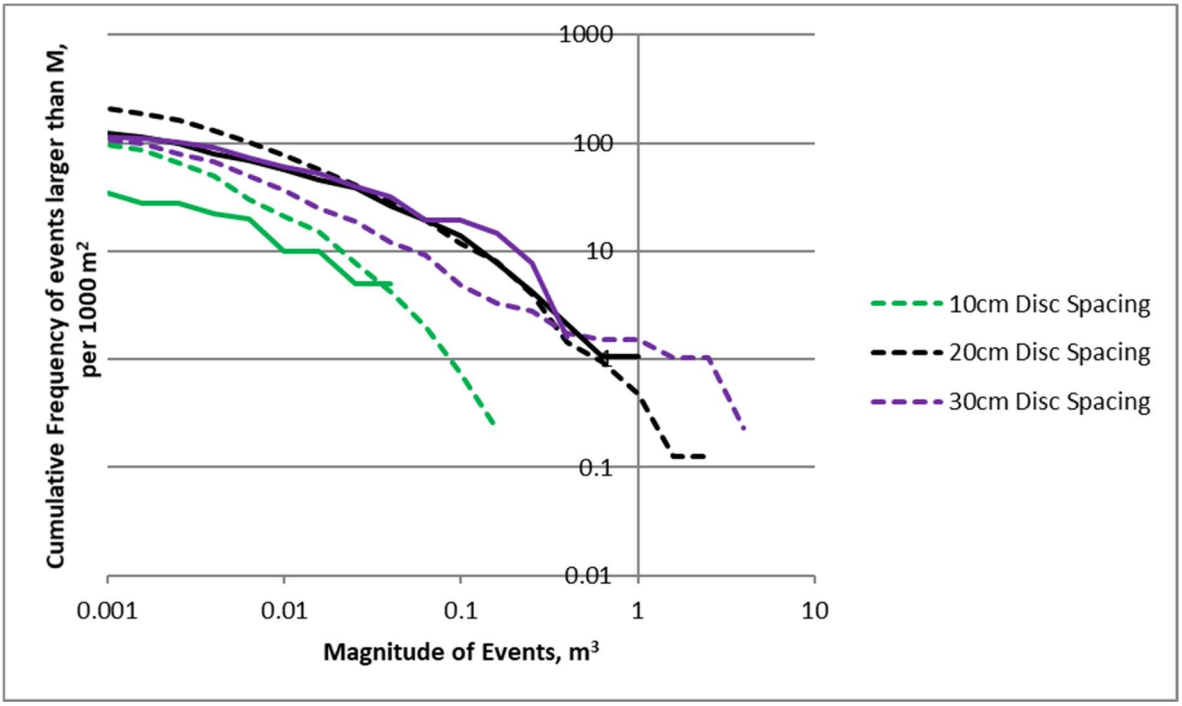

Figure 139. RAI Class Comparison between LL87 (solid) and LL71 (dashed) for four years of data.

Appendix B – RAI Size-Frequency Year Comparisons

Figures 140 through 143, below, show variations in size-frequency curves for the 7 RAI Classes at LL71 between the change epochs.

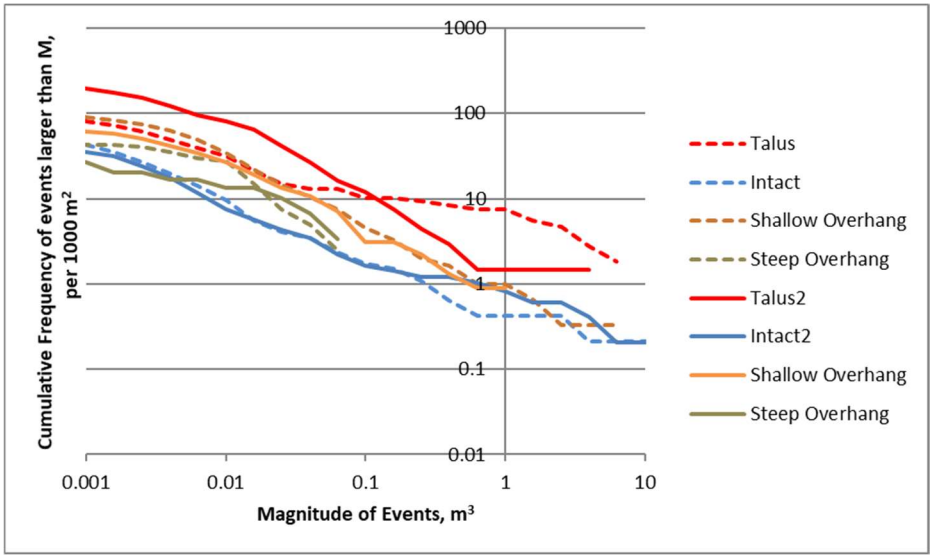

Figure 140. RAI Class Comparison at LL71 between 2013-2014 (dashed) and 2014-2015 (solid) change epochs

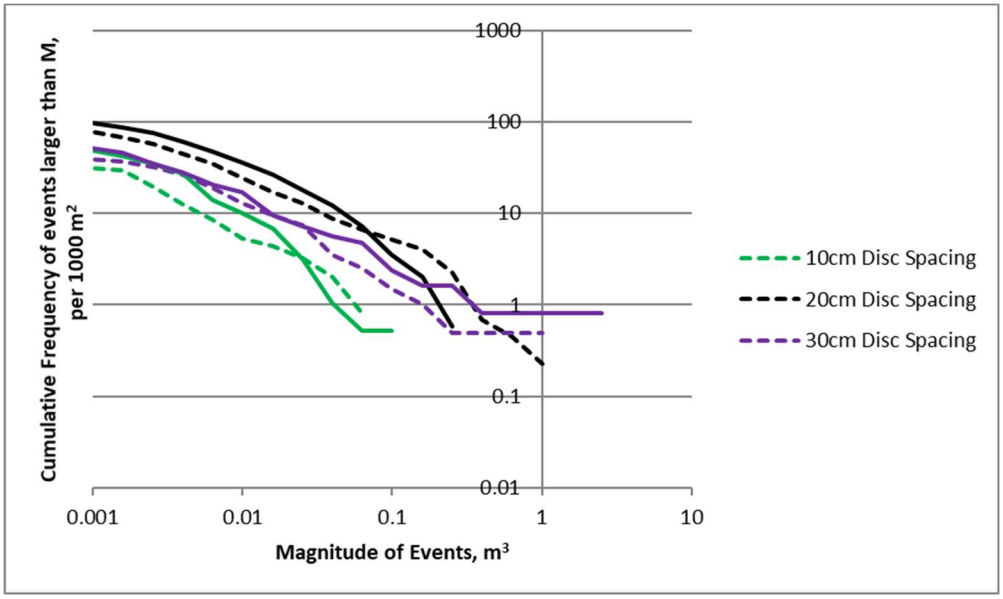

Figure 141. RAI Class Comparison at LL71 between 2013-2014 (dashed) and 2014-2015 (solid) change epochs

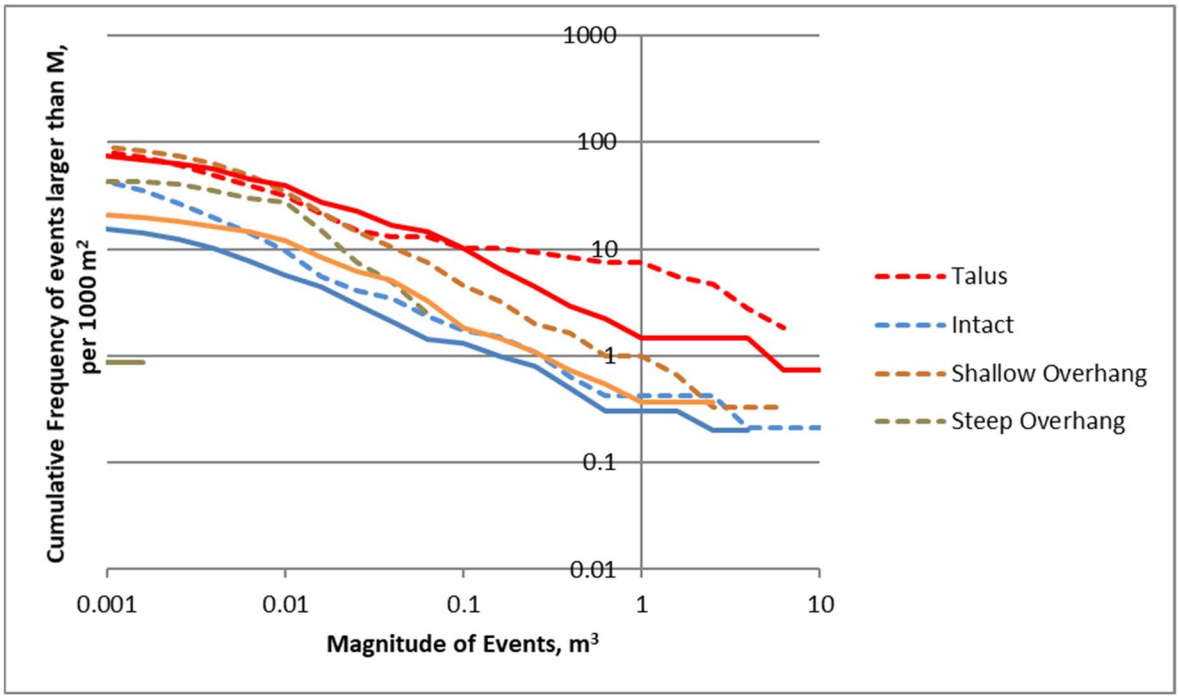

Figure 142. RAI Class Comparison at LL71 between 2014-2015 (dashed) and 2015-2017 (solid) change epochs

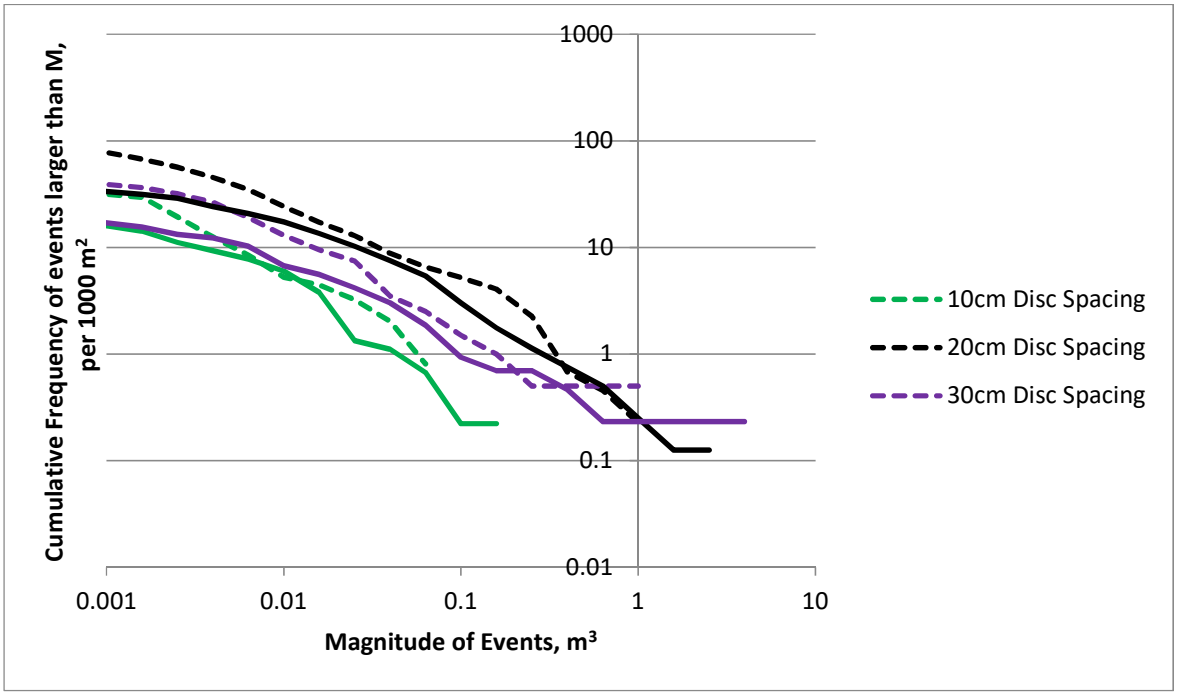

Figure 143. RAI Class Comparison at LL71 between 2014-2015 (dashed) and 2015-2017 (solid) change epochs

Appendix C – Failure Rate, Failure Depth, and Kinetic Energy Release Data

Long Lake 85.5 – Failure Rates					
Change Epoch	**2012-2013**	**2013-2014**	**2014-2015**	**2015-2017**	**Assumed Value**
Unclassified	0	0	0.0000	0.0094	0.000125
Talus	0.0458221	0.0085	0.0398	0.0373	0.000125
Intact	0.0139535	0.0186	0.0322	0.0344	0.000125
10cm Discontinuities	0.0247739	0.0144	0.0228	0.0888	0.002030
20cm Discontinuities	0.0088194	0.0101	0.0215	0.0926	0.004600
30cm Discontinuities	0.0113135	0.0036	0.0188	0.0526	0.009980
Shallow Overhang	0.0023006	0.0020	0.0093	0.0063	0.029410
Steep Overhang	0.0076336	0.0000	0.0181	0.0037	0.039210

Table 33. Failure rates recorded for the RAI Classes, for Long Lake Site 85.5

Long Lake 86.9 – Failure Rates					
Change Epoch	**2012-2013**	**2013-2014**	**2014-2015**	**2015-2017**	**Assumed Value**
Unclassified	0.0136	0.1599	0.0093	0.0036	0.000125
Talus	0.0071	0.4131	0.0292	0.2601	0.000125
Intact	0.0052	0.0617	0.0673	0.0798	0.000125
10cm Discontinuities	0.032	0.1183	0.1194	0.0704	0.002030
20cm Discontinuities	0.0217	0.0989	0.1190	0.0820	0.004600
30cm Discontinuities	0.014	0.0472	0.0898	0.0343	0.009980
Shallow Overhang	0.0376	0.1086	0.1520	0.0562	0.029410
Steep Overhang	0	0.0471	0.2436	0.0339	0.039210

Table 34. Failure rates recorded for the RAI Classes, for Long Lake Site 86.9

Long Lake 87 – Failure Rates					
Change Epoch	**2012-2013**	**2013-2014**	**2014-2015**	**2015-2017**	**Assumed Value**
Unclassified	0	0	N/A	0.0924	0.000125
Talus	0.0530223	0.0557	N/A	0.2100	0.000125
Intact	0.0047995	0.0216	N/A	0.0555	0.000125
10cm Discontinuities	0	0.0167	N/A	0.1086	0.002030
20cm Discontinuities	0.0026933	0.0204	N/A	0.0827	0.004600
30cm Discontinuities	0.0039332	0.0152	N/A	0.0438	0.009980
Shallow Overhang	0.0070157	0.0257	N/A	0.0361	0.029410
Steep Overhang	0.0196078	0.0371	N/A	0.0415	0.039210

Table 35. Failure rates recorded for the RAI Classes, for Long Lake Site 87

Long Lake 71 – Failure Rates					
Change Epoch	**2012-2013**	**2013-2014**	**2014-2015**	**2015-2017**	**Assumed Value**
Unclassified	N/A	0.0170	0.0167	0.0043	0.000125
Talus	N/A	0.1990	0.1385	0.2222	0.000125
Intact	N/A	0.0345	0.0246	0.0235	0.000125
10cm Discontinuities	N/A	0.0335	0.0287	0.0385	0.002030
20cm Discontinuities	N/A	0.0426	0.0369	0.0434	0.004600
30cm Discontinuities	N/A	0.0429	0.0399	0.0471	0.009980
Shallow Overhang	N/A	0.0367	0.0294	0.0234	0.029410
Steep Overhang	N/A	0.0586	0.0501	0.0419	0.039210

Table 36. Failure rates recorded for the RAI Classes, for Long Lake Site 71

Long Lake 85.5 – Failure Depths					
Change Epoch	**2012-2013**	**2013-2014**	**2014-2015**	**2015-2017**	**Assumed Value**
Unclassified	0	0	0	0.0000	-0.025
Talus	-0.09334	-0.0635	-0.0518	-0.0674	-0.025
Intact	-0.09951	-0.1034	-0.0530	-0.0627	-0.05
10cm Discontinuities	-0.0932	-0.1058	-0.1045	-0.1015	-0.10
20cm Discontinuities	-0.09287	-0.0834	-0.0834	-0.1118	-0.20
30cm Discontinuities	-0.09929	-0.0991	-0.1583	-0.1321	-0.30
Shallow Overhang	-0.12202	-0.1064	-0.2002	-0.1041	-0.50
Steep Overhang	-0.15789	0	-0.2861	-0.1533	-0.75

Table 37. Average failure depths recorded for the RAI Classes, for Long Lake Site 85.5

Long Lake 86.9 – Failure Depths					
Change Epoch	**2012-2013**	**2013-2014**	**2014-2015**	**2015-2017**	**Assumed Value**
Unclassified	-0.10472	-0.1316	-0.0388	-0.1134	-0.025
Talus	-0.07348	-0.0773	-0.0433	-0.1200	-0.025
Intact	-0.09735	-0.0576	-0.0467	-0.0971	-0.05
10cm Discontinuities	-0.13333	-0.0770	-0.0553	-0.1071	-0.10
20cm Discontinuities	-0.13234	-0.0951	-0.0608	-0.1119	-0.20
30cm Discontinuities	-0.16505	-0.1275	-0.0852	-0.1369	-0.30
Shallow Overhang	-0.16981	-0.1131	-0.0854	-0.1102	-0.50
Steep Overhang	0	-0.1707	-0.1444	-0.2555	-0.75

Table 38. Average failure depths recorded for the RAI Classes, for Long Lake Site 86.9

Long Lake 87 – Failure Depths					
Change Epoch	**2012-2013**	**2013-2014**	**2014-2015**	**2015-2017**	**Assumed Value**
Unclassified	0	0	N/A	-0.1556	-0.025
Talus	-0.12469	-0.0608	N/A	-0.0921	-0.025
Intact	-0.15852	-0.0559	N/A	-0.0919	-0.05
10cm Discontinuities	0	-0.0833	N/A	-0.1324	-0.10
20cm Discontinuities	-0.11455	-0.0901	N/A	-0.1341	-0.20
30cm Discontinuities	-0.27219	-0.1086	N/A	-0.1562	-0.30
Shallow Overhang	-0.16926	-0.1071	N/A	-0.1610	-0.50
Steep Overhang	-0.23702	-0.1344	N/A	-0.1956	-0.75

Table 3932. Average failure depths recorded for the RAI Classes, for Long Lake Site 87

Long Lake 71 – Failure Depths					
Change Epoch	**2012-2013**	**2013-2014**	**2014-2015**	**2015-2017**	**Assumed Value**
Unclassified	N/A	-0.2275	-0.124756	-0.182561	-0.025
Talus	N/A	-0.1677	-0.097317	-0.204569	-0.025
Intact	N/A	-0.2306	-0.15735	-0.181123	-0.05
10cm Discontinuities	N/A	-0.1841	-0.122335	-0.225287	-0.10
20cm Discontinuities	N/A	-0.1797	-0.117618	-0.231848	-0.20
30cm Discontinuities	N/A	-0.1825	-0.14205	-0.335023	-0.30
Shallow Overhang	N/A	-0.2197	-0.155295	-0.251333	-0.50
Steep Overhang	N/A	-0.2306	-0.148056	-0.283494	-0.75

Table 40. Average failure depths recorded for the RAI Classes, for Long Lake Site 71

Long Lake 85.5 – Kinetic Energy Release					
Change Epoch	**2012-2013**	**2013-2014**	**2014-2015**	**2015-2017**	**Predicted**
Total	5.3808254	18.23251	127.6316	311.2527	647.764802
Unclassified	0	0.0000	0.0000	0.0000	0.00308
Talus	0.9918892	1.3946	2.5280	4.1851	0.013147
Intact	0.2106026	3.0071	1.6762	2.4569	0.018766
10cm Discontinuities	1.1742945	3.7798	19.9003	42.4051	2.648478
20cm Discontinuities	1.2243417	6.0117	32.0950	163.3919	41.045740
30cm Discontinuities	1.245209	2.9560	53.1621	95.3484	173.125780
Shallow Overhang	0.4402916	1.0834	15.0036	3.1177	305.890856
Steep Overhang	0.0941968	0.0000	3.2663	0.3476	125.018955

Table 41. Kinetic Energy Release (kJ) recorded for the RAI Classes, for Long Lake Site 85.5

Long Lake 86.9 – Kinetic Energy Release					
Change Epoch	**2012-2013**	**2013-2014**	**2014-2015**	**2015-2017**	**Predicted**
Total	81.91117	1861.635	791.1586	4920.6310	2060.401660
Unclassified	0.0047099	23.5500	0.2025	0.5010	0.018996
Talus	0.5176093	128.8301	10.9586	1.9510	0.715602
Intact	9.37E+00	354.4584	325.4097	2437.1000	3.941311
10cm Discontinuities	20.754164	203.7738	142.9320	1839.3000	38.482542
20cm Discontinuities	30.98403	471.8450	242.0220	422.0400	350.203049
30cm Discontinuities	11.57314	468.3263	36.2541	132.7500	441.046430
Shallow Overhang	8.7081097	202.0761	32.7648	85.7200	1124.414464
Steep Overhang	0	8.7750	0.6149	1.2690	101.579564

Table 42. Kinetic Energy Release (kJ) recorded for the RAI Classes, for Long Lake Site 86.9

Long Lake 87 – Kinetic Energy Release					
Change Epoch	**2012-2013**	**2013-2014**	**2014-2015**	**2015-2017**	**Predicted**
Total	20.646862	470.3844	N/A	1730.968	1515.977176
Unclassified	0	0.0000	N/A	2.3190	0.000559
Talus	3.833861	61.0165	N/A	260.6790	0.094531
Intact	5.6894128	66.7962	N/A	146.2900	0.433295
10cm Discontinuities	0	52.1571	N/A	345.3000	11.343153
20cm Discontinuities	3.6971022	137.4929	N/A	537.7600	108.399129
30cm Discontinuities	4.3706084	80.8478	N/A	302.4000	270.326936
Shallow Overhang	2.2502697	58.8805	N/A	110.6100	735.803492
Steep Overhang	0.8056078	13.1933	N/A	25.6100	389.576082

Table 43. Kinetic Energy Release (kJ) recorded for the RAI Classes, for Long Lake Site 86.9

Long Lake 71 – Kinetic Energy Release					
Change Epoch	**2012-2013**	**2013-2014**	**2014-2015**	**2015-2017**	**Predicted**
Total	N/A	37279.24	15048.24	32964.39	44789.9
Unclassified	N/A	90.27	10.99	30.67	0.31
Talus	N/A	458.55	249.54	1332.67	0.67
Intact	N/A	12156.87	4616.06	7484.52	27.77
10cm Discontinuities	N/A	3491.53	1755.74	4109.24	283.31
20cm Discontinuities	N/A	7540.59	3723.14	8024.65	2324.88
30cm Discontinuities	N/A	2948.14	1465.68	6104.90	3773.12
Shallow Overhang	N/A	9374.14	2853.69	5090.18	29921.49
Steep Overhang	N/A	1219.15	373.39	787.55	8458.27

Table 44. Kinetic Energy Release (kJ) recorded for the RAI Classes, for Long Lake Site 86.9

Appendix D – Expected Annual Kinetic Energy Release, Old and New Parameters

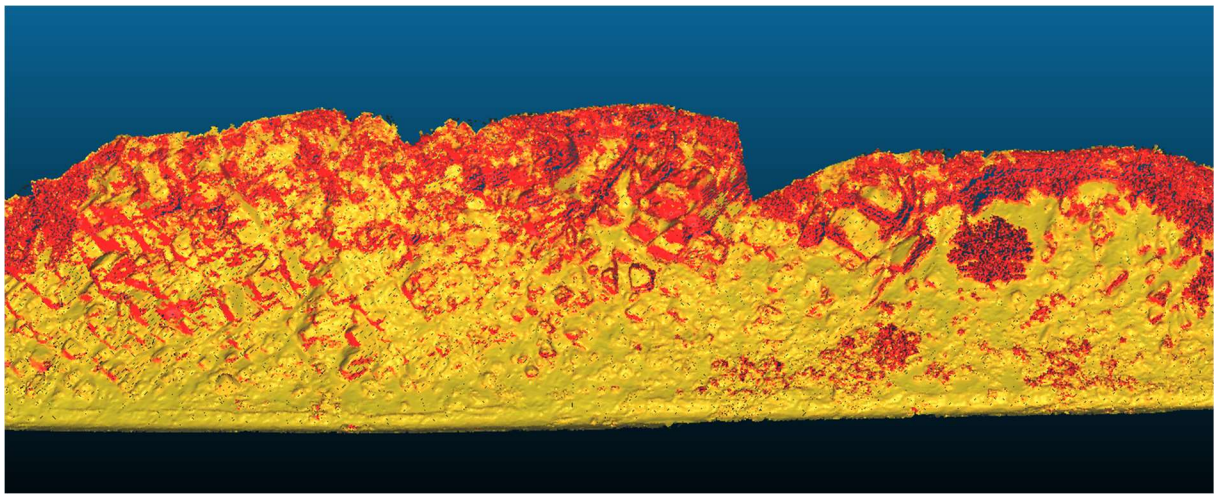

Figure 144. Expected KE Release, Old Parameters, LL85.5

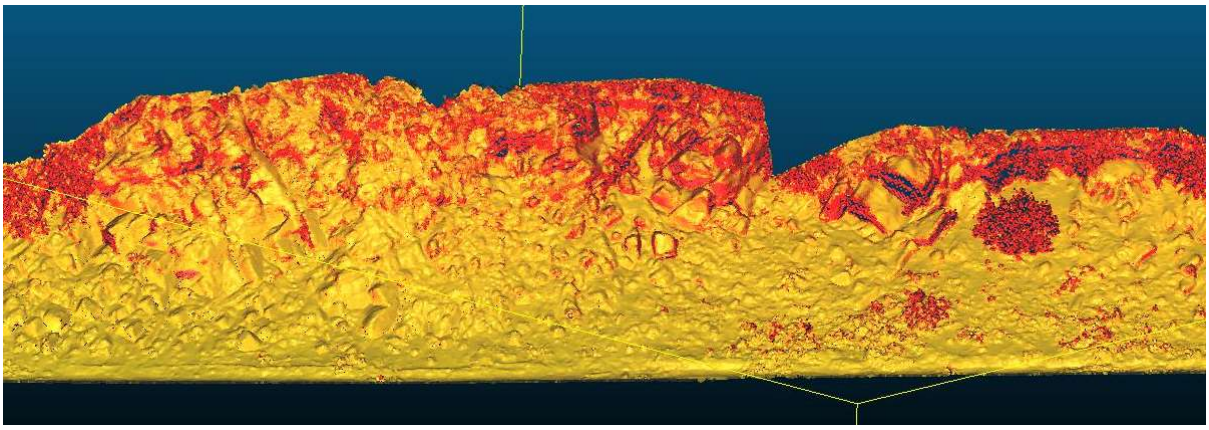

Figure 145. Expected KE Release, new Parameters, LL85.5

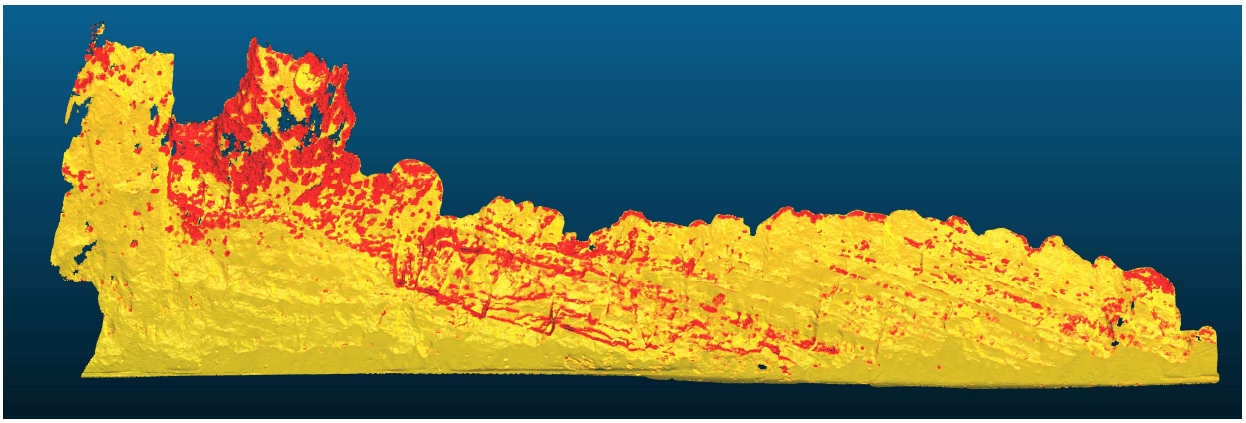

Figure 146. Expected KE Release, Old Parameters, LL86.9

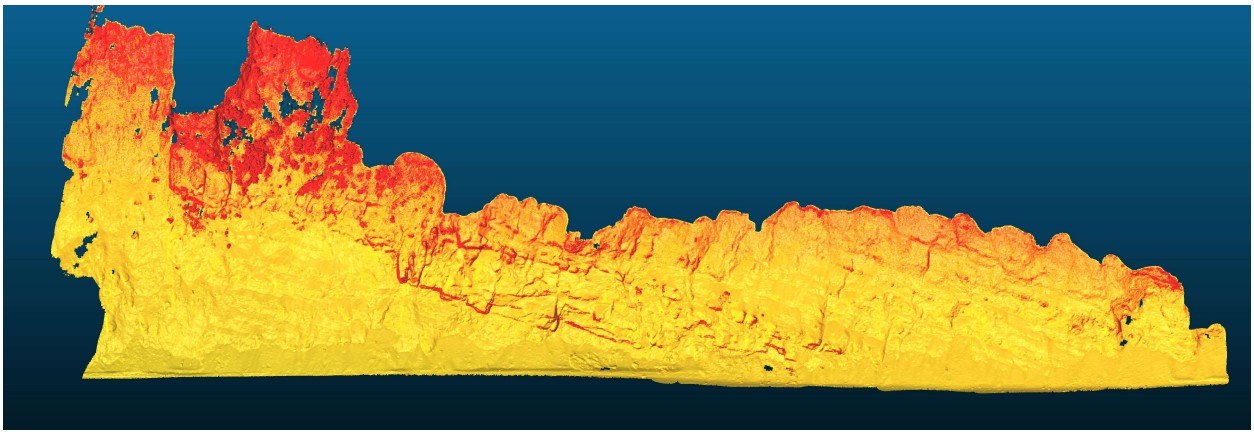

Figure 147. Expected KE Release, New Parameters, LL86.9

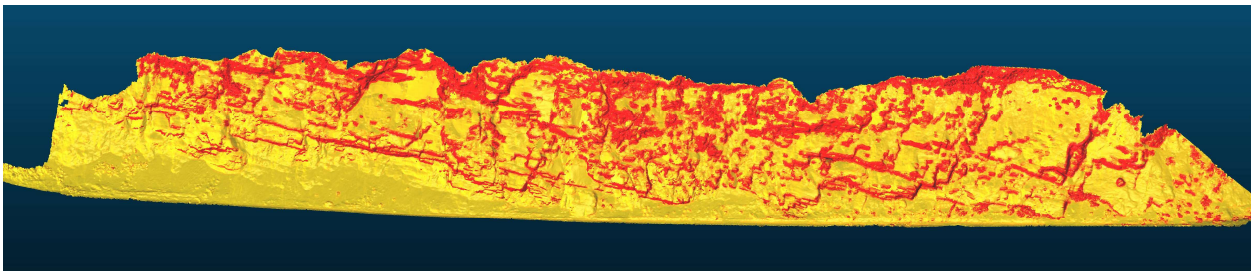

Figure 148. Expected KE Release, Old Parameters, LL87

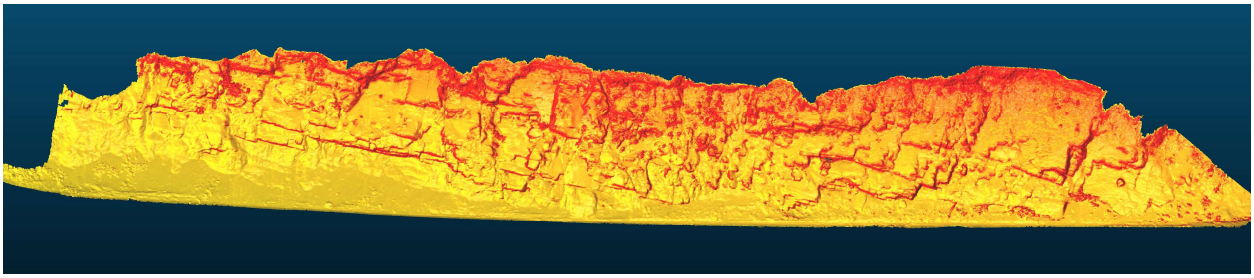

Figure 149. Expected KE Release, New Parameters, LL87.

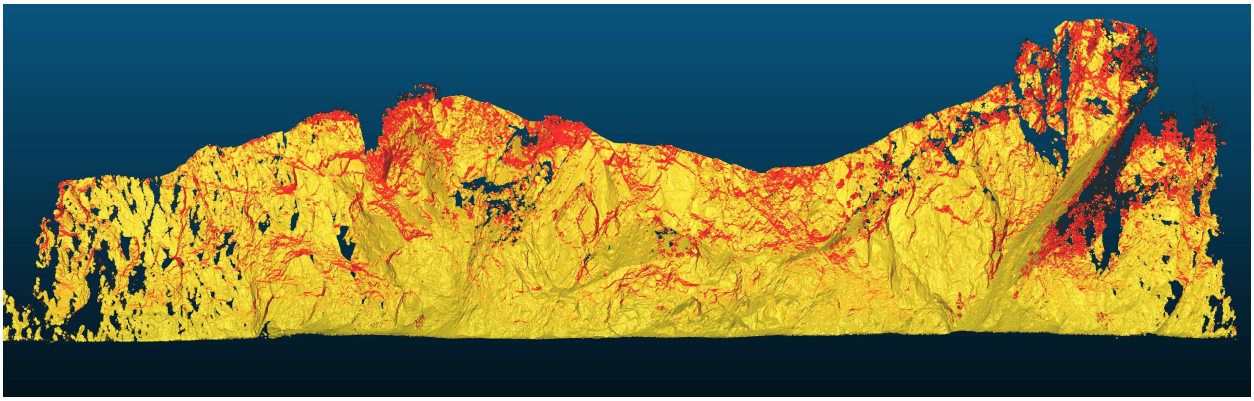

Figure 150. Expected KE Release, Old Parameters, LL71.

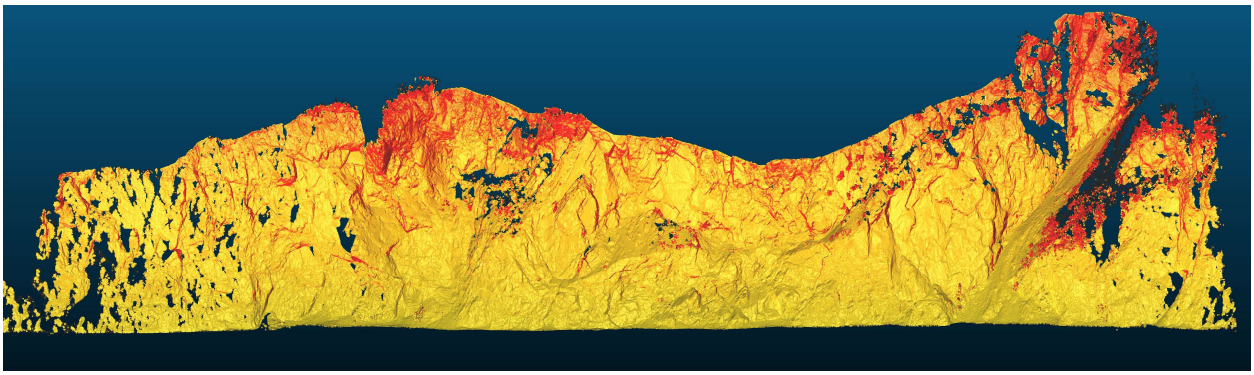

Figure 151. Expected KE Release, New Parameters, LL71.

References

Abellán *et al.* (2014). Terrestrial laser scanning of rock slope instabilities. *Earth Surface Processes and Landforms, 39(1).*

Alaska DNR. Division of Mining, Land and Water. (2009). *Wishbone Hill Permit Application*. Retrieved from http://dnr.alaska.gov/mlw/mining/coal/wishbone/

Barlow *et al. (2012).* Modeling cliff erosion using negative power law scaling of rockfalls. *Geomorphology, 139-140.* 416-424.

Benjamin *et al.* (2016). Rockfall detection and volumetric characterization using LiDAR. *Landslides and Engineered Slopes. Experience, Theory, and Practice.* 389-395.

Bieniawski, R.Z.T. (1997). Quo vadis rock mass classifications? Some thoughts on rating methods for tunnel design. *Felsbau, 15(3),* 177-178.

Carson, M. (1977). Angles of repose, angles of shearing resistance and angles of talus slopes. *Earth Surface Processes, 2.* 363-380.

Chandler, R. (1973). The Inclination of Talus, Arctic Talus Terraces, and Other Slopes Composed of Granular Materials. *The Journal of Geology, 81(1),* 1-14.

Clauset *et al.* (2009). Power Law Distributions in Empirical Data. *Society for Industrial and Applied Mathematics, 51(4).* 661-703.

Connor, C. (2014). *Roadside Geology of Alaska Second Edition.* Missoula, Montana: Mountain Press Publishing Company.

Dunham *et al.* (2017). Rockfall Activity Index (RAI): A lidar-derived, morphology-based method for hazard assessment. *Engineering Geology, 221,* 184-192.

Hantz, D. (2011). Qunatitative assessment of diffuse rock fall hazard along a cliff foot. *Natural Hazards and Earth System Sciences, 11,* 1303-1309.

Hergarten, S. (2003). Landslides, sandpiles and self-organized criticality. *Natural Hazards and Earth System Sciences, 3.* 505-514.

Hoek, E. (2006). *Practical Rock Engineering.* Vancouver, B.C.

Kassebaum, T. (2012). *Using LiDAR as a monitoring device to calculate volume of rockfall over time.* Unpublished master's thesis, Missouri University of Science and Technology, Rolla, Missouri.

Katsube, K. and Oguchi, T. (1999). Altitudinal Changes in Slope Angle and Profile Curvature in the Japan Alps: A Hypothesis Regarding a Characteristic Slope Angle. *Geographical Review of Japan, B(72).*

Kramer, S. (1996). *Geotechnical Earthquake Engineering.* Upper Saddle River, New Jersey: Prentice Hall Publishing.

Labay, K. and Haeussler, P. (2001). *GIS Coverages of the Castle Mountain Fault, South Central Alaska.* U.S. Geological Survey. Retrieved from https://pubs.usgs.gov/of/2001/of01-504/

Miller and Whitehead. (1999). *Ground Water Atlas of the United States: Segment 13, Alaska, Hawaii, Puerto Rico, and the U.S. Virgin Islands.* U.S. Geological Survey.

National Park Service. *Explore Nature – Geologic Resources – Education.* Retrieved from https://www.nature.nps.gov/geology/education/images/GRAPHICS/terrane_accretion.jpg

Olsen *et al.* (2015). To Fill or Not to Fill: Sensitivity Analysis of the Influence of Resolution and Hole Filling on Point Cloud Surface Modeling and Individual Rockfall Event Detection. *Remote Sensing, 7,* 12103-12134.

Ridgway *et al.* (2007). *Tectonic Growth of A Collisional Contental Margin: Crustal Evolution of Southern Alaska.* Geological Society of America.

Sæter, M.B. (2008). *Dynamics of Talus Formation.* Unpublished master's thesis, University of Oslo, Oslo, Norway.

Turner and Jayaprakash. (2012). *Rockfall Characterization and Control.* Washington, D.C.: Transportation Research Board.

Wilson *et al.* (2015). *Geologic Map of Alaska: U.S. Geological Survey Scientific Investigations Map 3340, pamphlet 197 p., 2 sheets* [map]. (1:1,584,000).